Forschungsbericht 2024-17

Experimental Investigation of Particle-Induced Heating Augmentation in Supersonic Flows

Dirk Allofs

Deutsches Zentrum für Luft- und Raumfahrt
Institut für Aerodynamik und Strömungstechnik
Köln

DLR
Deutsches Zentrum
für Luft- und Raumfahrt

Forschungsbericht 2024-17

Experimental Investigation of Particle-Induced Heating Augmentation in Supersonic Flows

Dirk Allofs

Deutsches Zentrum für Luft- und Raumfahrt
Institut für Aerodynamik und
Strömungstechnik
Köln

136	Seiten
70	Bilder
28	Tabellen
94	Literaturstellen

Deutsches Zentrum
DLR für Luft- und Raumfahrt

Herausgeber:

Deutsches Zentrum
für Luft- und Raumfahrt e. V.
Wissenschaftliche Information
Linder Höhe
D-51147 Köln

ISSN 1434-8454
ISRN DLR-FB-2024-17
Erscheinungsjahr 2024
DOI: 10.57676/r2e9-w211

Erklärung des Herausgebers
Dieses Werk wird unter den Bedingungen der Creative Commons Lizenz vom Typ Namensnennung Nicht kommerziell-Share Alike 4.0 International, abrufbar über https://creativecommons.org/licenses/by-nc-sa/4.0/legalcode.en zur Nutzung überlassen.

Lizenz
Creative Commons NonCommercial-ShareAlike Attribution 4.0 International

Staupunktwärmestrom, Heating Augmentation, Partikel, Partikelbeladene Strömung, Überschallströmung, Stoßschicht, Partikelvermessung, Partikelgröße, Partikelkonzentration, Partikelgeschwindigkeit, Partikelmassenkonzentration, Staub, Feststoffpartikel, Schattenverfahren, PIV, Particle-Image-Velocimetry, de Laval Düse

Dirk ALLOFS
DLR, Institut für Aerodynamik und Strömungstechnik, Köln

Experimentelle Untersuchung von partikelinduzierten Wärmestromsteigerungen in Überschallströmungen

RWTH Aachen

Partikel-beladene Überschallströmungen haben signifikante Aufheizungseffekte auf Proben sowie auf Raumtransportsysteme. Diese Aufheizungseffekte werden in der Fachwelt „particle-induced heating augmentation“ (Aufheizungsverstärkung durch Partikel) genannt. Die Modellierung und die Vorhersage solcher Effekte ist nach dem aktuellen Stand der Technik komplex und basiert lediglich auf eine geringe Anzahl an Experimenten. Um diese Datenbank zu erweitern wurden neuartige Versuche durchgeführt. Hierzu wurde zunächst eine kleine Versuchswindkanalanlage konzipiert, aufgebaut und charakterisiert. Es wurden optische nicht-intrusive Messtechniken weiterentwickelt, die es ermöglichen, einzelne Partikel vor und innerhalb der Stoßschicht individuell zu untersuchen. Diese Weiterentwicklungen konnten nicht nur bisherige Annahmen zum Thema „heating augmentation“ bekräftigen bzw. wiederlegen, sondern können auch die Genauigkeit von Partikeluntersuchungen im Allgemeinen signifikant erhöhen.

---

stagnation point heat flux, heating augmentation, particles, particle-laden flow, supersonic flow, shock layer, particle measurement technique, particle size, particle concentration, particle velocity, particle mass flow rate, dust, solid particles, shadowgraphy, direct-imaging, backlight imaging, PIV, particle-image-velocimetry, de Laval nozzle

(Published in English)

Dirk ALLOFS
German Aerospace Center (DLR), Institute of Aerodynamics and Flow Technology, Cologne

Experimental Investigation of Particle-Induced Heating Augmentation in Supersonic Flows

RWTH Aachen University

Dust particles in supersonic flows may cause significant increases of heat flux augmentation. These effects are called ‘particle-induced heat flux augmentation’ or ‘heating augmentation’ in the scientific community. The modelling approaches of these effects are based on a limited database and required several particle-related assumptions, since corresponding experiments are complex. New experiments were conducted to increase the heating augmentation database. A small test facility was conceived, set up, and characterised. Non-intrusive measurement techniques were tested and developed to characterize individual particles in front of- and within the shock layer. The new measurement technique developments were able to underline and to refute assumptions regarding heating augmentation. Furthermore, these developments improve significantly the accuracy of particle flux investigations in general.

Experimental Investigation of Particle-Induced Heating Augmentation in Supersonic Flows

Experimentelle Untersuchung von partikelinduzierten Wärmestromsteigerungen in Überschallströmungen

Von der Fakultät für Maschinenwesen der Rheinisch-Westfälischen Technischen Hochschule Aachen zur Erlangung des akademischen Grades eines Doktors der Ingenieurwissenschaften genehmigte Dissertation

vorgelegt von

Dirk Allofs, geb. Kerkhoff

Berichter: Univ.-Prof. Dr.-Ing. Karl Alexander Heufer
Hon.-Prof. Dr.-Ing. Ali Gülhan

Tag der mündlichen Prüfung: 02.09.2024

Diese Dissertation ist auf den Internetseiten der Universitätsbibliothek online verfügbar.

Acknowledgement

„Nichts kann getan werden, es sei denn Schritt für Schritt“ – Charles Baudelaire

Für mich ist klar, dass ich ohne die Hilfe zahlreicher Personen den Weg der Promotion nicht geschafft hätte. Herrn Univ.-Prof. Dr.-Ing. Alexander Heufer möchte ich danken, dass er sich als Erstprüfer für mein Promotionsthema bereit erklärt hat.

Herrn Prof. Dr.-Ing. Ali Gülhan möchte ich besonders danken für die Möglichkeit, in einem sehr spannenden Themenbereich experimentelle Methoden frei auszuprobieren und zu untersuchen, für die breite Unterstützung zum Ausbau verschiedener Testanlagen, sowie für die zahlreiche Hilfe bei der Ausarbeitung mehrerer Publikationen. Herrn Dipl.-Ing. Dominik Neeb danke ich sehr für die vielen Stunden, in denen er für meine Themen, aber auch für meine Sorgen, ein offenes Ohr hatte und meine sprachliche Umsetzung ins Englische unterstützt hat. Mein Dank geht an die Kollegen, die mir immer wieder bei der Ausarbeitung dieser Arbeit wertvolle Anregungen zur Analyse und zur Strukturierung gegeben haben, allen voran Herrn Ansgar Marwege M.Sc., Herrn Patrick Seltner M.Sc. und Herrn Dipl.-Ing. Daniel Kirchheck. Außerdem danke ich Herrn Christian Hantz M.Sc. für seine Hilfe bei der Durchführung von TAU Simulationen sowie für das Geradebiegen verschiedener Formulierungen in der englischen Sprache.

Ich danke meinen Eltern für die Möglichkeiten, die sie mir gegeben haben, das Studium der Raumfahrttechnik unabhängig zu erleben. Ein großes Dankeschön geht an die zahlreichen Freunde und Verwandte, die mir immer Mut zugesprochen haben und felsenfest von meinem Promotionserfolg überzeugt waren.

Mein größter Dank geht an meine Frau Jana, die mir das wissenschaftliche Arbeiten beigebracht hat, die mich aufgebaut hat in den Momenten, in denen ich selbst nicht an mich geglaubt und gezweifelt habe, und die mich immer unterstützt und ermutigt hat, weiter zu machen.

Ich liebe dich!

Abstract / Übersicht

Dust particles in supersonic flows may cause significant increases of heat flux augmentation. These effects are called ‘particle-induced heat flux augmentation’ or ‘heating augmentation’ in the scientific community. The modelling approaches of these effects are based on a limited database and required several particle-related assumptions, since corresponding experiments are complex.
New experiments were conducted to increase the heating augmentation database. A small test facility was conceived, set up, and characterised. Non-intrusive measurement techniques were tested and developed to characterize individual particles in front of- and within the shock layer. The new measurement technique developments were able to underline and to refute assumptions regarding heating augmentation. Furthermore, these developments improve significantly the accuracy of particle flux investigations in general.

Partikel-beladene Überschallströmungen haben signifikante Aufheizungseffekte auf Proben sowie auf Raumtransportsysteme. Diese Aufheizungseffekte werden in der Fachwelt „particle-induced heating augmentation“ (Aufheizungsverstärkung durch Partikel) genannt. Die Modellierung und die Vorhersage solcher Effekte ist nach dem aktuellen Stand der Technik komplex und basiert lediglich auf eine geringe Anzahl an Experimenten. Um diese Datenbank zu erweitern wurden neuartige Versuche durchgeführt. Hierzu wurde zunächst eine kleine Versuchswindkanalanlage konzipiert, aufgebaut und charakterisiert. Es wurden optische nicht-intrusive Messtechniken weiterentwickelt, die es ermöglichen, einzelne Partikel vor und innerhalb der Stoßschicht individuell zu untersuchen. Diese Weiterentwicklungen konnten nicht nur bisherige Annahmen zum Thema „heating augmentation“ bekräftigen bzw. wiederlegen, sondern können auch die Genauigkeit von Partikeluntersuchungen im Allgemeinen signifikant erhöhen.

Contents

Acknowledgement iii

Abstract / Übersicht v

List of Figures xi

List of Tables xv

List of Abbreviations xvii

1. Introduction 1
1.1. Purposes and Structure 3
1.2. Published Content 3

2. State-of-the-Art 5
2.1. Physical Effects 5
2.1.1. Convective Heat Flux Increases 6
2.1.2. Particle Impact and Direct Energy Transfer 8
2.2. Heating Augmentation Dependencies 9
2.2.1. Flow-related Dependencies 9
2.2.2. Probe-related Dependencies 10
2.2.3. Particle-related Dependencies 10

3. Fundamentals 13
3.1. Heating Augmentation Modelling 13
3.2. Shadowgraphy 13
3.3. Particle Image Velocimetry (PIV) 16
3.3.1. PTV from PIV correlation 18
3.4. Test Facility GBK 18
3.4.1. GBK Measurement Setup 19
3.4.1. Probe Installation 24
3.4.2. Operation Range 25
3.5. General Optical Measurement Setup 27
3.6. Particles 30
3.7. Gas Constants 35
3.8. Material Constants 36

4. Flow Analysis of the GBK Facility 37
4.1. Purposes & Structure 37
4.2. Methods 38

4.2.1. Test Facility Setup 38
4.2.2. Non-Intrusive Measurement Technique Setup 38
4.2.3. Test Conditions 39
4.2.4. Formulation of Turbulence Intensity 39
4.2.5. PIV and PTV Data Processing 41
4.3. Analysis 43
4.3.1. GBK Flow Stability and Flow Field 43
4.3.2. Measurement Uncertainty Estimation 45
4.3.3. Flow Turbulence Intensity 48
4.4. Conclusion 49

5. Individual Particle Characterization 51
5.1. Purposes & Structure 51
5.2. Methods 52
5.2.1. Test Facility Setup 52
5.2.1.1. Total Particle Mass 53
5.2.2. Optical Setup 54
5.2.3. Test Conditions 55
5.2.4. Particle Flux Calculation Formulations 57
5.2.5. Measurement Approaches 60
5.2.5.1. Shadowgraphy Approach 60
5.2.5.1.1. Particle Size Determination 62
5.2.5.1.2. Measurement Volume Thickness 66
5.2.5.1.3. Velocity Measurement 67
5.2.5.1.4. Data Filtering 68
5.2.5.2. PTV Approach 68
5.2.5.2.1. Velocity Measurement 68
5.2.5.2.2. Particle Size Determination 69
5.2.5.2.3. Measurement Volume Thickness 71
5.2.5.2.4. Data Filtering 71
5.2.5.2.5. Mass Flow Rate Scaling 72
5.2.5.3. Scattered Light Intensity Approach 72
5.3. Analysis 73
5.3.1. Particle Velocities at the Nozzle Exit 73
5.3.2. Particle Density Analysis 76
5.3.3. Particle Size Distributions 77
5.3.4. Particle Mass Flow Rate 79
5.3.4.1. Uncertainty 80
5.3.4.2. Profiles at the Nozzle Exit 82
5.3.4.3. Quantitative Comparison 84
5.4. Conclusion 86

6. Particle-Induced Heating Augmentation 89
6.1. Purposes & Structure 89
6.2. Methods 90
6.2.1. Shadowgraphy 90
6.2.2. Test Conditions and Test Types 92
6.2.3. Probe Shape 94
6.2.4. Stagnation Point Heat Flux 95
6.2.4.1. Theoretical Stagnation Point Heat Flux 95
6.2.4.2. Experimental Stagnation Point Heat Flux 97
6.2.5. Particle Reflection Mode 98
6.2.6. Modelling of the A_{kin} Coefficient 98
6.3. Analysis 99
6.3.1. Heat Flux in Particle-Free Flows 99
6.3.2. Energy Flux of Incident Particles 101
6.3.3. Energy Flux of Rebounded Particles 105
6.3.4. A_{kin} Coefficient 105
6.3.5. Heat Flux in Particle-Laden Flows 111
6.4. Conclusion 113

7. Summary and Outlook 117

8. Appendix 119
8.1. Overview of Experimental Particle-Induced Heating Augmentation Analysis 119
8.2. Overview Particle Sizing with Shadowgraphy 123
8.3. Drag Correlation 128
8.3.1. General 128
8.3.2. Henderson Drag Correlation 128
8.3.3. Parmar Drag Correlation 130
8.3.4. Loth Drag Correlation 132

9. References 135

List of Figures

Fig. 1 Aerothermal heating of a capsule during the atmospheric re-entry / descent phase 1
Fig. 2 Visualization of phenomena occurring in supersonic two-phase flows around a hemispherical shaped probe 6
Fig. 3 Principal procedure of a shadowgraphy's depth-of-field-calibration (adapted from [56]) .. 15
Fig. 4 Calibration dots analysed with LaVision Particlemaster – Shadowgraphy: a) z = 0.0 mm, b) z = -1.0 mm, c) z = -2.0 mm 15
Fig. 5 General setup and principle of PIV (adapted from [65]) 17
Fig. 6 Principal procedure of the PIV technique (cross-correlation) (adapted from [66]) 18
Fig. 7 Sketch of the GBK facility 19
Fig. 8 Sectional side view of the GBK measurement setup 20
Fig. 9 The maximum stagnation pressure p_0 depends on the stagnation temperature T_0, following DIN EN 1092-1 21
Fig. 10 Geometric details of the particle injection 22
Fig. 11 The maximum achievable nozzle exit diameter depends on the chosen Mach number and is limited by the lowest achievable test chamber pressure p_a, the maximum stagnation pressure p_0 and stagnation temperature T_0, as well as by the minimum cross section $A_{GBK\ crit}$ of the GBK facility 23
Fig. 12 Sketch of the probe setup. Nozzle, diffusor and particle chamber are not shown 24
Fig. 13 Sketch of probe setup, dimensions given in mm 25
Fig. 14 Relation between p_0, p_a, and probe position for the presented GBK facility and measurement setup 26
Fig. 15 Operation range of GBK facility at Ma = 2.1 27
Fig. 16 Front view on the PTV and shadowgraphy setup, dimensions given in mm 28
Fig. 17 Photograph of the general camera setup 28
Fig. 18 Photograph of the laser optics 29
Fig. 19 Sketch of the complete scientific setup for all following analyses 30
Fig. 20 Cumulative and differential particle number distribution of PIV-MgO particles, measured with a 'S3500' by Microtrac Gmbh 32
Fig. 21 Cumulative and differential particle volume distribution of PIV-MgO particles, measured with a 'S3500' by Microtrac Gmbh 32
Fig. 22 Cumulative and differential particle number distribution of Al_2O_3 particles, measured with a 'PartAn SI' by Microtrac Gmbh 33
Fig. 23 Cumulative and differential particle volume distribution of Al_2O_3 particles measured with a 'PartAn SI' by Microtrac Gmbh 33
Fig. 24 Cumulative and differential particle number distribution of MgO particles measured with a 'PartAn SI' by Microtrac Gmbh 34
Fig. 25 Cumulative and differential particle volume distribution of MgO particles measured with a 'PartAn SI' by Microtrac Gmbh 34

Fig. 26 Inverted PIV Images of C2 and C3, showing the overlap FOV as central rectangle between dotted lines 42
Fig. 27 Stagnation pressure p_0 peaks and stagnation temperature T_0 peaks are caused by the switch of the three-way-ball-valve (before and after the red dashed lines, test run V60) 44
Fig. 28 Normed difference of measured temporal mean and theoretical particle velocity, run V60, IW ~ 0.3 mm (C2: 64 px, C3: 12 px) 45
Fig. 29 Velocity histogram of C2, run V60 46
Fig. 30 Velocity histogram of C3, run V60 46
Fig. 31 Measurement uncertainty for C2 and C3 in relation to the chosen IW size 47
Fig. 32 Measured turbulence intensity for C2 and C3 in relation to the IW size, run V60 48
Fig. 33 Relation between total particle mass loss in the seeding device and the particle mass, collected with the injection collection probe 54
Fig. 34 Sketch of FOVs: shadowgraphy FOV (blue), PTV FOV (red). Only data in front of the shock is evaluated (shadowgraphy: purple) 55
Fig. 35 Sketch of volume-of-interest (VOI) for G_p determination 58
Fig. 36 Sketch of shadowgraphy (red), PTV (blue), and scattered light intensity (green) measurement procedures for G_p determination 60
Fig. 37 Gray-levels of differently sized shadows, adapted from [45]. Graphical definitions of BiThr and GS are included 61
Fig. 38 Relation between detected size, true size and gradient slope GS 63
Fig. 39 'Rainbow plot': correlation between detected dot size, GS, true dot size and assigned correct dot size 64
Fig. 40 Count efficiency vs. z-position, BiThr = 13 % and NorRad = 10 px, C1 67
Fig. 41 Relation between $d_{GS\ min}$ and $d_{CE=1}$, depending on calibration dot size. $d_{CE=1}$ is always larger than $d_{GS\ min}$ 67
Fig. 42 Adapted PTV velocity uncertainty for different particle velocities across the entire nozzle exit, C3 69
Fig. 43 PTV's particle size uncertainty vs. estimated particle size 70
Fig. 44 PTV light sheet thickness for both laser pulses at different y-positions 71
Fig. 45 Nozzle contour and Mach Number contours along the nozzle axis, calculated with different methods 74
Fig. 46 Particle velocity vs. particle size 2.5 mm downstream of the nozzle exit, assuming different drag models and particle densities 75
Fig. 47 Particle size distribution, Al_2O_3, run A-32-1-akin 78
Fig. 48 Particle size distribution, MgO, run M-32-1-akin 78
Fig. 49 Particle size distribution, SiO_2, run S-32-1-akin 79
Fig. 50 Particle mass flow rate profiles, run A-32-1-akin, p_0 = 0.952 MPa, T_0 = 374.5 K, Al_2O_3 82
Fig. 51 Particle mass flow rate profiles, run M-32-1-akin, p_0 = 0.950 MPa, T_0 = 373.5 K, MgO 83
Fig. 52 Particle mass flow rate profiles, run S-32-1-akin, p_0 = 0.952 MPa, T_0 = 374.0 K, SiO_2 83

Fig. 53 Comparison of G_p in the y-range of -2.4 to 2.4 mm, measured with the scattered light intensity approach and shadowgraphy 85
Fig. 54 Comparison of G_p in the y-range of -2.4 to 2.4 mm, measured with the scattered light intensity approach and the PTV approach 86
Fig. 55 Comparison of G_p in the y-range of -2.4 to 2.4 mm, measured with the scattered light intensity approach and the scaled PTV approach 86
Fig. 56 Sketch of shadowgraphy's FOV: 'freestream' analysis area (purple) in front of the bow shock, while the 'shock layer' analysis area contains the entire shock layer (orange) 91
Fig. 57 Temperature time curve of the coaxial-thermocouple (purple: front, red: back) and the facilities' T_0 of test run A-32-1-akin 94
Fig. 58 Probe shape during the test series, horizontal (y = 0 mm) and vertical (z = 0 mm) profile 95
Fig. 59 Differences between measured stagnation point heat flux, A-32-1-akin, and an approximation, based on the equations of [85] and the probe temperature T 101
Fig. 60 Comparison of temporal mean of approximated and experimentally determined stagnation point heat fluxes 101
Fig. 61 Relation between particle velocity, size, and the kinetic energy of incident particles in the freestream and in the shock layer, run ID A-32-1-akin 103
Fig. 62 Relation between particle velocity, size, and the kinetic energy of incident particles in the freestream and in the shock layer, run ID M-32-1-akin 103
Fig. 63 Relation between particle velocity, size, and the kinetic energy of particles, run ID S-32-1-akin 103
Fig. 64 Significance of rebounded particle kinetic energy flux, compared to incident particle kinetic energy flux for all 'akin'-type tests 105
Fig. 65 Temporal change of θ for all 'akin'-type tests with Al_2O_3 particles 106
Fig. 66 Temporal change of $\dot{e}_{kin\ inc\ sl}$ for all 'akin'-type tests with Al_2O_3 particles 107
Fig. 67 The a_{kin} coefficient vs. relative stagnation point temperature θ 108
Fig. 68 Measured a_{kin} coefficient vs. Re_{dProbe} for all tests 110
Fig. 69 Kinetic energy flux of incident particles of the 'qsum'-type tests made with Al_2O_3 111
Fig. 70 Ratio of stagnation point heat fluxes in particle-laden and particle-free flows vs. the particle mass concentration c_m for all 'qsum'-type tests. Black-filled data are taken from [11] and were measured with hemispherical-shaped probes 112

List of Tables

Table 1 Overview of physical effects in terms of particle induced heating augmentation 5
Table 2 Summary of a_{kin} coefficients from literature 9
Table 3 General limitations of the GBK facility without measurement setup 19
Table 4 Characteristic diameters of particles used for PIV applications 34
Table 5 Characteristic diameters of particles used for heating augmentation analysis 35
Table 6 Gas constants 35
Table 7 Probe and coaxial thermocouple material properties 36
Table 8 Flow conditions for turbulence intensity measurements 39
Table 9 Maximum differences between measured and calculated velocities 45
Table 10 Measurement uncertainty for all cameras 47
Table 11 Determined flow turbulence intensities for investigated flow conditions 49
Table 12 Test matrix, sorted by particle material, T_0, and p_0 56
Table 13 Final detection parameters of LaVision DaVis ParticleMaster Shadowgraphy 61
Table 14 Size uncertainty before and after additional correction for shadowgraphy, C1 65
Table 15 Overview of applied filters on shadowgraphy data 68
Table 16 Overview of applied PTV data filters 72
Table 17 Pycnometer measurement results 77
Table 18 Parameter variation effects on shadowgraphy's G_p. The parameter variation has more influence on G_p than the estimated uncertainty based on individual particle parameter uncertainties 81
Table 19 Relative particle mass flow rate uncertainties of all measurement approaches 82
Table 20 Overview of applied filters to detect incident particles 92
Table 21 Overview of applied filters to detect rebounded particles 92
Table 22 Test matrix, sorted by particle material, T_0, and p_0, and test type 92
Table 23 Parameter range for which the Fay-Riddell approximation was established 96
Table 24 V_{p*} for all particle / probe material combinations 98
Table 25 Estimated a_{kin} coefficient for elastic reflection and for all particle/probe material combinations. The right term of eq. (6-9) was used for computation 99
Table 26 Kinetic energy flux reduction due to particle deceleration within the shock layer, test type 'akin' 104
Table 27 Measured a_{kin} coefficients for $t \leq 0.5$ s 109
Table 28 Summary of measured heat flux ratios in particle-laden supersonic flows 113

List of Abbreviations

$\dot{e}_{kin\ inc}$	*kinetic energy flux of incident particles [kW/m^2]*
$\dot{e}_{kin\ reb}$	*kinetic energy flux of rebounded particles [kW/m^2]*
$\dot{q}_0$	*stagnation point heat flux in a particle-free flow [kW/m^2]*
$\dot{q}_a$	*direct energy transfer from particles into the probe [kW/m^2]*
$\dot{q}_{FR}$	*stagnation point heat flux, approximated with the equations of Fay-Riddell [kW/m^2]*
$\dot{q}_{SP}$	*stagnation point heat flux [kW/m^2]*
$\dot{q}_\Sigma$	*stagnation point heat flux in a particle-laden flow [kW/m^2]*
Δt_{jitter}	*double-pulse time stability/variation of the laser system [ns]*
$\Delta X'_{PIV\ Unc}$	*PIV measurement uncertainty [px]*
Δt	*double-pulse time seperation of PIV laser [ns]*
$A_{GBK\ crit}$	*minimum cross section of GBK main flow [mm^2]*
a_{heat}	*thermal energy conversion efficiency coefficient [-]*
a_{kin}	*kinetic energy conversion efficiency coefficient [-]*
BiThr	*shadowgraphy binarization threshold [%]*
BS	*beam splitter*
C_1	*recombination rate parameter [-]*
C_D	*drag coefficient [-]*
CE	*count efficiency [-]*
c_m	*particle mass concentration [-]*
$c_{p\ gas}$	*specific heat [J/(kg K)]*
c_p	*specific heat of particles [J/(kg K)]*
$d_{GS\ min}$	*shadowgraphy measurement volume thickness, limited by the minimum GS boundary [mm]*
DAQ	*data acquisition system*
$d_{CE=1}$	*shadowgraphy measurement volume thickness in which CE = 1 [mm]*
DOF	*depth-of-field*
d_p	*particle diameter [µm]*
$d_{p\ detected}$	*detected particle size with DaVis, without additional size correction [µm]*
$d_{p\ corrected}$	*particle (or calibration dot) diameter, corrected with the help of the additional size correction [µm]*
$d_{p\ limit}$	*particle-induced heating augmentation related limiting particle diameter [µm]*
$d_{p\ min}$	*shadowgraphy's minimum detectable particle size [µm]*
$d_{p\ min,\ full}$	*shadowgraphy's minimum detectable particle size which can be fully detected [µm]*
$d_{p\ True}$	*a-priori known true calibration dot diameter [µm]*
d_{PTV}	*laser light sheet thickness [mm]*
d_{shadow}	*shadowgraphy's measurement volume thickness [mm]*
E	*Young's modulus [GPa]*
E_j	*Young's modulus of the j-th material [MPa]*
GBK	*multi-phase flow facility ("Gemischbildungskanal")*
G_p	*particle mass flow rate [kg/(m^2 s)]*

$G_{p\ PTV}$	*particle mass flow rate, based on PTV data [kg/(m² s)]*
$G_{p\ PTV\ scaled}$	*particle mass flow rate, based on PTV data, scaled to $M_{p\ Nozzle}$ [kg/(m² s)]*
$G_{p\ scatter}$	*particle mass flow rate, based on scattered-light intensity [kg/(m² s)]*
$G_{p\ scatter\ qual.}$	*particle mass flow rate, based on scattered light intensity, qualitative [kg/(m² s)]*
GS	*normalized intensity decrease per pixel at the detected particle/dot rim [%]*
GS_{max}	*maximum gradient slope per size class $d_{p\ True}$ [%]*
H	*simulated flight altitude in terms of the Fay-Riddell approximation [m]*
h_D	*dissociation enthalpy of the gas phase [J/kg]*
h_{0e}	*total gas enthalpy at the boundary layer edge [J/kg]*
h_w	*gas enthalpy at the stagnation point wall [J/kg]*
IQR	*interquartile range*
IW	*PIV interrogation window size [px²]*
Le	*Lewis number [-]*
L_x	*dimension of VOI in x-axis [mm]*
L_y	*dimension of VOI in y-axis [mm]*
Ma_∞	*free stream Mach number [-]*
Ma_p	*relative particle Mach number [-]*
minimum GS offset	*limiting gradient slope for infinitesimal small detected particle diameters [%]*
MOC	*Methods-of-Characteristics*
m_p	*particle mass [kg]*
$M_{p\ calc}$	*calculated total particle mass [g]*
$M_{p\ collected}$	*total particle mass collected with the injection collection probe and the closed container [g]*
$M_{p\ nozzle}$	*total particle mass passing the nozzle [g]*
NorRad	*shadowgraphy normalization radius [px]*
n_p	*all particles within VOI at a specific time [#]*
p_0	*stagnation pressure [MPa]*
p_{02}	*stagnation pressure in the shock layer [MPa]*
p_∞	*static pressure in the freestream [Pa]*
p_a	*test chamber pressure [MPa]*
p_s	*static pressure at the stagnation point [Pa]*
PIV	*Particle-Image-Velocimetry*
PpV	*particle number concentration (Particles-per-Volume) [1/m³]*
PTV	*Particle-Tracking-Velocimetry*
Re_∞	*unit flow Reynolds number [1/m]*
$Re_{\infty\ dp}$	*free stream Reynolds Number, related on particle size [-]*
$Re_{\infty 1m}$	*freestream Reynolds number, based on 1 m [-]*
Re_p	*relative particle Reynolds Number [-]*
SF	*scale factor [px/mm]*
T	*stagnation point surface temperature [K]*
T_0	*flow stagnation temperature [K]*

T_{back}	*temperature at coaxial thermocouple's back end [K]*
t_{meas}	*evaluation time in which shadowgraphy and PTV images are considered for processing [s]*
T_p	*particle temperature [K]*
T_{rec}	*recovery temperature [K]*
T_e	*gas temperature at the boundary layer edge [K]*
Tu	*turbulence intensity [%]*
T_w	*probe wall temperature [K]*
u	*velocity component in x-direction [m/s]*
u'	*velocity fluctuation in x-direction [m/s]*
v	*velocity component in y-direction [m/s]*
v'	*velocity fluctuation in y-direction [m/s]*
V'_{Laser}	*velocity fluctuation caused by the laser jitter [m/s]*
V'_{meas}	*velocity fluctuation measured with PIV [m/s]*
$V'_{PIV\ Unc}$	*velocity fluctuation caused by measurement technique uncertainty [m/s]*
V'_{Tu}	*velocity fluctuation caused by flow turbulence [m/s]*
V_g	*gas velocity [m/s]*
VOI	*Volume of Interest*
V_p	*mean particle velocity [m/s]*
V_{p*}	*limiting impact velocity [m/s]*
VSR	*Particle Velocity-Size-Relation*
V_{theo}	*theoretical gas velocity at the nozzle exit [m/s]*
X	*x-position of VOI [mm]*
Y	*y-position of VOI [mm]*
Δ	*shock stand-off distance [mm]*
$\Delta\dot{q}$	*increase of convective stagnation point heat flux due to the presence of particles [kW/m²]*
$\Delta M_{seeding\ device}$	*mass difference of seeding device before and after each run [g]*
Δt	*double-pulse time separation [ns]*
ΔX	*shift of particle between the two PIV images [px]*
$\varepsilon_{dp\ PTV}$	*particle size error of PTV system [µm]*
θ_t	*stagnation point surface temperature difference at time t_i and at time t_0* [K]
$\lambda/2$	*half-wave plate*
μ_s	*dynamic viscosity of the gas in the shock layer at stagnation point temperature [kg/(m s)]*
μ_w	*dynamic viscosity of the gas in the shock layer at wall temperature [kg/(m s)]*
ρck	*coaxial thermocouple material constant $[(W^2s)/(m^2K^2)]$*
ρ_g	*gas density $[kg/m^3]$*
ρ_j	*density of the j-th material $[kg/m^3]$*
ρ_p	*particle density $[kg/m^3]$*
ρ_e	*gas density at the boundary layer edge $[kg/m^3]$*
ρ_w	*gas density in the shock layer at wall temperature $[kg/m^3]$*
σ	*Yield strength or elastic limit of material [GPa]*

σ_p .... *particle's elastic limit [MPa]*

σ_s .... *elastic limit of the probe's material [MPa]*

1. Introduction

67 years ago, humans have launched the first space probe 'Sputnik' into space. Its regular beeping in low Earth orbit was the start signal of the 'space race', in which not only humans were brought into space, but also spacecraft missions were developed to reach the Moon, Mars, Venus, and other far-away destinations.

Interplanetary unmanned spacecrafts can be divided into two groups: orbiters and landers. Focussing on the mission flight profile, orbiters have to re-manouver their hyperbolic arrival orbit into an elliptic or circular orbit around the celestial body of interest. The landers' mission flight profile contains the descent phase and the landing on the celestial body, at which the spacecraft has to decelerate from enormous entry speeds to an appropriate landing speed. These flight phases are considerably complex and risky. As an example, only 10 of 17 Mars landers reached Mars' surface successfully [1].

The only possibility to lower speed in non-atmospheric environments is the firing of landing thrusters. Landing on a body with atmosphere like Venus, Mars, or Saturn's moon Titan, provides the advantage to lower the landing speed by means of aerobraking and by the use of parachutes on the one hand, which reduces the amount of required landing thruster propellant. As a positive effect, the maximum scientific payload mass can be increased, assuming that the maximum spacecraft's mass is limited by the used launch vehicle. On the other hand, high aerothermal loads can be reached, requiring a thermal protection system to avoid critical heating of the lander and to avoid a possible mission failure. An illustration of a spacecraft during the atmospheric descent phase is exemplarily shown in **Fig. 1**.

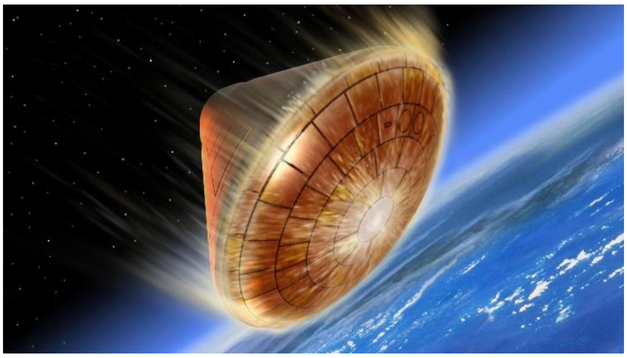

Fig. 1 Aerothermal heating of a capsule during the atmospheric re-entry / descent phase[1]

In terms of interplanetary missions to Mars, spacecraft designers have to consider also dust impact on aerothermal heating and material erosion during Martian atmospheric entry [2]. Larger dust particles in the range of 5 to 10 µm remain in the upper Martian atmosphere up to 50 days after a major dust storm [3]. A detailed knowledge about heating augmentation effects is essential for optimum spacecraft design, since an oversized thermal protection system increases spacecraft mass, while an undersized thermal protection system may lead to critical heating of the spacecraft. In the early 70's, stagnation point heat fluxes in particle-laden supersonic and hypersonic flows were measured first to be far in excess of heat fluxes in particle-free flows [4]. This heat flux increase is called 'particle-induced heat flux augmentation' or 'heating augmentation'.

---

[1] https://www.dlr.de/de/bilder/2012/1/raumkapsel-beim-wiedereintritt-in-die-erdatmosphaere_4825/@@images/image-2000-e8562e8053475c954aaea22fa960cd95.jpeg

The particle mass concentration c_m, the particle mass flow rate G_p, the kinetic energy flux of incident particles $\dot{e}_{kin}$, as well as the conversion efficiency of kinetic energy of particles into thermal energy, also called a_{kin} coefficient, are fundamental parameters to describe two-phase flows and heating augmentation effects (see **eq. (3-2)**). All these parameters are correlating with each other (see **eqs. (5-4)**, **(5-5)**, and **(5-6)**). Especially the a_{kin} coefficient can only be derived from particle mass flow rate measurements, or more specifically, from kinetic energy flux measurements.
There is only a limited number of experimentally determined a_{kin} coefficients for a limited number of materials (see **Table 1**). Many particle-induced heating augmentation studies, among them [5-10] are based only on the a_{kin} results of [11]. An extension of experimentally determined a_{kin} coefficients in supersonic particle-laden flows is therefore of high importance.

In the past, most of the experimental campaigns determined an average mass flow concentration for each run by dividing the particle discharge of the facility seeding system by the test time and the flow cross section area [10-13]. This procedure assumes that no particles remain in the facility, and that G_p is constant over time and over the flow cross section. Nonetheless, the authors of [11] reported significant variations in G_p occurred during some runs. In [13], time and spatial resolved particle mass flow rates were determined by measuring a particle scattering signal in front of the probe. In that study, it was concluded that the particle mass flow rate is constant across the flow section. However, for smaller facilities, as it was shown in [12], G_p is higher close to the symmetry axis. A kind of a particle catcher probe was often used during pre-tests as an additional calibration measurement method for levelling the average c_m for each run, but no indication of the capturing efficiency was given in any study. Generally, there is no reference technique for e.g. particle mass flow rate determination.
G_p correlates strongly with particle size (see **eq. (5-4)**). However, all of the studies provide only the nominal mean particle sizes, which were measured before insertion into the wind tunnel facilities. The study described in [12] is the only one which additionally analysed captured particle sizes. The study measured a particle size decrease, which is stated to be a consequence of particle break-up. Particle velocity was determined experimentally only in some of the studies [4, 12]; most of the studies defined it with analytical formulations. The question arises of how accurate these analytics are, since comparisons made in [4, 14] have indicated discrepancies.
A comprehensive overview of selected experimental particle-induced heating augmentation studies is given in **Table A 1**.

In summary, there is no data set related to heating augmentation in supersonic flows up to now, where all particle characteristics, namely number, size, and velocity, were measured simultaneously, although all of them affects G_p and hence, $\dot{e}_{kin}$ and the a_{kin} coefficient.

1.1. Purposes and Structure

The main focus of this work is to develop a method to determine all relevant particle characteristics and to increase the accuracy of particle flow measurements. Particle fluxes are determined with individual particle characterization techniques, among them is shadowgraphy. The state-of-the-art shadowgraphy requires additional complex correction procedures to analyse particle size and velocity in the range of 5 to 100 µm and up to 700 m/s within supersonic shock layers. A shadowgraphy correction procedure is developed and validated. Its measurement uncertainties are derived following linear error propagation theory. The derived particle fluxes are compared to different developed measurement approaches, since there is no reference technique for e.g. particle mass flow rate determination.

With the help of this individual particle characterization method, the experimental data base regarding particle-induced heating augmentation is extended. Especially the conversion efficiency of kinetic energy of particles into thermal energy, also called a_{kin} coefficient, is analysed in detail and compared to existing values and modelling approaches from literature. The particle deceleration and rebound within the shock layer are measured to increase the accuracy of the resulting a_{kin} coefficient.

This work is organized as follows: First, a fundamental flow analysis is made of the test facility, which was specially-designed for the establishment of individual particle characterization methods. These new methods and procedures are tested and validated by comparing particle size distributions to state-of-the-art measurement devices and by comparing particle mass flow rates to each other. Finally, stagnation point heat fluxes in particle-free and particle-laden flows are determined and the impact of particle fluxes on heating augmentation as well as on the a_{kin} coefficient are investigated. The experimental data is compared to existing data and modelling approaches regarding particle-induced heating augmentation.

1.2. Published Content

This work includes the scientific content of three published journal research articles.

The first published research article [15] focussed on the establishment of shadowgraphy correction algorithms and the general determination of particle mass flow rate and its measurement uncertainty from individual particle characteristics. Furthermore, measured particle velocities were compared to one-dimensional isentropic calculations, indicating significant discrepancies.

The second journal research article [16] included several measurement improvement suggestions and considered additional error sources of the shadowgraphy system. Particle mass flow rate measurement uncertainties of all implemented measurement procedures, namely shadowgraphy, Particle-Tracking-Velocimetry, and scattered light intensity, were derived. The particle mass flow rate analysis was extended to a large range of flow conditions of the test facility. Particle densities were analysed to explain discrepancies between measured and calculated particle velocities. Moreover, particle size distributions were compared qualitatively and quantitatively to state-of-the-art spectrometer measurements.

The third published work [17] used the refined shadowgraphy measurement procedure to determine the a_{kin} coefficient for three particle materials in several flow conditions. Particle deceleration and rebound effects within the shock layer were considered to reduce the number of common assumptions in heating augmentation literature. The found a_{kin} coefficients were compared to analytical formulations.

Beside the content of the above mentioned research articles, this work includes additional fundamental investigations in **section 4** as well as convective heating augmentation analyses in **section 6.3.5**.

2. State-of-the-Art

2.1. Physical Effects

A wide range of physical effects were identified to explain heating augmentation. These effects can be divided into two categories: convective heat flux increases from the gas phase to the probe due to the presence of particles, and the direct energy transfer of incident particles into the probe during impact [10, 11]. The identified effects are illustrated in **Fig. 2** and summarized in **Table 1**. While only the bottom right illustration (**Fig. 2 f**) belongs to the particle impact category, all other illustrated effects can be classified into the convective heat flux increase category. Both categories are described in detail in the respective subsections.

Table 1 Overview of physical effects in terms of particle induced heating augmentation

phenomenon	physical effect	literature
high particle mass concentration	- change in gas flow characteristics and Mach number	[12] [18]
rebounded particle accumulation in front of probe	- change in effective probe shape - change in particle reflection behaviour / shielding effect	[12] [18]
wake of rebounded particle within shock layer	- no significant heating effect	[19, 20]
rebounded particle just crosses bow shock	- generation of toroidal vortices → tubulisation of the boundary layer - disturbance of bow shock shape	[4, 11, 18]
rebounded particle crosses bow shock and penetrates into freestream	- conical shocks 'fluid cones' around particles - generation of shear layers and ring vortices by shock-shock interaction - ring vortices lead to short time heat flux increase	[18, 19, 21] [9]
particle impact on probe	- particle kinetic energy conversion into thermal energy	[9-11, 22]
inelastic reflection of particles	- erosion effects → increase of surface roughness - surface roughness increases convective heat flux	[4, 11, 23]
	- particle deformation	[24]
	- particle fragmentation	[25]

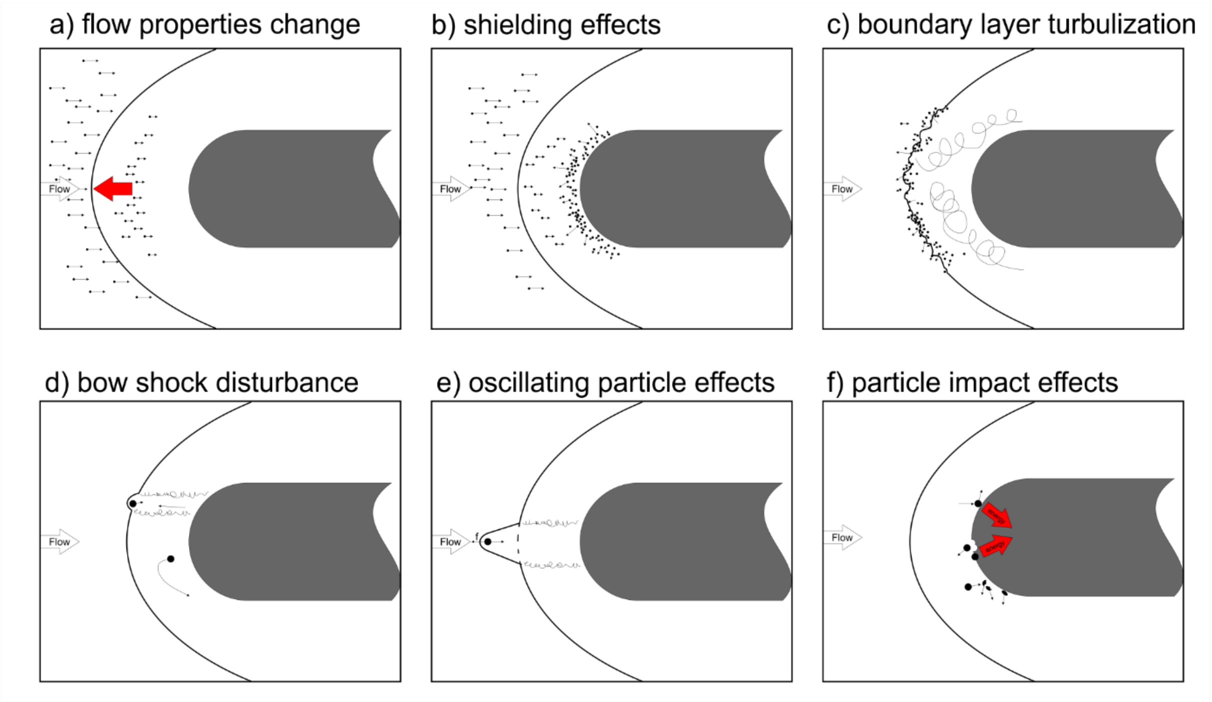
a) flow properties change
b) shielding effects
c) boundary layer turbulization
d) bow shock disturbance
e) oscillating particle effects
f) particle impact effects
Flow

Fig. 2 Visualization of phenomena occurring in supersonic two-phase flows around a hemispherical shaped probe

2.1.1. Convective Heat Flux Increases

The increase of the convective heat flux could have several reasons (see **Fig. 2**). In the following, the effects are discussed step-by-step.

An observed effect was a decrease of the freestream Mach number with increasing particle concentration, leading to a change in the shock stand of distance [12, 18] (see **Fig. 2 a**).

Observed changes in the bow shock structure was explained by particle accumulations in front of the probe, affecting the effective probe shape. This accumulation was fed by rebounded particles which did not crossed the bow shock after probe impact. The accumulation region size increased with particle mass concentration within the flow. The particle accumulation also acts like a shielding, attenuating the relation between particle mass concentration and heating augmentation [12] (see **Fig. 2 b**).

The presence of particles increase generally the boundary layer turbulence [21] (see **Fig. 2 c**), which again affects the convective heat flux.

While rebounded particles remaining within the shock layer did not increase heating or cause laminar boundary layer transition [19, 20], it was found that rebounded particles crossing the bow shock have significant impact on heating augmentation as well as on the bow shock structure (see **Fig. 2 d**). Strong bow shock perturbations were detected in tests made with coarse particles between 100 to 200 µm in size and with particle mass concentrations significantly smaller than 1 % [4, 11]. Especially the rebounded particles destroyed the bow shock [18]. This postulation was confirmed by tests with hollow probes. These probes decreased drastically the number of rebounded particles and the bow shock remained undisturbed.

A complex flow structure establishes if rebounded particles are crossing the bow shock after probe impact [18, 19], as illustrated in **Fig. 2 e**. After crossing the probe bow shock, a shock cone, also called 'fluid cone' in the literature, is established around the particle [11, 18, 19, 21]. A formulation to calculate the shock angle is given in [18]. The high pressure of the subsonic region can be transmitted to the supersonic part of the flow within the particle wake [11, 18]. With increasing distance between particle and probe, the link between the particle wake and the subsonic region reduces, till the original bow shock shape around the probe is restored. This process is highly unsteady in high particle concentration flow regimes as long as the probe bow shock reconstruction time is longer than the time interval between impacting and rebounded particles crossing the bow shock.

A shear layer is formed at the junction of the probe bow shock and the particle shock cone due to the abrupt change in shock curvature. This shear layer subsequently rolls up into a vortex ring as the particle is driven back into the shock layer. After approaching the surface, the vortex ring is moved toward the model and expands in radial direction. When the vortex ring passed the heat transfer gages, an increased heat flux was registered by 1.5 to 3 times the undisturbed value for a period of around 1 ms [19]. The authors explained the increased heating with an increased vorticity of the edge of the boundary layer, which is in agreement to the discussion made in [9]. In general, the overall flow behaviour fits well with so called 'Edney Type IV' or 'jet' shock-shock interactions.

The authors of [19] divided the effect of single rebounded particles crossing the probe bow shock into three classes:

1. The particle crosses the probe bow shock along the symmetry axis, but its maximum distance to the probe surface is less than 0.7 of the body diameter
2. same as 1), but the particle travels further than 0.7 of the body diameter before returning toward the body
3. the particle travels off center

For the first case, the above described shear layer reaches the model periphery just as the particle moves back towards the probe, collapses inwards a quasi-steady fashion and disappears when the particle re-enters the shock layer. The authors noted an increased heating for the time the particles needed to exit and re-enter the shock layer. At that point where the shear layer touched the probe, the pressure was measured to be above the pitot level. At points within the annulus the measured pressure could be roughly reconstructed by the compression through the conical particle shock. The movement of the particles were predictable with simple drag relations.

For the second case, the entire flow started to oscillate, similar to pulsating flows observed over spiked bodies or highly indented nose shapes (see **Fig. 2 e**). The non-dimensional frequency of these pulsations seemed to be independent of particle Mach number, particle velocity, penetration size and model size. The axial motion of the particle was strongly influenced by the oscillating flow. Due to oscillating shear layers, the recorded heat flux and pressure values also showed strong oscillations which provided 'surprising' regularity and persistence. The maximum heating rates measured at the edge of the cylinder probe were up to five times higher, the minimum heating rates were close to the values of the undisturbed flow. The particle movement can be described with drag relations until the flow starts to oscillate. After the oscillation process started, the particle motion was extremely complex. For the third case, highly asymmetric flows were detected, where no oscillations were observed.

2.1.2. Particle Impact and Direct Energy Transfer

Particle impacts on the probe have significant influence on heat flux augmentation [9, 11, 13, 21] (see **Fig. 2 f**). A detailed description of particle and probe deformation and the transferred energy into the probe for a single particle is made in [24]. Moreover, particles can fragment into smaller particles when impacting, also leading to more complex flow phenomena [25]. An approximation at which velocities particles made of different materials will break up can be found e.g. in [26]. Furthermore, impacting particles can collide with rebounded particles [14].

If the particle velocity exceeds a certain value at impact, no rebound from the probe surface occurs and the reflection can be termed erosive; otherwise it is elastic or partially elastic [14]. This critical value is called limiting impact velocity V_{p*} in the following and is defined as [14, 27]:

$$V_{p*} = \left[\frac{3}{\rho_p}\left(\frac{1}{\sigma_p} + \frac{1}{\sigma_s}\right)^{-1}\right]^{1/2} \tag{2-1}$$

The parameters ρ_p, σ_p and σ_s are the particle density, and the elastic limit of the particle and sample material, respectively.

Particle with higher impact velocity than V_{p*} are in the erosive reflection mode, while slower particles reflect elastic. An elastic reflection is described for example in [28] and strongly depends on the material properties of the probe and the particle, as well as on the impact velocity and the impact angle related to the surface.

In the case of inelastic reflection, erosive effects occur, leading to an increase of the probe surface roughness which again has effects on the convective heat transfer [4, 23].

When impacting, a part of the particle kinetic energy is converted into thermal energy [4, 10-12, 14]. A key parameter is the conversion efficiency of kinetic energy of particles into thermal energy, also called a_{kin} coefficient (see **eq. (3-2)**). The a_{kin} coefficient depends on particle, probe, and flow properties as well as on the reflection modus between particles and probe surface [6, 9, 14].

All a_{kin} coefficients from experimental literature are summarized in **Table 2**. The study of [11] provided the largest dataset of the a_{kin} coefficient, containing 20 measured values in the range of 0.5 to 0.9. They have made heating augmentation tests in a hypersonic Mach number 6.1 to 9.5 air flow regime and 100 to 200 µm large SiC and MgO particles. The achieved particle mass concentrations were in the range of 0.001 to 10 % [4, 11, 29]. The stagnation point heat flux was measured with back face thermocouples. The a_{kin} coefficient was derived from the calculated heat flux at that time at which the probe surface reached the gas stagnation temperature in a particle-laden flow. The authors of [12] measured an a_{kin} coefficient of 0.17 in a Mach number 2.3 combustion gas and nitrogen flow regime and 27 to 111 µm large SiO_2 particles. The particle mass concentration was up to 25 %. Both studies approximated the reduction of particle impact velocity in the shock layer and measured a time-averaged particle mass flow rate to calculate the incident particle kinetic energy flux.

Table 2 Summary of a_{kin} coefficients from literature

particle material	probe material	V_p at impact	reflection modus	a_{kin}	source	remarks
[-]	[-]	[m/s]	[-]	[-]	[-]	
SiC / MgO	6AL-4V titanium alloy	< 884	elastic	0.7±0.2	[11]	reflection modus named in [6]
-	-	-	erosive	0.3	[6, 9]	no reference explanation given
SiO_2	copper	564		0.17	[12]	-
SiO_2	copper	907	erosive	0.1	[14]	data from [12]

The authors of [14] have deduced a formulation to predict the a_{kin} coefficient in an elastic particle reflection environment. This formulation depends on the particle mass flow rate of incident, rebounded, and chaotized particles as well as on particle and probe material parameters. Chaotized particles are defined as incident particles colliding with rebounded particles. A simplified prediction formulation is discussed in **section 6.2.6**.

2.2. Heating Augmentation Dependencies

While the general physics of heating augmentation is addressed in **section 2.1**, this section is a summary of qualitative dependencies of flow-, probe-, and particle parameters on heating augmentation.

2.2.1. Flow-related Dependencies

The stagnation pressure p_0 has an proportional effect on the heating augmentation [13], which is explained in [9] by a square root dependence described in [30]. The authors of [13] measured a trend of increased heat flux augmentation in a pure nitrogen gas phase, while they detected a trend of decreased heat flux augmentation in a CO_2 gas phase. However, they have stated that the change of the gas phase has no essential effect on the heating augmentation. Unfortunately, no explanation was given for the observed trends.

A higher flow turbulence increases the stagnation point heat flux in particle-free flows [31], which also affects the ratio between stagnation point heat flux in particle-free and in particle-laden flows.

2.2.2. Probe-related Dependencies

The convective heating augmentation contribution is independent of the probe nose radius [4, 10]. The model geometry has no effect on the convective heating augmentation contribution [4] or can be reduced to a constant proportionality factor [10].
Similar levels of heating augmentation were found for metallic probes made of different materials, but slightly higher levels for graphite probes [4]. This difference is contributed to a higher level of probe surface roughness.
The effect of the surface roughness on the heating augmentation is not distinct. On the one hand, [4, 9] stated that it has only minor effects on the stagnation heat transfer. On the other hand, [32] reported that the probe surface has to be very smooth in order to avoid transitional effects in the nose tip area which increased significantly the measured heat flux. Moreover, [23] stated that surface roughness could be one disturbing effect responsible for heat flux augmentation. [13] have shown that particles smaller than 2 µm in diameter did not erode probes so no roughness effects could be observed.

Regarding the spatial heat flux distribution onto the probe surface, it is reported that the maximum heat flux rate is located in the near of the sound point in particle-free flows (angle from the stagnation point ~25° to 30°) [10, 11, 23]. While in [10, 23], this was explained by a laminar-turbulent transition of the boundary layer in a Mach number = 2.6 to 4.2 and $Re_{dProbe} = 0.4*10^6$ to $5*10^6$ flow, the authors of [11] noted that this behaviour is in agreement to turbulent boundary layer calculations and the consideration of surface roughness in a Mach number = 6.1, $Re_{dProbe} = 1.88*10^6$ flow. In particle-laden flows, the maximum heating rate is in the stagnation point [10, 11]. Following this observation, the maximum heating augmentation is in the stagnation region. Heating augmentation decreases sharply behind the sound point [10, 23].

2.2.3. Particle-related Dependencies

A linear dependence between particle mass concentration c_m and the heat flux augmentation is shown by [10, 13, 21, 23], although experimenters had issues with variable dust concentrations during the test time [11, 13].
If the particle mass concentration was increased above a certain point, a shielding effect of accumulated particles within the shock layer in front of the probe was observed, and the effect of the particle mass concentration on the heat flux augmentation relation is attenuated [12].

Heating augmentation is proportional to the particle diameter [12, 21], or to the square root of the particle diameter [10]. The authors of [13] found the particle inertia to be decisive for heating augmentation.
Heating augmentation effects were negligible for tests with particles in the size class of 25 µm and particle mass concentrations smaller than 0.5 to 1 % [18]. Negligible heating augmentation effects were also detected by [13] for silica particles with 0.15 µm in size and concentration up to 3 %, and by [12] for particles 0.23 µm in size and mass concentrations up to 7 %. To distinguish between

small non-impacting particles and large impacting particles, [9] has proposed a formulation for estimating a limit particle diameter $d_{p\ limit}$:

$$d_{p\ limit} \geq \frac{3\ C_D \rho_2\ V_2\ \Delta}{8\ \rho_p\ V_{p\ fs}} \tag{2-2}$$

While C_D is the particle drag coefficient, ρ_2 and V_2 are the gas density and the gas velocity within the shock layer, respectively. The distance between probe surface and bow shock is expressed by Δ. The parameters ρ_p and $V_{p\ fs}$ are the particle material density and the particle velocity in the freestream, respectively.
Following **eq. (2-2)**, the limiting particle diameter depends on particle- as well as on flow parameters. It must be noted that a comparison between $d_{p\ limit}$ and the above mentioned particle sizes, at which no heating augmentation was measured, cannot be made due to missing particle- and flow parameters in [18] [13] [12].

Most of the experimental studies supposed that a part of the particle kinetic energy impacting on the probe is transferred into thermal energy [4, 10, 11, 21] so that the heating depends on the squared particle impact velocity. [21] concluded, that small particles do not impact due to their negligible velocity lag. As a consequence, these have no contribution to the heating caused by kinetic energy conversion.

No experimental study had investigated the effect of particle temperature on heating augmentation. [12] noted that only kinetic energy is transmitted into the probe. In [10], the effect of particle temperature on the heating augmentation was neglected since the contact time of the particle and the probe is too short. For 50 µm sized aluminium particles with impact velocities in the range of 400 to 1000 m/s on a copper substrate [24] estimated this time to be 10^{-6} to 10^{-7} s.

No experimental study investigated in detail the effect of particle shape on heating augmentation [10, 11, 21]. The authors of [13] noted that impacting particles would not be perfect spherical and hence, a comparison between numeric and experiments can be erroneous. The study of [12] was the only one which investigated the particle shape within the incoming flow, concluding that the particle shapes were highly irregular.

3. Fundamentals

This section is a summary of how particle-induced heat flux augmentation can be formulated mathematically and which general test facility, measurement methods, and parameters were used in the analyses of **section 4** to **section 6**.

3.1. Heating Augmentation Modelling

A common formulation to describe heating augmentation is [10, 33]:

$$\dot{q}_{\Sigma} = \dot{q}_0 + \Delta\dot{q} + \dot{q}_a \tag{3-1}$$

The measurable stagnation point heat flux in a particle-laden flow $\dot{q}_{\Sigma}$ is the sum of the stagnation point heat flux in a particle-free flow $\dot{q}_0$, the increase of convective heat flux due to the presence of particles $\Delta\dot{q}$, and the direct energy transfer from particles into the probe $\dot{q}_{\mathrm{a}}$.

The direct particle energy transfer during impact $\dot{q}_{\mathrm{a}}$ can be described as the sum of the conversion of kinetic energy into thermal energy and the heat transfer due to differences between particle temperature T_p and probe surface temperature T:

$$\dot{q}_a = a_{kin} * (\dot{e}_{kin\,inc} - \dot{e}_{kin\,reb}) + a_{heat} * G_p * c_p * (T_p - T) \tag{3-2}$$

This formulation assumes that all particles have the same particle temperature during impact. The parameter a_{kin} is the energy conversion efficiency, also called accommodation coefficient or a_{kin} coefficient, describing the "effectiveness" of particle kinetic energy to be converted into probe heat. The values $\dot{e}_{kin\,inc}$ and $\dot{e}_{kin\,reb}$ are the kinetic energy flux of incident and rebounded particles. The factor a_{heat} and G_p are the thermal energy conversion efficiency coefficient and the particle mass flow rate of incident particles, respectively. The heat capacity of particles is described with the factor c_p.

The formulation of **eq. (3-2)** deviates from those given in literature [5, 13]. This is caused by the fact, that those studies assumed uniform particle sizes as well as uniform particle velocities at impact. The kinetic energy flux of rebounded particles $\dot{e}_{kin\,reb}$ is commonly neglected [10, 11], as well as the heat transfer aspect [10-12]. This can be reasoned by the short collision time of the particles with the probe surface [10, 34]. While the heat transfer aspect is also neglected, the kinetic energy flux of rebounded particles is investigated in **section 6** for the first time.

3.2. Shadowgraphy

One implemented measurement technique to characterize particles in this work is shadowgraphy. Multiple names have been used for this technique in the past: Shadowgraphy technique [35-38], particle droplet image analysis (PDIA) [35, 39-42], backlight photography [43], image processing technique [44, 45], image-based drop-sizing techniques [46], shadow imaging [47], or just imaging [48]. In the following, the term ‘shadowgraphy’ is used. The process of direct imaging of particles is a straightforward technique for determining velocity and size even of non-spherical particles. It measures the intensity decrease on a bright illuminated background, caused by particle shadows. The general intensity distribution of a particle shadow depends on its size and the defocus level [45]. Shadowgraphy’s main fields of application are the investigation of water or fuel injection spray processes (e.g. [35, 48, 49]), industrial process analyses (e.g. [50]) or the investigation of erosion processes (e.g. [51]).

Advantages of shadowgraphy are an economical setup, robustness, an easy optical alignment, a large dynamic range, and its ability to measure non-spherical particles. Furthermore, it is also capable to visualize shocks in supersonic flows. Its disadvantages are strong dependencies on the chosen image processing algorithm, especially the ambiguity of defining the perimeter of unfocused particles and the consideration of different measurement volume thicknesses (depth-of-field, DOF) for different particle sizes. These two aspects are the two major error sources by using shadowgraphy [52].

In general, the measurement process of shadowgraphy consists of three steps: image acquisition of calibration targets with well-defined size, image acquisition of the experiment to be examined, and image processing.

In a typical shadowgraphy calibration, a calibration target is moved on the optical axis of the recording device through the focus plane. The principal procedure of a typical shadowghraphy calibration is illustrated in **Fig. 3**. Herewith, a relation between defocus position and shadow appearance can be found, which strongly depends on the implemented optical arrangement (e.g. focal length or aperture) [44].

While the calibration was conducted with calibration dots on a glass target in most of shadowgraphy-related studies, also mono-disperse droplets were used [53-55]. A comparison between bubble-based and glass-target-based calibrations was made in [39], showing differences in the detected DOF.

Regarding image processing, particles are generally detected with the help of image binarization, applying different levels of gray-level thresholding. Due to the so called ‘depth-of-field effect’ and because particles do not exist only in the focal plane, focussed and unfocussed particle shadows are recorded and detected. The challenge of the depth-of-field effect is illustrated in **Fig. 4**. It shows a part of LaVision’s shadow calibration target. In the top left image, the calibration target was in focus (z = 0 mm), in the top right image (z = -1 mm) and in the bottom right image (z = -2 mm), it was moved out of focus. The blue circles indicate detected particles or dots, respectively. Unfocussed particles were sized and shaped incorrectly at high magnifications.

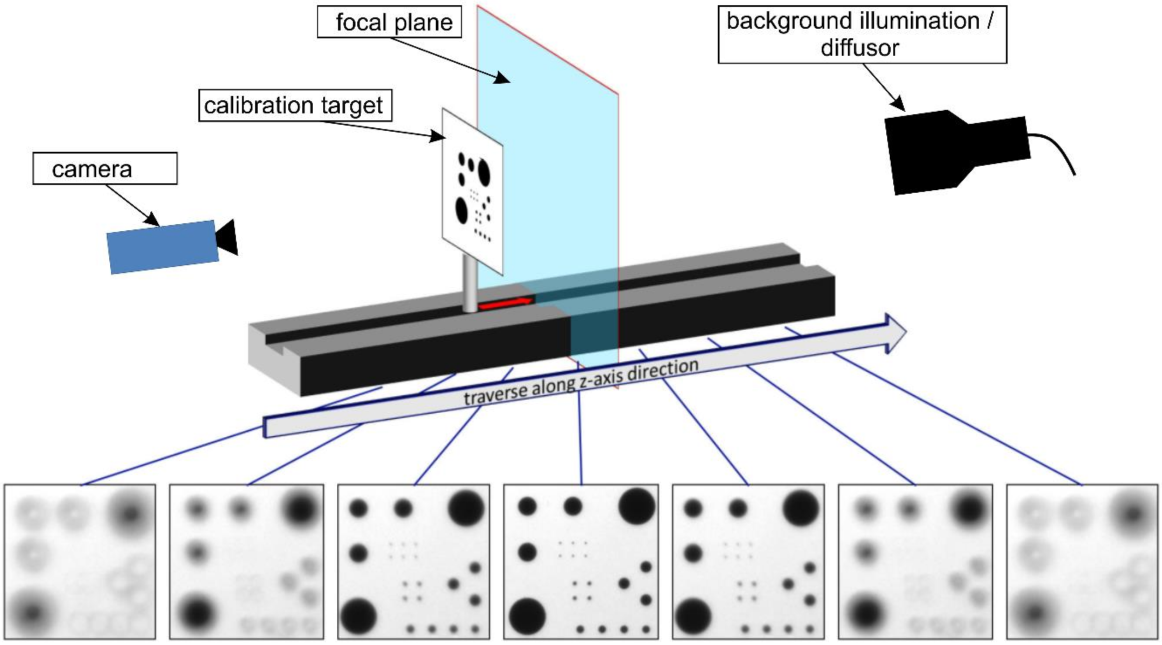
focal plane
background illumination / diffusor
calibration target
camera
traverse along z-axis direction

Fig. 3 Principal procedure of a shadowgraphy's depth-of-field-calibration (adapted from [56])

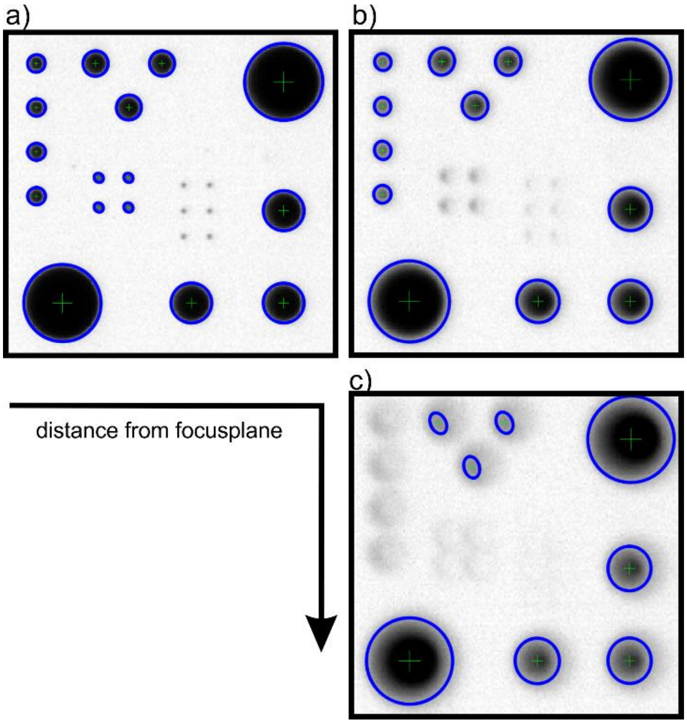
a)
b)
c)
distance from focusplane

Fig. 4 Calibration dots analysed with LaVision Particlemaster – Shadowgraphy: a) z = 0.0 mm, b) z = -1.0 mm, c) z = -2.0 mm

There is no general rule how to distinguish between focussed and unfocussed particles. Several approaches for defining an 'in-focus-criteria' are presented in literature. Two indicators are commonly used for defining particles to be in-focus: the gray-level gradient at the detected particle boundaries [40, 57-60] and the particle contrast [48, 61], or both [45, 47, 55]. A recent approach has considered the particle shadow area of two differently focused cameras [43]. It can be distinguished between studies, in which unfocussed particles were neglected in further evaluation [47], and studies, in which the detected size of unfocussed particle shadows was corrected in a second step [35, 40, 48, 60-62].

In shadowgraphy, the DOF depends on the particle size [44]: Generally, the smaller the particle, the smaller the DOF. This effect biases the detected particle size distribution towards larger particles and leads to erroneous G_p and particle concentrations. Depending on the in-focus-criteria and the elimination of unfocussed particles, the DOF is additionally affected. When determining particle concentrations or particle mass flow rates, the varying DOF has to be considered (see **eq. (5-4)**). Most of the studies assumed a linear relation between particle size and DOF [39, 40, 42, 43, 48, 51, 55, 60, 63], others assumed a linear relation with two different slopes [35, 45], a power-law dependence [47] or another functional dependence [62]. A constant DOF for every particle size was used in e.g. [38, 46, 49, 50, 57, 59]. An overview of several shadowgraphy studies and their important investigation parameters is given in **Table A 2** in the **Appendix**.

A commercial code for particle shadow detection and analysis is included in DaVis by LaVision Gmbh and is called ‘ParticleMaster’. As explained in more detail in **section 5.2.5.1**, this software was used for basic particle detection in the following analyses. The ‘ParticleMaster’ code was compared to an in-house developed code of the Institute of Thermal Turbomachinery, University of Karlsruhe. The comparison showed a good agreement of detected particles, if the different minimum detectable shadow size was considered [64].

It must be noted, that shadowgraphy measures a shadow area and hence, only a two-dimensional projection of particles. Based on the measured shadow area, an area-equivalent diameter is defined which is the diameter of a circle with the same shadow area. In all following analyses, this area-equivalent diameter is considered for size classification. Furthermore, it is assumed that all particles are spherical.

3.3. Particle Image Velocimetry (PIV)

Another considered measurement technique for investigating flow structures and particle characteristics is Particle Image Velocimetry (PIV). It is a common measurement technique for measuring quantitative velocity fields, mostly in a two-dimensional plane. A flow of interest is seeded with tiny particles, so-called tracers. These tracers are assumed to follow the flow instantaneously. The tracers have the purpose to visualize the flow due to their light reflection behaviour. A pulsed light source is used to illuminate the tracers within a flow, while a camera is recording the tracers. Two short-time light pulses are required to achieve two recordings of the tracers. By measuring the tracer’s displacement and by knowing the time separation between those two pulses, the velocity of the tracer and hence, the velocity of the flow can be calculated. The general setup of PIV is sketched in **Fig. 5**.

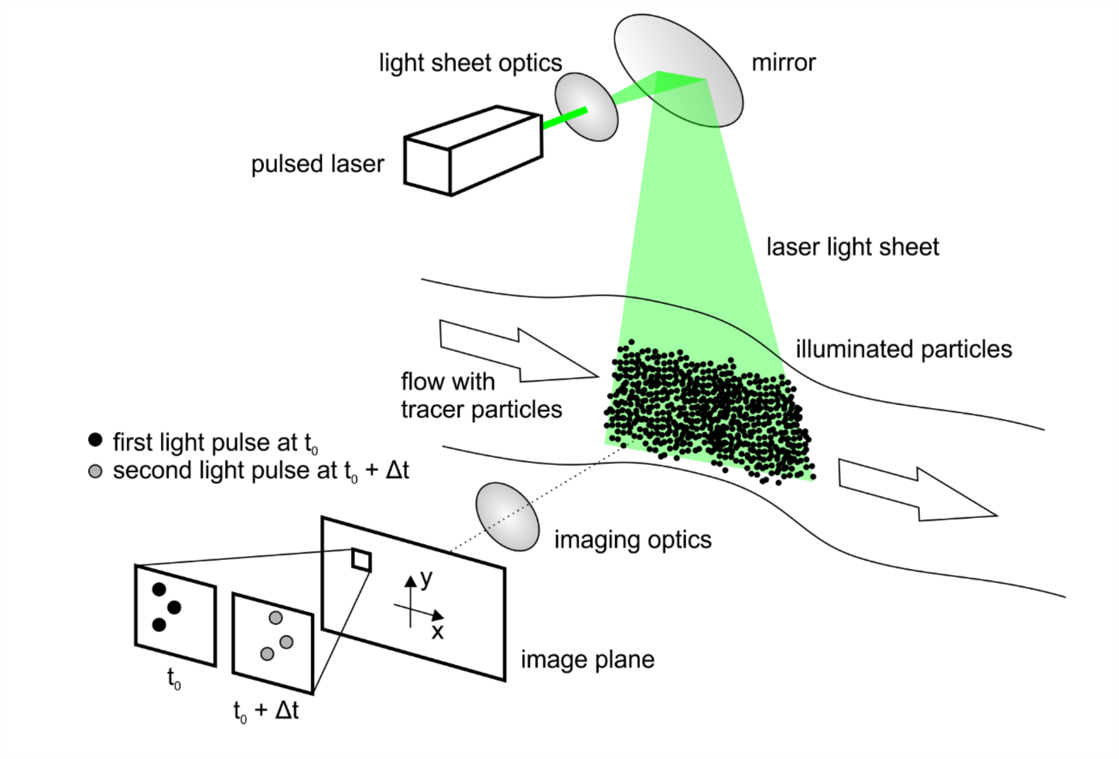
light sheet optics
mirror
pulsed laser
laser light sheet
illuminated particles
flow with
tracer particles
● first light pulse at t_0
○ second light pulse at $t_0 + \Delta t$
imaging optics
y
x
image plane
t_0
$t_0 + \Delta t$

Fig. 5 General setup and principle of PIV (adapted from [65])

There are two basic approaches for displacement detection: auto-correlation and cross-correlation. While in auto-correlation two light pulses are recorded into one image, each pulse is recorded on a separate image for cross-correlation. For both approaches the images are separated into areas, so-called interrogation windows. The interrogation windows can contain multiple tracers. The correlations are based on the intensity distribution of the interrogation windows. Cross-correlation is searching for the displacement with the highest probability between an interrogation window in the first image and the respective interrogation window in the second image. The most probable displacement is also called 'peak'. For each interrogation window one displacement and hence, one velocity vector is calculated. The principal procedure of PIV with cross-correlation is illustrated in **Fig. 6**. More detailed information regarding PIV can be found in e.g. [65].

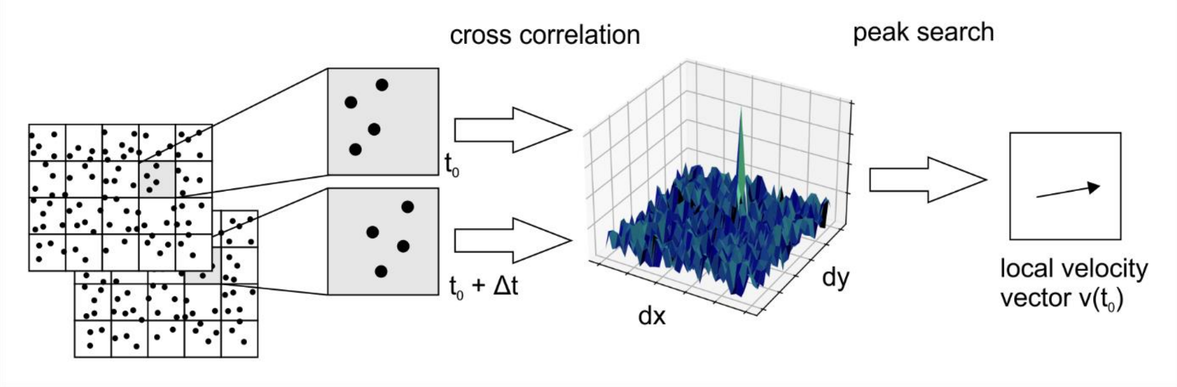
cross correlation
peak search
t_0
$t_0 + \Delta t$
dx
dy
local velocity
vector $v(t_0)$

Fig. 6 Principal procedure of the PIV technique (cross-correlation) (adapted from [66])

3.3.1. PTV from PIV correlation

Particle Tracking Velocimetry (PTV) from PIV correlation is an advanced analysis technique which is implemented in LaVision DaVis FlowMaster software. This procedure requires an initial particle displacement measurement made with PIV. The interrogation window size is iteratively refined until only one single particle is located in it. The accurate position of each particle is defined to be the position of the intensity maximum. With the help of the initial PIV results, the single particle displacement is determined with cross-correlation. This method allows determining individual particle velocity, while the standard PIV method measures a mean velocity vector of an interrogation window which can contain multiple particles. PTV from PIV correlation is not identical to the standard Particle Tracking Velocimetry method of detection and tracking [66].

3.4. Test Facility GBK

All following experiments were conducted in the multi-phase flow facility (‘Gemischbildungskanal’, GBK). This facility is a small test facility integrated into DLR’s supersonic wind tunnel infrastructure in Cologne, Germany [67]. It is a fully automated blow down facility, using dried high-pressurized air from reservoir tanks. A sketch of the principal GBK facility is illustrated in **Fig. 7**. Due to its small size, the GBK facility can run several days until the reservoir tanks have to be refilled. As a consequence, the GBK can achieve steady state flow conditions.

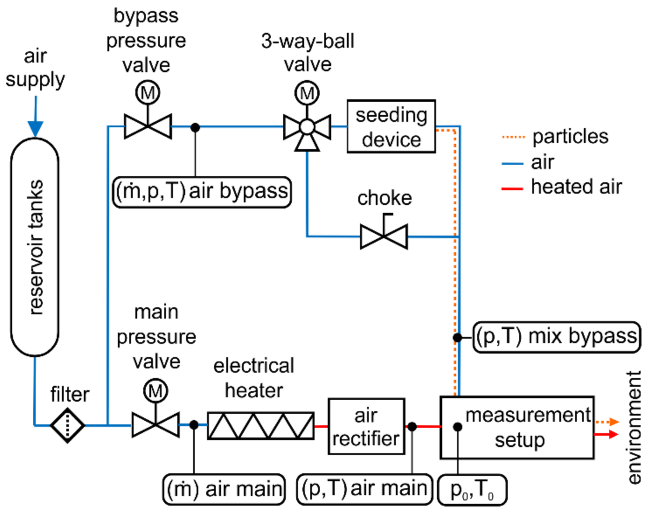
bypass pressure valve
air supply
3-way-ball valve
M
seeding device
particles
air
heated air
(ṁ,p,T) air bypass
choke
reservoir tanks
main pressure valve
(p,T) mix bypass
electrical heater
filter
air rectifier
measurement setup
environment
(ṁ) air main
(p,T) air main
p_0,T_0

Fig. 7 Sketch of the GBK facility

Variable measurement setups can be fed with two air flows: a heatable pure air flow, named ‘main’ flow, and an unheated flow, named ‘bypass’ flow in the following. An electrical heater with a maximum electrical power of 191 kW can heat the main air flow up to 800 K. Afterwards, an air rectifier reduces the main flow turbulence. The bypass flow is equipped with an in-house developed seeding device for particle dispersion. It can be either controlled by a three-way-ball valve, or by a customized mechanical device. The seeding device has an air volume of approximately 0.011 m^3. If a three-way-ball valve is used for seeding device control, air is directed through a seeding device’s bypass unless seeding is started. The pressure drop of the seeding device's bypass is adapted by a manual choke to the pressure drop of the seeding device.

GBK's maximum design air pressure is 5.4 MPa, the maximum total air flow rate (main + bypass) is approximately 1.5 kg/s and the maximum bypass air flow rate $\dot{m}_{by}$ is limited to 0.2 kg/s. A minimum cross section $A_{GBK\ crit}$ of 25 x 40 mm² is limiting the main flow. All limiting aspects of the general GBK facility without any measurement setup are summarized in **Table 3**. Several measuring points exist to fully determine the GBK flow. The stagnation pressure (p_0) and stagnation temperature (T_0) were measured within the measurement setup.

Table 3 General limitations of the GBK facility without measurement setup

parameter	unit	range	remarks
p_0	MPa	up to 5.4	max. GBK design pressure
T_0	K	up to 800	max. GBK design temperature
heater power P_{heater}	kW	up to 191	max. electrical heater power
air mass flow $\dot{m}_{main} + \dot{m}_{by}$	kg/s	up to 1.5	limited by safety ball valve
bypass air mass flow $\dot{m}_{by}$	kg/s	0.2	limited by bypass pipe diameters
nozzle throat cross section A*	m²	0.001	$A_{GBKcrit}$ = 25 x 40 mm²

3.4.1. GBK Measurement Setup

This section describes the general measurement setup. Differences to this setup are described in the respective test setup section of the following analyses.

The GBK measurement setup is connected to the GBK facility and can be designed and set up variably. To establish high-accuracy individual particle characterization methods, a new measurement setup was designed. The measurement setup contained a cross section adapter, a mixing chamber, an ideal-contoured nozzle, a test chamber, and a diffusor pipe. A sketch of the implemented measurement setup is given in **Fig. 8**.

The measurement setup mixing chamber is made of standardized (DIN EN 1092-1) pipe sections of type DN65 and PN40. Hence, the mixing chamber had an inner diameter of 70.3 mm. The maximum stagnation pressure p_0 of standardized pipe sections of type DN65 and PN40 depends on the stagnation temperature T_0, see **Fig. 9**. The illustrated maximum p_0 and T_0 values are only valid for the measurement setup, and not for the general GBK facility. The maximum stagnation temperature is limited by the limiting temperature of the mixing chamber sealing material PTFE, which is 573 K. To avoid long time damaging of the sealing, the maximum stagnation temperature is set to 551 K. Since both p_0 and T_0 of the measurement setup are lower than p_0 and T_0 of the general GBK facility, the measurement setup limits the maximum operation range.

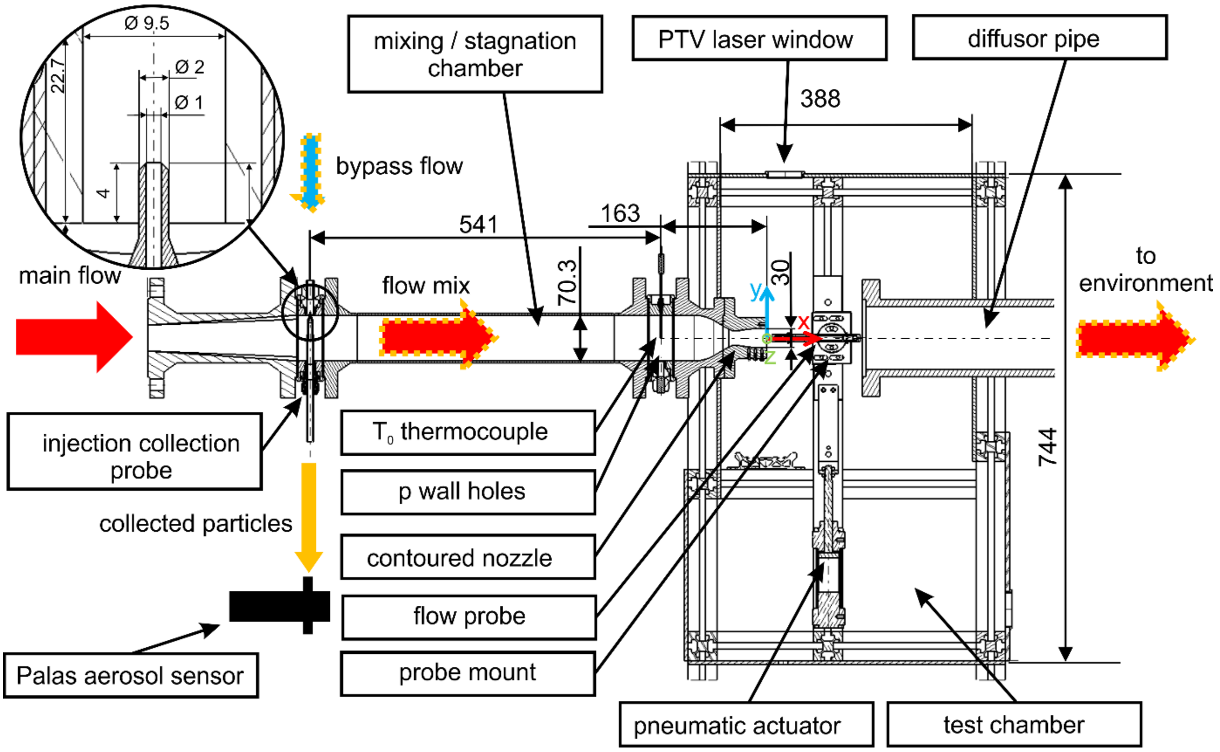
Ø 9,5
Ø 2
Ø 1
22.7
4
main flow
bypass flow
mixing / stagnation chamber
PTV laser window
diffusor pipe
388
541
163
flow mix
70.3
30
y
x
z
to environment
744
injection collection probe
T_0 thermocouple
p wall holes
contoured nozzle
flow probe
probe mount
collected particles
Palas aerosol sensor
pneumatic actuator
test chamber

Fig. 8 Sectional side view of the GBK measurement setup

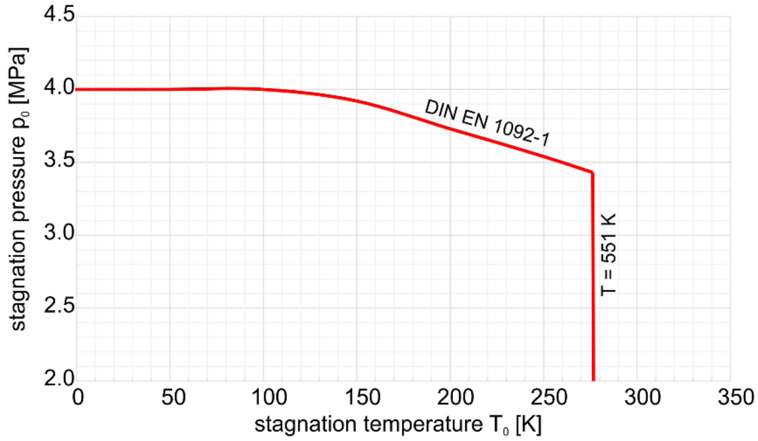

Fig. 9 The maximum stagnation pressure p_0 depends on the stagnation temperature T_0, following DIN EN 1092-1

The heatable main flow was mixed with the cold two-phase bypass flow in front of the mixing chamber. A circular conical particle injection collection probe was located at the position where the cold particle bypass flow was injected into the heated pure air flow, for additional particle mass flow calibration purposes. Geometric details of the particle injection and the particle injection collection probe tip can be found in **Fig. 10**. Its position was optimized in terms of minimizing gravity-based particle losses in pipes or pipe bending losses [68]. Either a closed container or an additional aerosol spectrometer was mounted at the outlet of the injection collection probe. It was assumed that particles were caught with the closed container due to the particle inertia.

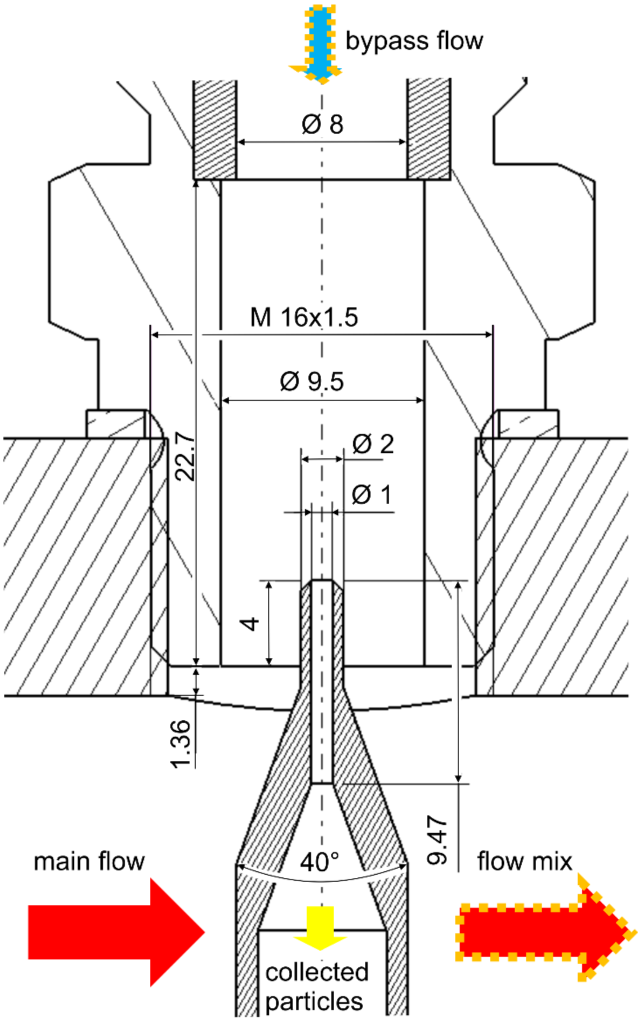

Fig. 10 Geometric details of the particle injection

In selected tests, a Palas aerosol spectrometer was installed. Due to its time-resolved measurement ability, the aerosol spectrometer was used to check the absence of particle seeding during the facility's heat-up and shut-down phase. Particle seeding during these phases was identified to be a significant error source in total particle mass determination [15].

Sensors of types welas 2070 HP or 2300 HP were installed and connected to a Palas Promo 3000 HP. The maximum particle concentration for both sensors was $1*10^6$ particles/cm³ and $4*10^4$ particles/cm³, respectively. Considering the spectrometer's maximum design pressure of 1 MPa and its maximum design temperature of 393 K, it was only installed for tests with lower stagnation pressures p_0 and flow stagnation temperatures T_0. A constant air volume flow of 5 l/min was required for accurate particle size determination, which was controlled by the spectrometer. The internal velocity calibration of the spectrometer was performed, while the flow of the facility was running. Special calibration particles, provided by Palas, were used for size calibration. It is assumed that the choice of spectrometer and closed container at the injection collection probe did not affect the nozzle flow. This can be reasoned by negligible aerosol and closed container air flow rates, compared to the air mass flow.

Particles were collected with the injection collection probe to check if particle total mass flow can be predicted only with the collected particle mass, while the aerosol spectrometer was used to check the absence of particle seeding beyond the measurement time.

The Mach number within the mixing chamber was derived from the nozzle geometry, respectively the expansion ratio. It was assumed that the Mach number within the mixing chamber was subsonic. The derived mixing chamber Mach number was 0.0575. A 1.1 mm diameter type K thermocouple close to the nozzle was used for temperature measurements. It was assumed that the measured static temperature can be used as T_0 signal. This can be reasoned by negligible differences between static and total temperature smaller than 0.5 K, considering isentropic relations and the low mixing chamber Mach number. This difference is smaller than the 1.1 K minimum standard measurement error of type K thermocouples. To avoid particle deposit in a Pitot tube, p_0 was reconstructed by means of the wall pressure close to the T_0 sensor, the mixing chamber Mach number, and isentropic relations. Here, it was assumed that the wall pressure is identical to the static pressure. The reconstructed p_0 value agreed well to the stagnation pressure measurements upstream of the cross-section adapter.

For heating augmentation tests, it was tried to achieve large nozzle exit diameters d_e and large nozzle Mach numbers. Maximizing both is a trade-off, due to all limitations of the GBK facility and of the measurement setup (see **Fig. 9** and **Table 3**). The maximum achievable nozzle exit diameter d_e is a function of the selected Mach number, shown in **Fig. 11**. While the minimum throat cross section $A_{\text{GBK crit}}$ is limiting the nozzle exit cross section at low Mach numbers, the maximum Mach number is limited by the lowest possible test chamber pressure p_a, the maximum stagnation pressure and maximum stagnation temperature, which again is interdependent (see **Fig. 9**). It was initially assumed that the test chamber pressure p_a is always around 0.11 MPa. All possible Ma/d_e relations are shaded red in **Fig. 9**. The final nozzle had a length of 111.9 mm, a nozzle exit diameter of 30 mm and a design Mach number of 2.1. Its ideal-contoured geometry was calculated by means of an in-house developed methods of characteristics design tool. This nozzle configuration is marked as a black cross in in **Fig. 11**. The complete nozzle contour can be found in **Fig. 45** in **section 5.3.1**.

The nozzle ended in a test chamber with dimensions of 388 mm x 390 mm x 744 mm. The test chamber pressure p_a was measured with multiple pressure sensors in the test chamber. This chamber had a convex shape in the y-z-plane, allowing optical access in 10° inclination steps to ensure window related reduced aberration (see **Fig. 16**). Additional windows provided optical access from all sides. The distance between GBK diffusor pipe and nozzle exit plane was 147 mm.

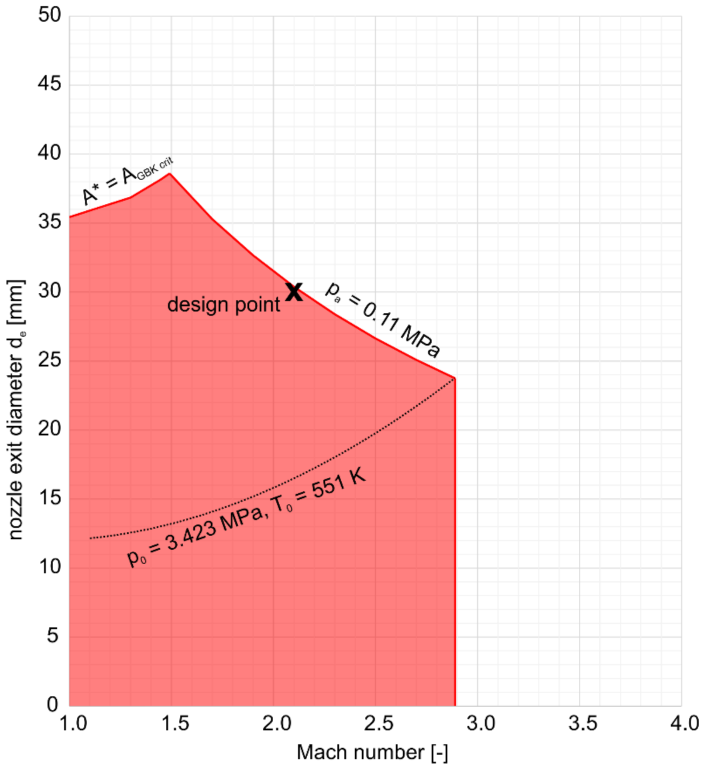

Fig. 11 The maximum achievable nozzle exit diameter depends on the chosen Mach number and is limited by the lowest achievable test chamber pressure p_a, the maximum stagnation pressure p_0 and stagnation temperature T_0, as well as by the minimum cross section $A_{GBK\ crit}$ of the GBK facility

3.4.1. Probe Installation

The measurement setup was designed to investigate particle-probe interactions and heating augmentation effects. A fast-pneumatic probe insertion system was implemented. A sketch of the probe insertion system is given in **Fig. 12**.

The probe consisted of a probe head, a coaxial thermocouple, an insulator, a head mount, and a probe mount. The probe mount was aligned in horizontal direction and was attached at its lateral ends to two vertical rail carriages. These were connected via connectors to a pneumatic actuator mount, at which the pneumatic actuator was connected. The pneumatic actuator created a force in vertical direction along the rails, so that the probe was inserted into the flow from the bottom up. The full insertion of the probe into the flow took around 75 ms. The orientation and the position of the probe was adjusted with respective rotation and translation adjustment devices. Due to the long connectors between the pneumatic actuator mount and the rail carriages a high freedom degree of illumination was achieved. The probe position was determined with a Laser-based distance sensor. The cables of the coaxial thermocouple were covered from the flow by means of a cable housing.

The probe head and the insulator were clamped into the head mount with clamping screws. Alignment edges were used for accurate re-positioning of the probe head. The head mount was axisymmetric (cylindrical) and the probe head was hemispherical with a probe nose diameter d_{Probe} of 12 mm. The probe head was made of stainless steel, namely 1.4539. The probe length, from probe head to probe mount, were 60 mm. The distance between probe tip and nozzle exit has varied between 4 to 6 mm, which is caused by thermal expansion of the nozzle.

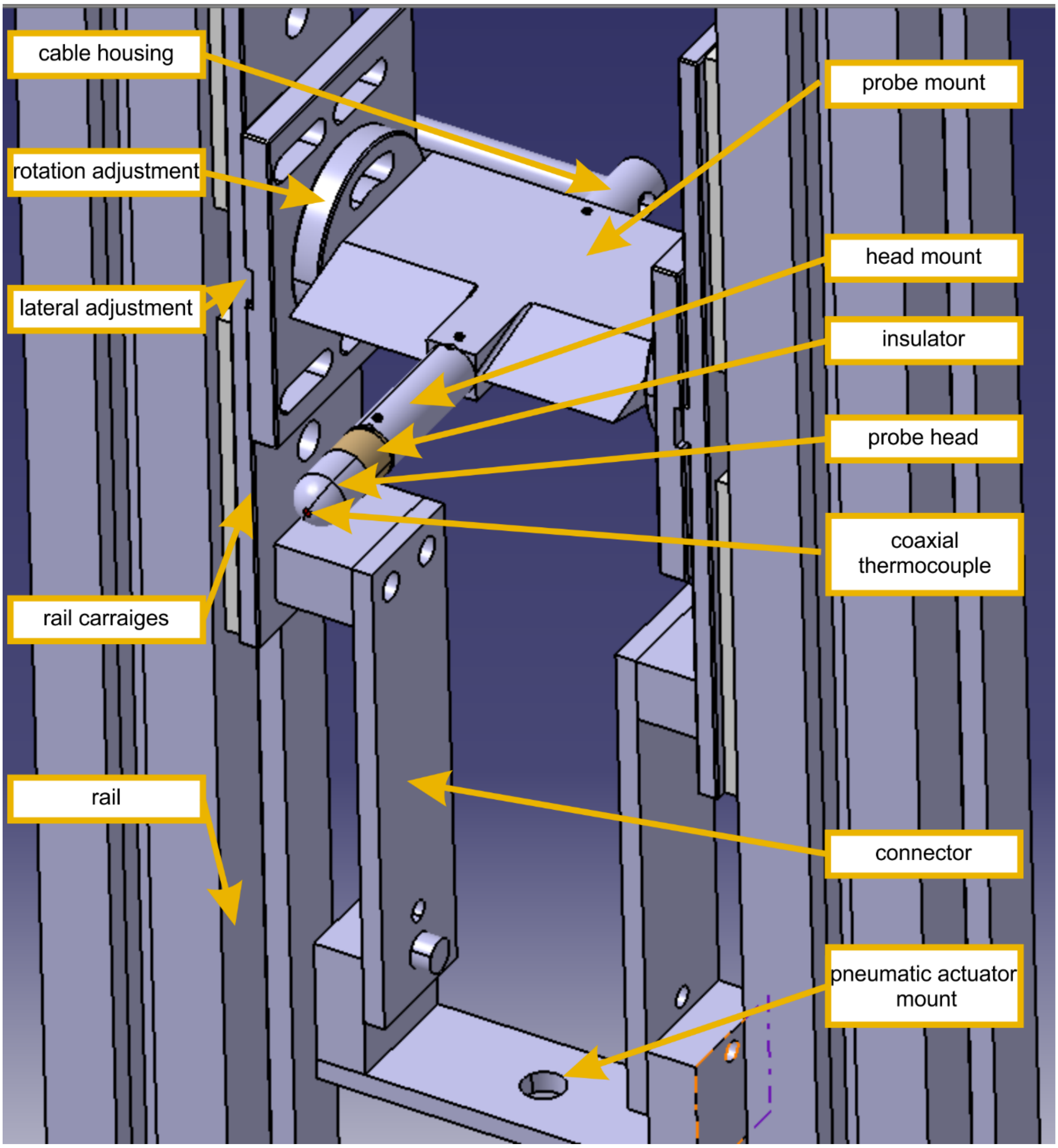
cable housing
rotation adjustment
lateral adjustment
rail carraiges
rail
probe mount
head mount
insulator
probe head
coaxial thermocouple
connector
pneumatic actuator mount

Fig. 12 Sketch of the probe setup. Nozzle, diffusor and particle chamber are not shown

The stagnation heat flux was derived with the help of a Type-E coaxial thermocouple. This thermocouple was manufactured by the Supersonic and Hypersonic Flow Technologies Department of DLR. It had a thread-less 1.9 mm diameter tip and a M2.5 thread for mounting. Its total length was 18 mm. The coaxial thermocouple was fixed with a nut. The probe head was insulated to decrease the coaxial thermocouple signal noise. The coaxial-thermocouple installation is sketched in **Fig. 13**. The probe head as well as the coaxial thermocouple were polished with a 2000-grit sandpaper before each test run, which was done to activate the thermocouple.

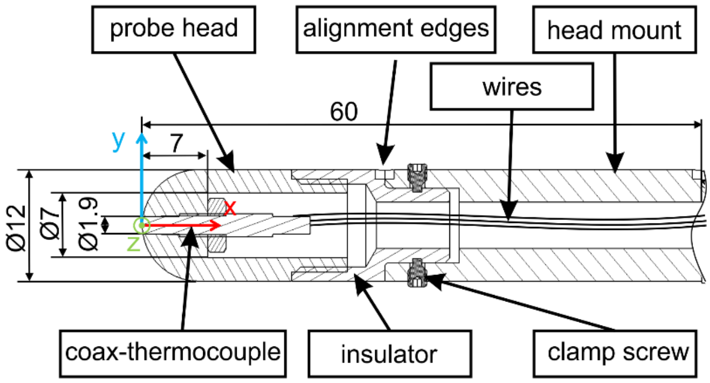

Fig. 13 Sketch of probe setup, dimensions given in mm

3.4.2. Operation Range

The pressure in the test chamber p_a depends on the stagnation pressure and the probe position, considering the presented GBK measurement setup design and the Ma = 2.1 nozzle. The test chamber was not perfectly sealed. The supersonic nozzle flow draws test chamber air into the diffusor. The higher the stagnation pressure, the higher the nozzle flow impulse, the higher the air draw and as a consequence, the lower the test chamber pressure. When the probe is positioned within the flow, the nozzle flow is partially blocked, which is caused by a comparative large probe or by a comparative small diffusor diameter. As a result, the test chamber air draw is reduced and the test chamber pressure increases. The relation between p_a, p_0 and probe position is shown in **Fig. 14**. Generally, the flow between the nozzle exit and up to approximately 5 mm downstream was investigated. It was predefined that tests can be successfully conducted as long as the entire investigated nozzle flow was supersonic and no vertical overexpansion shock within the investigated area was detected. Due to the pressure relations shown in **Fig. 14**, a minimum stagnation pressure of approximately 0.45 MPa was required for the absence of the overexpansion shock within the first 5 mm of the Ma = 2.1 nozzle flow. The resulting operation range of the GBK facility and the presented measurement setup considering the Ma = 2.1 nozzle is illustrated in **Fig. 15**. The red lines indicate the operation limits, while the black dashed lines are auxiliary lines. The maximum power of the electrical heater and the maximum total air flow are limited by the general GBK test facility. The GBK measurement setup sealings are designed for a maximum temperature of 573 K. The lowest total temperature of the flow is limited by the gas temperature in the reservoir tanks and the piping system temperature between reservoir tanks and the GBK measurement setup. Furthermore, varying ratios between reservoir tank pressure and desired total pressure affect gas expansion cooling effects. As a first guess, it was assumed that the lowest achievable total temperature is 273 K. As described above, a minimum stagnation pressure of 0.45 MPa was required to avoid vertical overexpansion shocks in the first 5 mm of the nozzle exit flow.

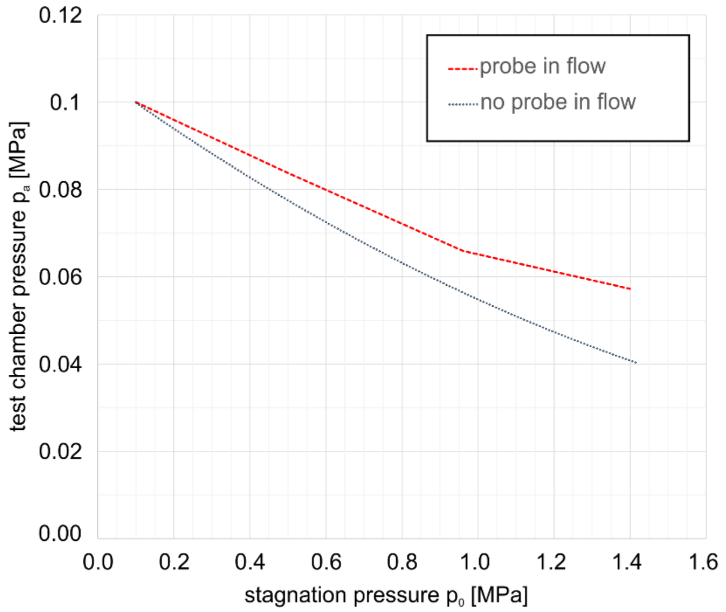

Fig. 14 Relation between p_0, p_a, and probe position for the presented GBK facility and measurement setup

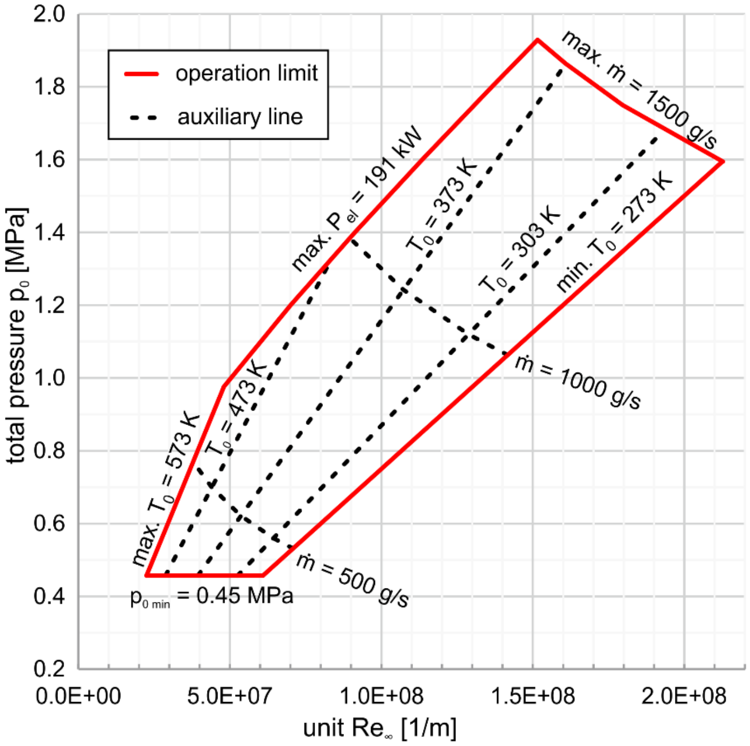

Fig. 15 Operation range of GBK facility at Ma = 2.1

3.5. General Optical Measurement Setup

In general, two optical systems were set up und used in all of the following analyses. This section describes their general setup. Specific settings are reported in the respective subsections.
The two optical systems were a high-resolution system and a low-resolution system. An overview of the optical setup is sketched in **Fig. 16**, while a photograph of the camera setup is given in **Fig. 17**.

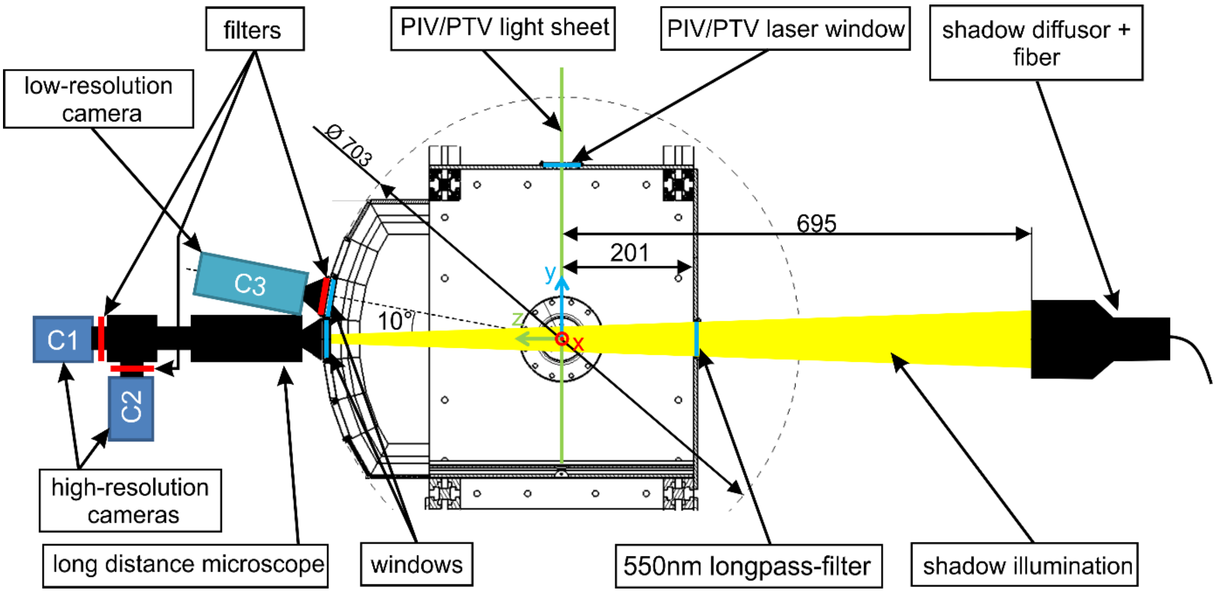
filters
PIV/PTV light sheet
PIV/PTV laser window
shadow diffusor + fiber
low-resolution camera
Ø 703
695
201
y
z
x
C3
10°
C1
C2
high-resolution cameras
long distance microscope
windows
550nm longpass-filter
shadow illumination

Fig. 16 Front view on the PTV and shadowgraphy setup, dimensions given in mm

The high-resolution system was mainly used for shadowgraphy and additionally for only some initial PIV and PTV tests. It consisted of two LaVision Imager sCMOS cameras (named C1 and C2), having a pixel size of 6.5 µm. A long-distance microscope K2 Distamax of Infinity Photo-Optical Company was equipped with a CF-1b lens, a 'Zoom Module'. Both cameras were linked to the long-distance microscope via an optical beam splitter.
The low-resolution camera (named C3 in the following) was a PCO 1600 with a Nikon Nikkor tele lens. It was used for PIV / PTV applications only. Its pixel size was 7.4 µm. A Scheimpflug adapter was used to compensate the angle of 10° between vertical focus plane and camera axis. Distancing rings were used for shorten the required focal length. The working distance between lens and focus plane was similar to those of the shadowgraphy system, which was 351 mm. Bandpass or low-pass filter were placed in front of the high-resolution and low-resolution cameras, depending on the application.

The illumination source was a 'SpitLight DPSS 250 PIV' laser system of InnoLas Laser GmbH, generating two light pulses with a nominal time separation (Δt) of 400 ns at a repetition rate of 100 Hz and a wavelength of 532 nm. The 532 nm laser light was used for the PTV measurements and for feeding the shadow diffusor of Dantec Dynamics GmbH. The shadow diffusor generated a background illumination with a wavelength range of 532 nm to approximately 564 nm. Several wavelength filters were used to separate PTV and shadowgraphy measurements properly. Only light in the wavelength range of 550 nm to approximately 564 nm was used for shadowgraphy measurements by implementing 550 nm long-pass filters behind the shadow diffusor and in front of the shadowgraphy cameras. The 532 nm laser light is marked green and the shadowgraphy background illumination is marked yellow in **Fig. 16**. The energy for shadowgraphy and PTV illumination was adjusted with a set of half-wave plates (λ/2) and beam splitters (BS). An additional photodiode was connected to an oscilloscope and was used to control and to correct the pulse time separation Δt. The timing of laser and cameras as well as the camera data acquisition was controlled by a PTU-X timing unit of LaVision and the LaVision DaVis ParticleMaster software V10.1. The maximum illumination area of the shadow diffusor was 112 mm in diameter. The shadow diffusor was placed 695 mm away from the nozzle axis. A maximum pulse energy of 30 mJ was used to feed the shadow diffusor.

The PTV light beam was generated by one cylindrical lens with focal length of 500 mm. This lens was placed ahead of the test chamber in order to direct the PTV illumination vertically from top to bottom. The PTV light sheet was around 5 mm wide in x-direction and parallel to achieve homogenous illumination intensities across the nozzle. A photograph of the laser optics is given in **Fig. 18**.

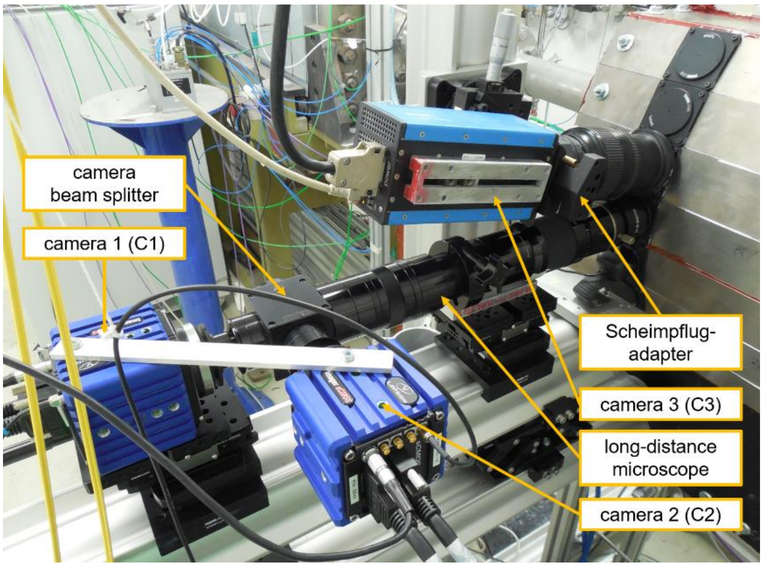

Fig. 17 Photograph of the general camera setup

All data of the GBK test facility and the flow probe were recorded by data acquisition system components of National Instruments (DAQ). The GBK test facility data were recorded with 10 Hz. The flow probe data, especially its position and its coaxial thermocouple signal, were recorded with 50000 Hz. A main control computer controlled all implemented devices. A sketch of the complete scientific setup for all following analyses is given in **Fig. 19**.

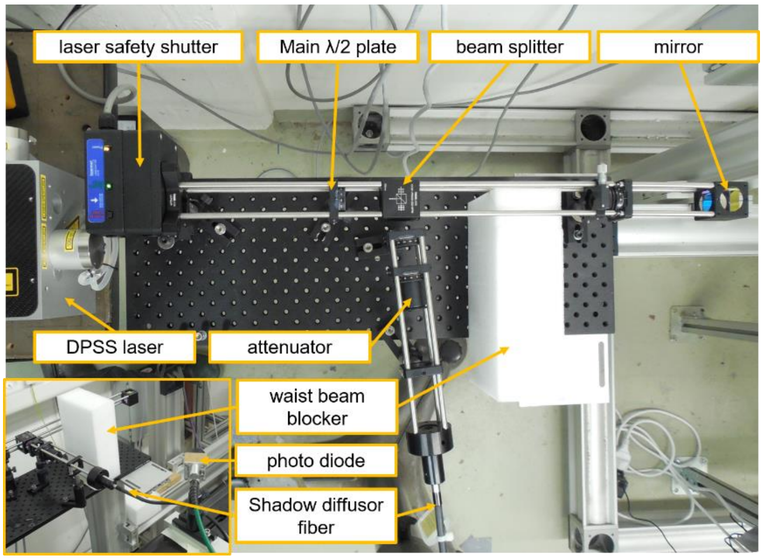
laser safety shutter
Main λ/2 plate
beam splitter
mirror
DPSS laser
attenuator
waist beam blocker
photo diode
Shadow diffusor fiber

Fig. 18 Photograph of the laser optics

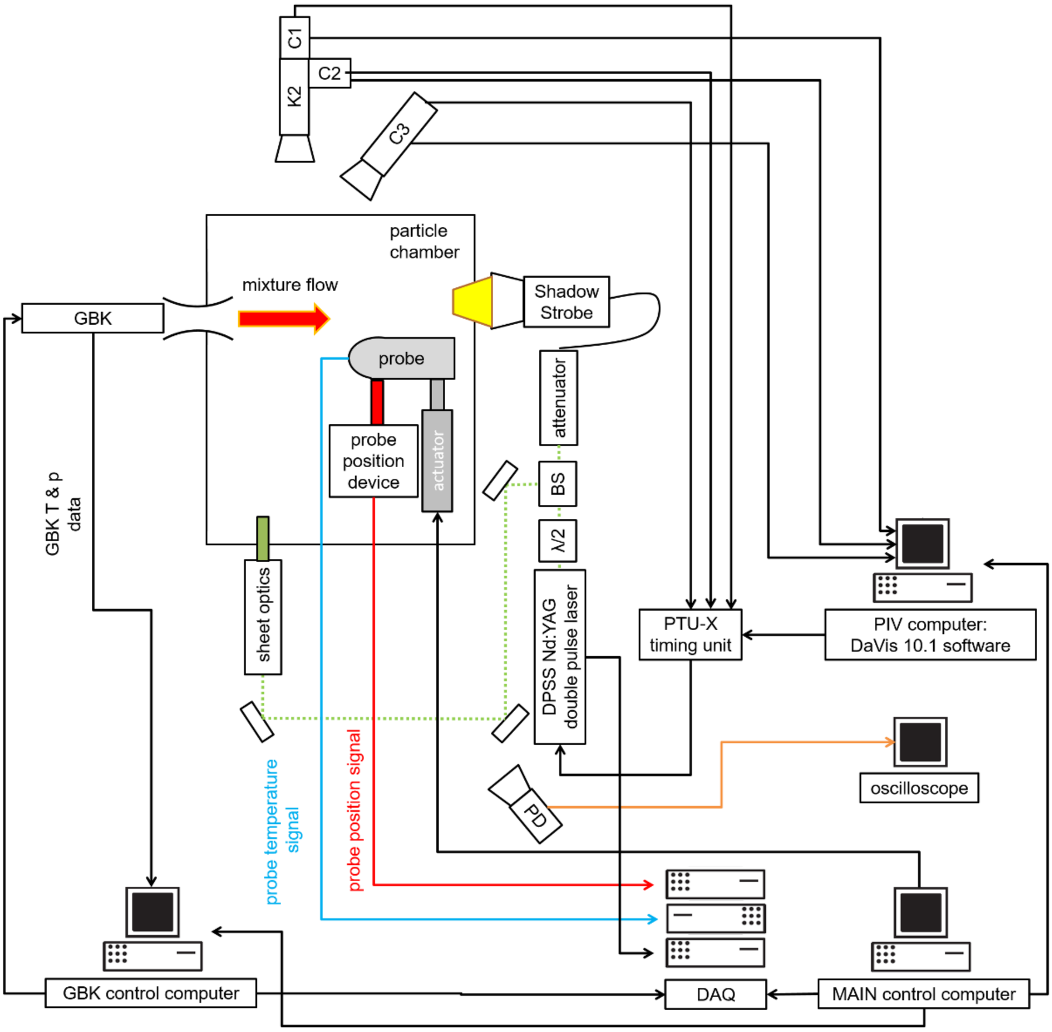
C1
K2
C2
C3
particle chamber
mixture flow
GBK
Shadow Strobe
probe
attenuator
probe position device
actuator
BS
λ/2
GBK T & p data
sheet optics
DPSS Nd:YAG double pulse laser
PTU-X timing unit
PIV computer: DaVis 10.1 software
probe temperature signal
probe position signal
oscilloscope
PD
GBK control computer
DAQ
MAIN control computer

Fig. 19 Sketch of the complete scientific setup for all following analyses

3.6. Particles

Four different particle materials were used for seeding in the examinations. The finest available material made of MgO was chosen for PIV application and velocity uncertainty estimation purposes (particle size distributions are shown in **Fig. 20** to **Fig. 25**). This particle material is called 'PIV-MgO' in the following. For particle mass flow rate determination, three different particle materials were used for seeding, namely alumina (Al_2O_3), magnesium oxide (MgO) and silica (SiO_2). The selected Al_2O_3 and MgO particles offered a significant number of particles larger than 10 µm, which was required for particle analysis with shadowgraphy. The MgO material was taken from Lehmann&Voss GmbH and was additionally sieved to decrease the number of particles smaller than 10 µm, so that the relative number of particles larger than 10 µm increased. SiO_2 was chosen not only because of its significant lower density, but also because of its relevance for Martian atmosphere simulation.

Particle size distributions of Al_2O_3 and both MgO particle materials were externally analysed by Microtrac GmbH. These data were achieved with a dynamic image analysis device 'PartAn SI' and a 'S3500' laser diffraction device. For these measurements, all materials were diluted into water to reduce agglomeration effects. Additionally, large MgO particle measurements were also conducted in air, resulting in particle size distributions very similar to those measured in wet dilutions.

No reference size data from Microtrac are available for the SiO_2 particles. This is caused by the fact, that the company cancelled their supply in analysing customer's particles during preparation of this work. SiO_2 data from the supplier's technical datasheet are given instead.

Particle size distributions are shown generally as histograms, grouped by particle size. These histograms are called 'differential'. If size distributions are cumulated up to a specific size, they are called 'cumulative'. There are two common weightings of these histograms: particle number-weighted or particle volume-weighted. While in particle number-weighted histograms, the bar height represents the number of all particles with the corresponding size, the bar height indicated the particle volume of all particles with the corresponding size in volume-weighted histograms. These size distributions are called 'number distribution' or 'volume distribution' in the following and indicated with 'count' or 'volume', respectively. It must be noted, that number-weighted distributions highlight small particle sizes, while volume-weighted distributions highlight large particle sizes. As an example, a 20 µm particle has a $1*10^6$ times larger volume than a 0.2 µm particle. Assuming that 10000 0.2 µm particles and a single 20 µm particle were detected, the single 20 µm particle represents less than 0.01 % of the total particle number, while it provides 99 % of the total particle volume. As a result, the single 20 µm particle becomes 'invisible' in a particle number-weighted differential histogram, while the 10000 0.2 µm particles become 'invisible' in a particle volume-weighted differential histogram.

Number and volume distributions of Al_2O_3 and both MgO particle materials are illustrated in **Fig. 20** to **Fig. 25**. The green lines represent the cumulative particle distributions up to a specific particle size, which is given on the x-axis. As an example, approximately 60 % of the entire Al_2O_3 particle volume is spread on particles < 30 µm (see **Fig. 23**). The red bins are the particle distribution histogram and represent the gradient of the green line. To get a probability density function, the particle number distribution histogram of **Fig. 20**, **Fig. 22**, and **Fig. 24** can be used. The results of the dynamic image analysis are referenced in **Fig. 22** to **Fig. 25**, while laser diffraction results are used describing PIV-MgO material in **Fig. 20** and **Fig. 21**. This is caused by the fact that the dynamic image analysis detects only particles larger than 2 µm which will ignore most of the PIV-MgO particles.

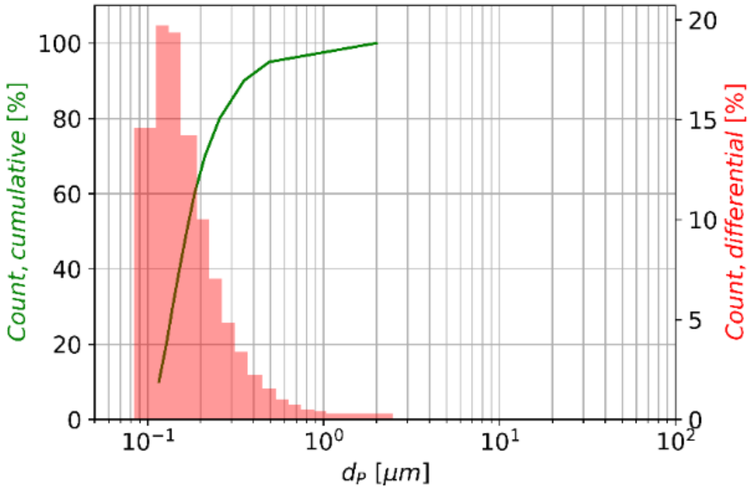

Fig. 20 Cumulative and differential particle number distribution of PIV-MgO particles, measured with a 'S3500' by Microtrac Gmbh

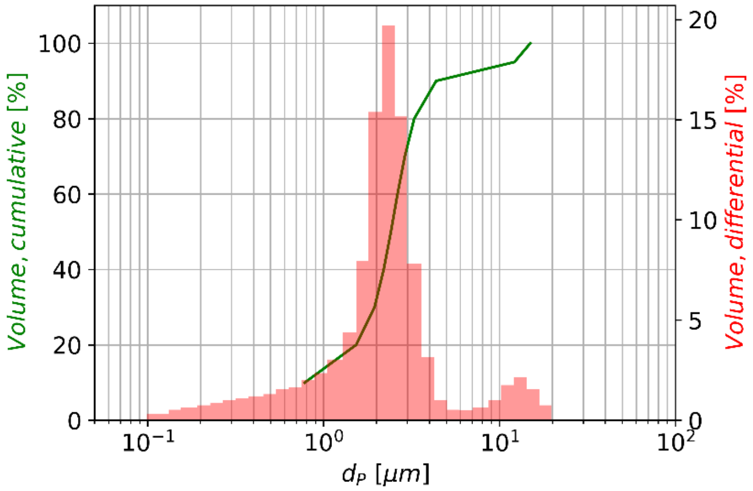

Fig. 21 Cumulative and differential particle volume distribution of PIV-MgO particles, measured with a 'S3500' by Microtrac Gmbh

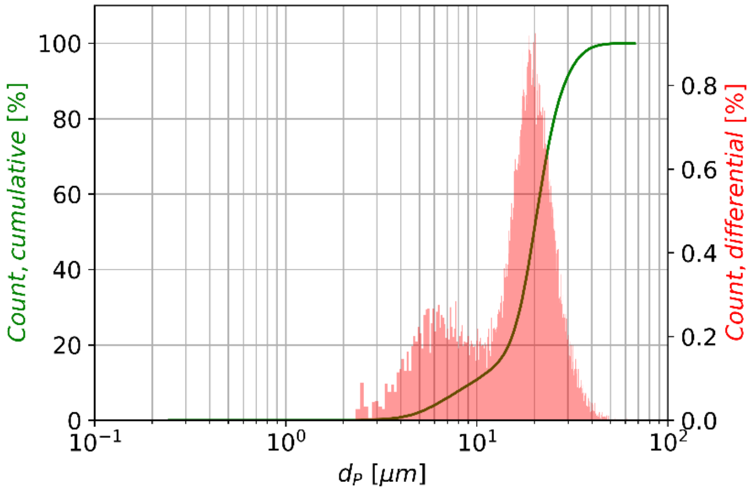

Fig. 22 Cumulative and differential particle number distribution of Al_2O_3 particles, measured with a 'PartAn SI' by Microtrac Gmbh

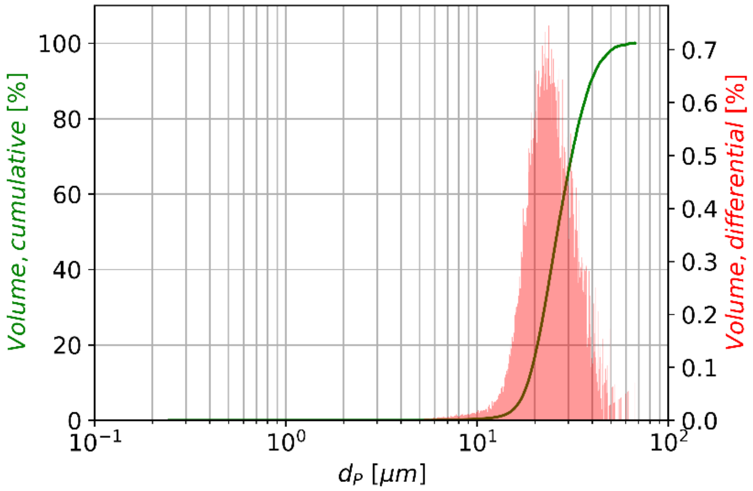

Fig. 23 Cumulative and differential particle volume distribution of Al_2O_3 particles measured with a 'PartAn SI' by Microtrac Gmbh

Number-weighted diameters have a 'N' and a percentage number as subscript, while volume-weighted diameters have a 'V' instead the 'N'. These diameters represent the particle size to which the given percentage of the particle number / volume is spread on all particles with smaller or similar size. As an example, 50 % of the entire particle volume is spread on particles with smaller or similar size than d_{V50}. Number-weighted and volume-weighted diameters are given for a rough size characterization in **Table 4** and **Table 5**.

These tables also contain particle material properties which are used for analytical calculations. The parameter σ is the Yield strength or the elastic limit of the material and the parameter E is the Young's modulus. The material data are taken from [14] and [69]. The specific heats c_p are taken from [14] and [70].

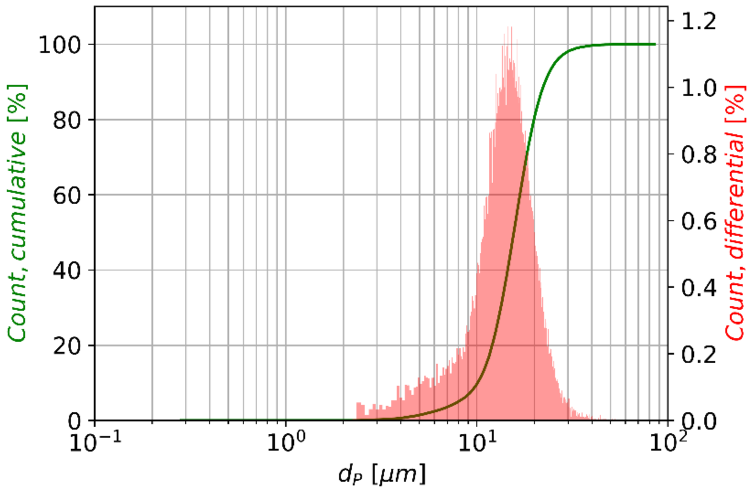

Fig. 24 Cumulative and differential particle number distribution of MgO particles measured with a 'PartAn SI' by Microtrac Gmbh

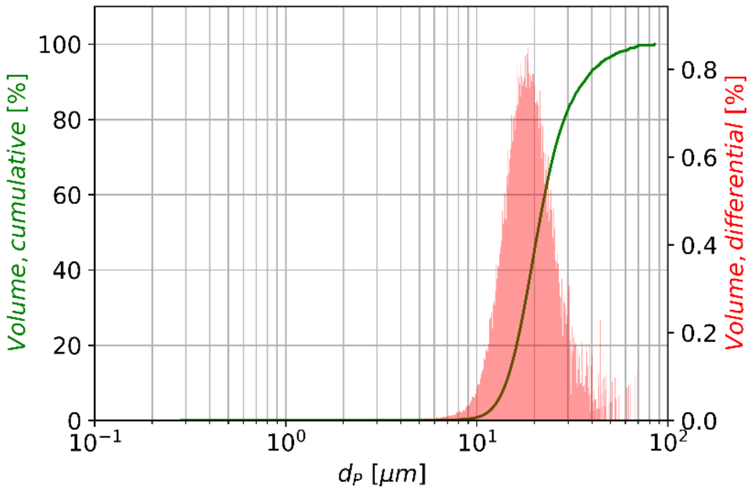

Fig. 25 Cumulative and differential particle volume distribution of MgO particles measured with a 'PartAn SI' by Microtrac Gmbh

Table 4 Characteristic diameters of particles used for PIV applications

particles	**manufacturer, material name**	**data source**	d_{N50}	d_{V50}	**σ**	**E**	c_p
unit	[-]	[-]	[µm]	[µm]	[GPa]	[GPa]	[J/(kg K)]
PIV-MgO	Lehmann & Voss & Co. KG, LUVOMAG M SF	Microtrac PartAn SI	5.98	20.32	1.25	300	1029
		Microtrac S3500	0.17	2.42			

Table 5 Characteristic diameters of particles used for heating augmentation analysis

particles	**manufacturer, material name**	**data source**	d_{N50}	d_{V50}	**σ**	**E**	**c_p**
unit	[-]	[-]	[µm]	[µm]	[GPa]	[GPa]	[J/(kg K)]
Al_2O_3	H.C. Starck GmbH, Amperit 740.065	Microtrac PartAn SI	19.9	26.3	0.74	320	1100
		Microtrac S3500	14.76	22.11			
MgO	Lehmann & Voss & Co. KG, LUVOMAG M-045, sieved	Microtrac PartAn SI	14.19	18.63	1.25	300	1029
		Microtrac S3500	10.51	18.23			
SiO_2	sigmaaldrich, Merck SA, 83340	data sheet	> 230 mesh		0.37	100	1226

3.7. Gas Constants

All conducted tests were performed in air. The relevant gas constants are summarized in **Table 6**. Since only one nozzle configuration was used, also the Mach number was constant for all tests.

Table 6 Gas constants

parameter	**unit**	**value**
γ	-	1.4
R	$m^2 / (s^2 K)$	287.058
$c_{p\ gas}$	$m^2 / (s^2 K)$	1004.798
Pr	-	0.71
Ma	-	2.1

3.8. Material Constants

Characteristic probe and coaxial-thermocouple material properties are summarized in **Table 7**. These values were required for the analytical calculations. The parameters ρ, E, σ, c, and k are the material density, Young's modulus, Yield strength, heat capacity, and the heat conductivity, respectively.

Table 7 Probe and coaxial thermocouple material properties

probe material	**manufacturer**	**material name**	**ρ**	**E**	**σ**	**c**	**k**
unit	[-]	[-]	[kg/m³]	[GPa]	[GPa]	[J/(g K)] at 293 K	[W/(m K)] at 293 K
stainless steel	Ugine	1.4539	8000	195	0.263	0.5	12
constantan	Isabellenhütte Heusler GmbH	Isotan	8900	160	0.25	0.41	23
chromel	Isabellenhütte Heusler GmbH	Isatherm-	8700	180	0.40	0.45	19

4. Flow Analysis of the GBK Facility

4.1. Purposes & Structure

Before analysing complex particle-laden supersonic flows, a basic knowledge about the implemented hardware and the general flow environment of the GBK test facility is required. Therefore, this section focusses on the stability of the GBK flow temperature and -pressure as well as on the uniformity of the flow field close to the nozzle exit. Since flow turbulence can have a significant impact on stagnation point heat fluxes [31], the flow turbulence intensity of selected flow conditions of the GBK facility is estimated to consider its influence on the following heating augmentation analyses. The flow turbulence intensity is derived from PIV and PTV measurements. As it is proposed in [71], the PIV interrogation window size (IW) acts as a spatial filter for turbulent structures. So, the final IW was varied in order to consider these filtering effects on the detected turbulence intensity.

Finally, a general measurement uncertainty of the presented optical measurement technique setup (see **section 3.5**) is derived, which is required for particle mass flow rate uncertainty estimations as done in **section 5**.

The purposes of this section are summarized as follows:

- Qualitative analysis of flow condition stability
- Qualitative analysis of the flow field close to the nozzle exit
- Determination of measurement uncertainties of the high-resolution and the low-resolution camera system
- Determination of freestream turbulence for selected flow conditions in particle-free GBK flows and its dependence on the chosen PIV / PTV interrogation window size

The agenda of this section is organized as follows: First, the experimental setup is described, followed by turbulence intensity formulations and a detailed explanation of the PIV and PTV data processing.

Regarding analyses, first the GBK flow stability is addressed. Then, PIV data of the flow field is analysed in terms of uniformity and the measured flow velocity is compared to isentropic calculations. According to **eq. (4-3)**, the PIV and PTV measurement uncertainty is required to estimate the flow turbulence. As a consequence, first the measurement uncertainties, including a peak-locking analysis, are investigated, followed by the determination of the flow turbulence intensity.

4.2. Methods

4.2.1. Test Facility Setup

The general test facility setup is described in **section 3.4.1**. The seeding device is controlled by the three-way-ball valve, as suggested in [65], which is depicted in **Fig. 7**. In contrast to **Fig. 8**, no aerosol spectrometer, but a closed container was mounted on the injection collection probe.

4.2.2. Non-Intrusive Measurement Technique Setup

The two sCMOS cameras of the high-resolution system are named C1 and C2. These had a maximum number of pixels of 2560 x 2160 px². These cameras are able to increase the double-frame rate by reducing the recordable sensor area. To avoid double exposure by the 100 Hz laser system, only a central sensor area of 2560 x 1060 px² for C1 and C2 was used, leading to a double-frame rate of 50 Hz for each camera. The long-distance microscope led to a scale factor (SF) of 211.2 px/mm for C1 and C2. The implemented Cf-1b lens offered the highest available resolution in the image center, but coma effects in the image edges reduced the evaluable image size (see **Fig. 26** in **section 4.2.4**). Another K2 Distamax lens is recommended with a larger depth of field and less coma effects at the edges (e.g. Infinity I lens) for PIV investigations. However, the chosen lens seems to be appropriate for shadowgraphy measurements due to its higher resolution in the image center.

The aperture of the long-distance microscope was set to the middle position, resulting in an aperture opening of approximately 17 mm in diameter. C1 was used for shadowgraphy and equipped with a 550 nm long-pass filter, while C2 was used for PIV and equipped with a 532 nm bandpass filter. Shadowgraphy was intentionally made for comparison reasons, to see which influence small particles might have on the shadowgraphy background illumination. While C1 was not capable to detect particle shadows of the seeded particles, C2 recorded slightly unfocussed particle images with sizes of 5 - 8 px.

The low-resolution recording system, called C3 in the following, provided a scale factor SF of 40.6 px/mm. The lens aperture was set to f/11. The active sensor pixel area was reduced to 168 x 1600 px² to avoid double exposures by the 100 Hz laser system. The resulting double-frame rate of C3 was 50 Hz. The C3 particle image size was 1 - 2 px.

The laser sheet thickness was determined by aid of a scale to be approximately 1 mm. The nominal double-pulse time separation Δt between the PIV double images was set to 400 ns. It was checked by an additional photodiode which measured a mean time separation of 409 ns. The difference in nominal and measured time separation would lead to up to 2.3 % higher particle velocities, if the measured signal is not considered. In the following, the measured time separation is taken for calculations. To avoid systematic errors in PIV measurements in general, especially with pulse time separations < 1µs, a verification with an additional photodiode is mandatory.

Apart from that, the pulse time separation is not constant but it varies up to some nanoseconds for every double-pulse. This variation is called 'laser jitter' or just 'jitter' in the following and is expressed by Δt_{jitter}. The measured laser jitter for all tests is given in **Table 8**.

Both C1 and C2 were calibrated using the ParticleMaster calibration plate made from LaVision GmbH, illuminated by the shadowgraph diffusor. C3 was calibrated using a 3D calibration plate from LaVision GmbH.

In the following, only the PIV data from C2 and C3 are considered and compared to each other; the shadowgraphy data from C1 is excluded from further processing in this section, because the used PIV-MgO particles were too small for shadowgraphy recordings.

4.2.3. Test Conditions

The PIV-MgO particles were used for flow seeding (see **Table 4**). Before filling the particles into the seeding device, no additional treatment like heating or sieving was applied.

The bypass three-way-ball-valve was used to control seeding. It opened when constant flow conditions in the GBK facility were achieved, and closed, when the measurement time of approximately 23 s was over. No probe was inserted into the flow during the measurement time.

The theoretical nozzle exit velocities (V_{theo}) are the gas velocities at the nozzle exit. These were calculated with one-dimensional isentropic formulations. In this section, the reference condition is T_0 = 373.4 K p_0 = 0.95 MPa of run V60.

Table 8 Flow conditions for turbulence intensity measurements

run ID	T_0 [K]	p_0 [MPa]	V_{theo} [m/s]	Δtjitter / Δt [%]
V58	374.6	0.494	593.8	0.14
V59	374.2	1.382	593.6	0.13
V60	373.5	0.949	593.1	0.14
V61	473.7	0.949	667.9	0.15
V62	302.8	0.949	534.0	0.14

4.2.4. Formulation of Turbulence Intensity

Turbulence intensity (Tu) is the ratio of velocity fluctuations and mean velocity and is defined for two velocity components as follows [31, 71]:

$$\mathrm{Tu} = \frac{\mathrm{V}'}{\overline{\overline{\mathrm{V}}}} = \frac{\sqrt{(\mathrm{u}'^2 + \mathrm{v}'^2)}}{\sqrt{(\bar{\mathrm{u}}^2 + \bar{\mathrm{v}}^2)}} \tag{4-1}$$

The absolute velocity V is the square mean root of the velocity component in x- direction u and the velocity component in y- direction v.

The components u' and v' are the velocity fluctuations in x- and y- direction, respectively. In the process of PIV, velocities are calculated for each individual interrogation window. Parameters marked with a bar represent the temporal mean of an interrogation window. So, it is not the spatial mean of the complete FOV.

Following [71], the velocity fluctuations, measured with PIV, V'_{meas} is the sum of the squared velocity fluctuation coming from flow turbulence V'_{Tu} and the squared measurement PIV uncertainty $V'_{PIV\ Unc}$. Because of the short pulse separation times, velocity fluctuations caused by the laser jitter V'_{Laser} are considered as well:

$$\mathrm{V'^2}_{\mathrm{meas}} = \mathrm{V'^2}_{\mathrm{Tu}} + \mathrm{V'^2}_{\mathrm{PIV\ Unc}} + \mathrm{V'^2}_{\mathrm{Laser}} \tag{4-2}$$

Dividing **eq. (4-2)** by the squared temporal mean absolute velocity it follows:

$$\frac{\mathrm{V'^2}_{\mathrm{meas}}}{\overline{\mathrm{V}}^2} = \mathrm{Tu}^2 + \frac{\mathrm{V'^2}_{\mathrm{PIV\ Unc}}}{\overline{\mathrm{V}}^2} + \frac{\mathrm{V'^2}_{\mathrm{Laser}}}{\overline{\mathrm{V}}^2} \tag{4-3}$$

The second term on the right-hand side is the squared relative measurement uncertainty of PIV. In general, the measured PIV velocity can also be expressed with the position shift within the two PIV frames, given in pixels, named ΔX. The relation between ΔX and V is:

$$\Delta\mathrm{X}^2 = \mathrm{V}^2 * \Delta\mathrm{t}^2 * \mathrm{SF}^2 \tag{4-4}$$

In **eq. (4-4)**, the measured PIV velocity is multiplied with the mean pulse time separation and the scale factor to get the corresponding pixel shift. The PIV measurement uncertainty $\Delta\mathrm{X'}_{\mathrm{PIV\ Unc}}$, given in px, is:

$$\Delta\mathrm{X'^2}_{\mathrm{PIV\ Unc}} = \mathrm{V'^2}_{\mathrm{PIV\ Unc}} * \Delta\mathrm{t}^2 * \mathrm{SF}^2 \tag{4-5}$$

Summarizing **eqs. (4-4)** and **(4-5)**, the squared relative measurement uncertainty of PIV can be expressed by:

$$\frac{\mathrm{V'^2}_{PIV\ Unc}}{\overline{\mathrm{V}}^2} = \frac{\Delta\mathrm{X'^2}_{\mathrm{PIV\ Unc}}}{\Delta\mathrm{X}^2} \tag{4-6}$$

The third term of **eq.(4-3)** can be expressed by the ratio of the laser jitter and the pulse time separation :

$$\frac{\mathrm{V'^2}_{\mathrm{Laser}}}{\overline{\mathrm{V}}^2} = \frac{\Delta\mathrm{t_{jitter}}^2}{\Delta\mathrm{t}^2} \tag{4-7}$$

4.2.5. PIV and PTV Data Processing

PIV vector data were first generated by the help of DaVis 10.1 software by LaVision GmbH. The PIV uncertainty was estimated by means of the correlation-statistics method [72]. This method is based on a post-processing of differences between the two PIV images.
Also, PTV from PIV correlation was applied and is called PTV in the following. It is referenced as 'IW = 0 mm' in the plots, although its correlation window size was set to 16 px for C2 and to 8 px for C3. Uncertainty estimation of PTV is a recent topic of interest (e.g. [73, 74]). Since DaVis 10.1 does not include the possibility to calculate the measurement uncertainty of PTV, a PIV analysis with IW size smaller than the PTV correlation window size (C2: 8 px, C3: 3 px) was performed and the uncertainty value of PIV data were transferred to PTV data. The found particle positions via PTV acted as a 'pointer' to select the corresponding PIV IW vector uncertainty data. The statistical analysis of all vector data was performed with an additional in-house developed Python script.

To properly compare the achieved data of C2 and C3, only the overlap FOV was chosen. The overlap FOV was further reduced due to several reasons, as visualized in **Fig. 26**. On the left- and right-hand side, the two frames of C2 and C3 are shown, respectively. At higher stagnation temperatures, the laser sheet moved towards the nozzle, resulting in a poor PIV illumination on the right-hand side in run V61, so that the area right to the red line was excluded. A further exclusion was done due to coma effects at the top and bottom in C2 images which is marked with the green lines. The area at the left side from the purple line is unconsidered due to nozzle reflections recorded in C3. All vectors within the remaining center rectangle are used for further analyses and turbulence intensity measurements. The remaining FOV size was 1.6 x 7.3 mm². Around 1150 images were taken for each run.

No image pre-processing was performed for PIV evaluation. Multi-pass vector calculation methods were applied with an initial interrogation window size of 512 x 512 px for C2 and 128 x 128 px for C3. The final pass was gaussian-weighted, the overlap of all passes was 50 %. Vector post-processing was performed only with the in-house developed Python script to remove vector outliers. Spurious vectors may significantly affect standard deviation or fluctuation values. Three different filters were applied, see **eqs. (4-8)**, **(4-9)**, and **(4-10)**.

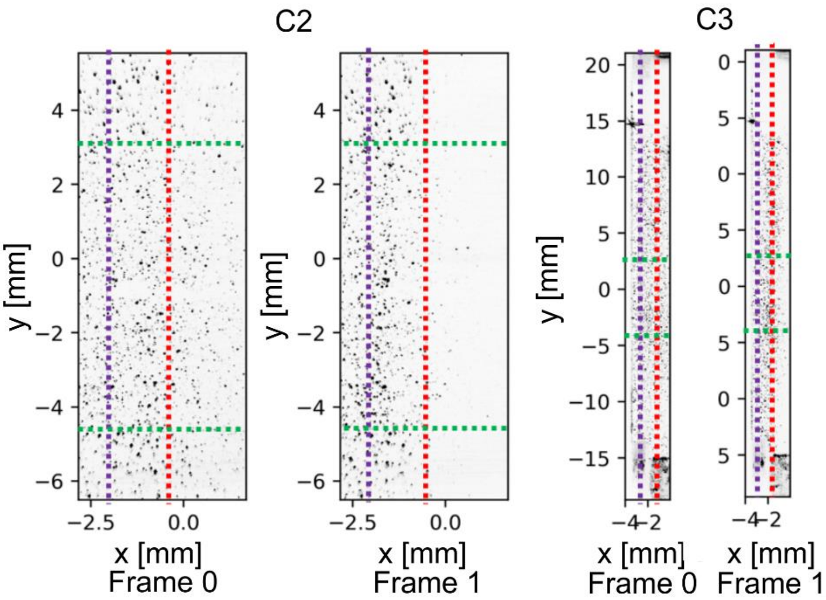

Fig. 26 Inverted PIV Images of C2 and C3, showing the overlap FOV as central rectangle between dotted lines

The first filter was a standard outlier filter, based on quantiles instead of standard deviations, because a spatial velocity gradient over the valid centered image area was observed (see **Fig. 28**), leading to non-gaussian velocity distributions. Vectors were filtered out, if they did not fulfil **eq. (4-8)**, in which the medians are marked with a tilde, while the first and third quantile are marked with q1 and q3, respectively.

$$\begin{gathered} u > \tilde{u} - 1.5 * (\tilde{u} - u_{q1}) \wedge \\ u < \tilde{u} + 1.5 * (u_{q3} - \tilde{u}) \wedge \\ v > \tilde{v} - 1.5 * (\tilde{v} - v_{q1}) \wedge \\ v < \tilde{v} + 1.5 * (v_{q3} - \tilde{v}) \end{gathered} \tag{4-8}$$

Filter two removed vectors which provided an PIV uncertainty larger than 10 % of the global mean velocity (see **eq. (4-9)**). This filter only affected data of C3, where the resolution and particle image size are low:

$$\frac{V'_{\mathrm{PIV\,Unc}}}{\overline{V}} < 10\% \tag{4-9}$$

The third filter removed data for which the square of the measured fluctuation is smaller than the square of the PIV uncertainty (see **eq. (4-10)**). This filter was only applied for turbulence determination and not for the standard PIV velocity field evaluation as shown in **Fig. 28**:

$$\frac{V'^{2}_{\mathrm{meas}}}{\overline{V}^{2}} = \frac{(V - \overline{V})^{2}}{\overline{V}^{2}} > \frac{V'^{2}_{\mathrm{PIV\,Unc}}}{\overline{V}^{2}} \tag{4-10}$$

4.3. Analysis

In the following, first the GBK flow stability is addressed. Then, PIV data of the flow field is analysed in terms of uniformity and the measured flow velocity is compared to isentropic calculations. According to **eq. (4-3)**, the PIV and PTV measurement uncertainty is required to estimate the flow turbulence. As a consequence, first the measurement uncertainties are investigated, followed by the determination of the flow turbulence intensity.

4.3.1. GBK Flow Stability and Flow Field

To avoid influences of any pressure or temperature fluctuations of the GBK flow itself on heating augmentation measurements, first the GBK flow stability and flow field is analysed. To determine flow stability the temporal changes of the stagnation pressure and the stagnation temperature are considered. These are plotted in **Fig. 27.** The red vertical dashed lines in **Fig. 27** indicate the start and the end of the measurement time.
The three-way-ball-valve was switched to open the air supply of the seeding device and hence, to start particle seeding. At the beginning of this switch a stagnation pressure drop of around 0.008 MPa and a stagnation temperature increase of around 0.8 K was detected for around 5 s. When closing the air supply of the seeding system with the help of the three-way-ball-valve, opposite effects were measured. This can be explained by the seeding device's air volume and the piping connection between seedings device and the seeding device's bypass (see **Fig. 7**). Before the three-way-ball-valve is opened, the GBK bypass pipes are cooled by the expanded and unheated bypass flow to a lower temperature than ambient temperature. The seeding device is pressurized on the choke's back end level. The air volume in the seeding device has an ambient temperature. When opening the three-way-ball-valve, the seeding device air volume pressure is increased from the choke's back end level to its front end level. For this time period, the GBK bypass pressure and air mass flow drops. When closing the three-way-ball-valve, the seeding device air volume is depressurized, so that the bypass air mass flow is increased shortly, resulting in a short pressure and mass flow increase. During these mass flow changes, the mixing ratio of the heated GBK main flow and the unheated GBK bypass flow is changed, resulting in short temperature changes. Because the seeding device air volume and its piping are on ambient temperature, and not on a lower level like the seeding device's bypass piping, they are transferring heat to the expanded bypass flow, resulting in a higher temperature level than before opening the three-way-ball-valve. For the following PIV evaluation, only data at constant pressure and temperature values were considered.

Since pressure and temperature peaks and drops especially at the beginning of the seeding could have potential impact on the following heating augmentation analyses, the switch of the three-way-ball-valve to control the particle seeding is not feasible. The control of particle seeding without affecting the flow is a high importance in future studies. It can be anticipated that an innovative seeding control was developed at DLR AS-HYP, which makes the three-way-ball-valve as well as the seeding device bypass unnecessary. As a consequence, pressure and temperature fluctuations can be reduced. This control was used in **section 5** and **section 6**. This seeding control is part of a patent process, so no detailed information can be given at the moment.

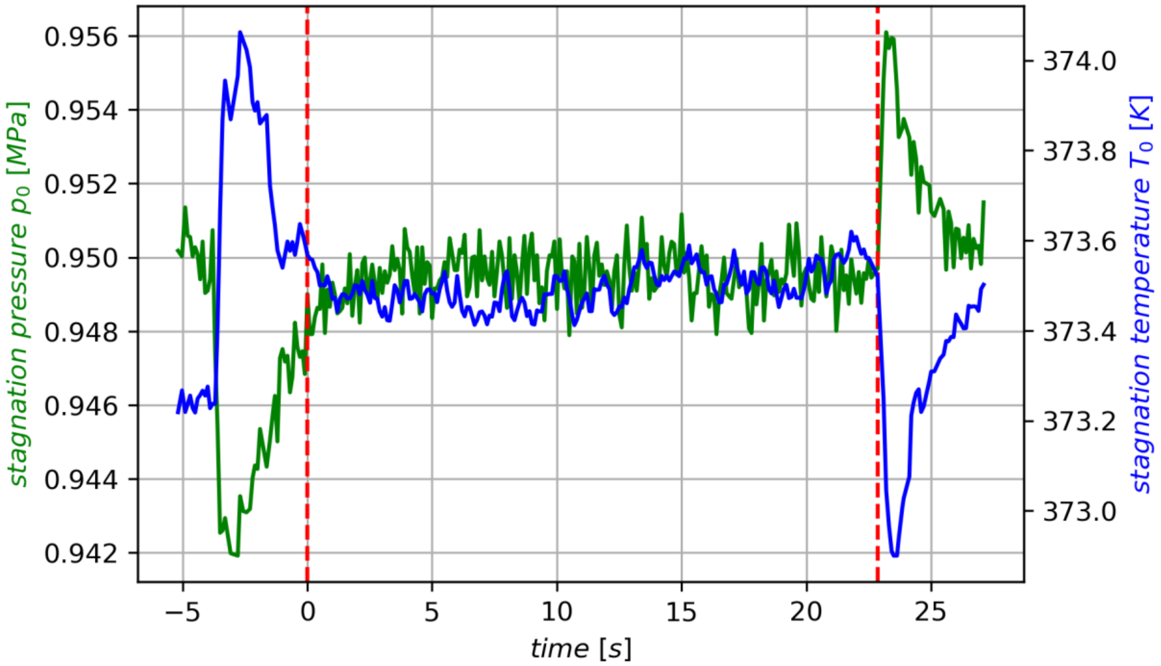

Fig. 27 Stagnation pressure p_0 peaks and stagnation temperature T_0 peaks are caused by the switch of the three-way-ball-valve (before and after the red dashed lines, test run V60)

To investigate flow uniformity at the nozzle exit, the filtered (filter 1 and 2) relative difference between measured temporal mean- and calculated theoretical velocity is considered. The relative flow field of test run V60 is exemplarily shown in **Fig. 28**. The qualitative flow field of all investigated flow conditions is similar. Regardless of which flow condition is investigated, there is a negative x-velocity gradient of up to -0.4 % in flow direction. This could be caused by optical distortions due to density gradients within the test chamber. A calibration misalignment can be excluded, since an uncalibrated PIV evaluation also led to a comparable x-velocity gradient. Also any coma effects can be excluded, since they would lead to a positive velocity gradient. Since velocity spreads of up to 10 % of similar sized particles are found in **section 5.3.1**, it is assumed that the effect of the found velocity gradient on particle-induced heating augmentation analyses can be neglected.

To quantify differences between experiments and calculations, the maximum normed differences for all flow conditions are given in **Table 9**. The PIV evaluation shows that the measured PIV velocity in the overlap region of C2 and C3 is in good agreement with the theoretical estimated value. The maximum difference is -1.4 % for test run V61. It can be concluded that the temperature and pressure measurements of the GBK, which are required for theoretical velocity calculation, as well as the PIV measurements are valid.

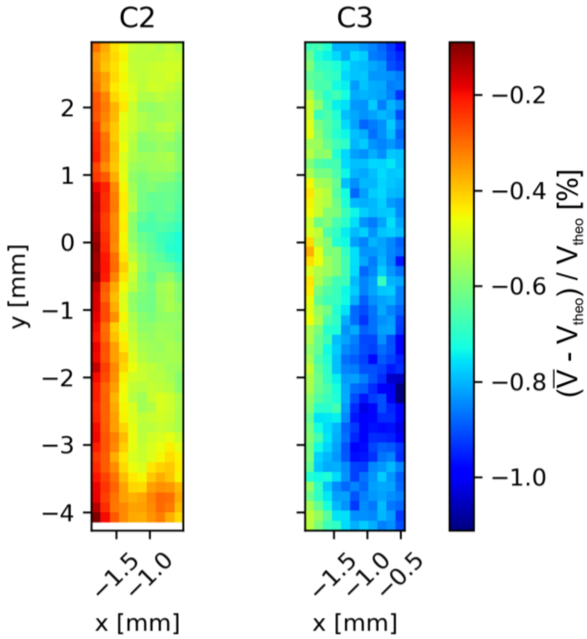

Fig. 28 Normed difference of measured temporal mean and theoretical particle velocity, run V60, IW ~ 0.3 mm (C2: 64 px, C3: 12 px)

Table 9 Maximum differences between measured and calculated velocities

run ID	V_{theo} [m/s]	C2: max. $\frac{\overline{V}-V_{theo}}{V_{theo}}$ [%]	C3: max. $\frac{\overline{V}-V_{theo}}{V_{theo}}$ [%]
V58	594.08	-0.4	-0.8
V59	593.76	-0.7	-1.0
V60	593.21	-0.7	-1.0
V61	668.06	-1.3	-1.4
V62	534.12	-1.0	-1.3

4.3.2. Measurement Uncertainty Estimation

Before estimating the general measurement uncertainty, the experimental PIV and PTV data is analysed in terms of peak-locking effects, because these are one of commonly known PIV data misinterpretation errors [65]. To do so, velocity histograms are considered to check whether the processed data is affected by peak-locking [71]. If peak locking affects the data, histogram peaks appear at integer pixel shifts. In **Fig. 29** and **Fig. 30**, the velocity histograms of C2 and C3 are shown, respectively. These figures contain all filtered (filter 1 and filter 2) vector data of the overlap region.

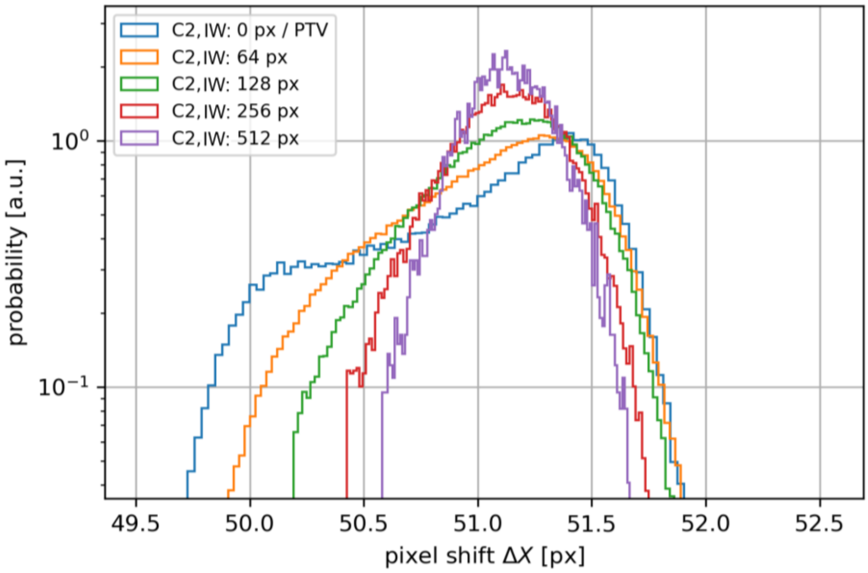

Fig. 29 Velocity histogram of C2, run V60

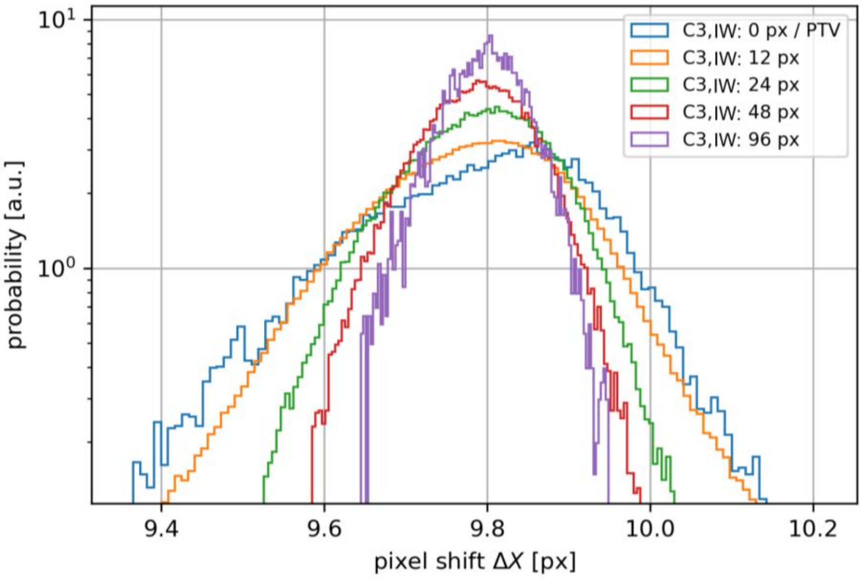

Fig. 30 Velocity histogram of C3, run V60

The shown velocity distributions are smooth and do not contain multiple peaks. As a consequence, PIV-related peak-locking effects can be excluded. The distribution deviates from gaussian for smaller IW sizes, especially for PTV, which is caused by the velocity gradient in the overlap region (see **Fig. 28**).

The general measurement uncertainty is of fundamental interest and is required for the determination of flow turbulence intensity (see **section 4.3.3**) and for estimating particle mass flow rate uncertainties (see **section 5.3.4.1).** The determined measurement uncertainties for C2 and C3 in relation to the chosen IW size are plotted in **Fig. 31**. While the dots represent the median of all valid vector data (filter 1-3), the filled bars represent the corresponding interquartile range IQR. With decreasing IW size, the measurement error increases. This can be explained by the fact, that smaller IW sizes contain less data for the cross-correlation, which let increase the uncertainty of the cross-correlation analysis. The resulting measurement uncertainty for PTV is depicted in **Fig. 31** as data points at IW = 0.0 mm. This uncertainty seems to be reasonable, since it increases smoothly with decreasing IW size. However, the presented PTV measurement uncertainty approach should be compared to other PTV uncertainty approaches, e.g. [74], although these approaches are still in development.

The largest median measurement uncertainty is considered as measurement uncertainty in the following. These values are approximately 0.2 px and 0.1 px for C2 and C3, respectively. These values are additionally summarized in **Table 10**. The C3 result is close to the common value of 0.1 px for estimating PIV uncertainty [65]. The found C2 uncertainty is larger than the common PIV uncertainty value, which can be explained by the significant larger optical magnification. The found measurement uncertainties are used for all following uncertainty calculations, since the camera and lens setup is very similar. This means that PTV uncertainty estimations of C2 are applied to shadowgraphy data, since both techniques are based on individual particle detection algorithms.

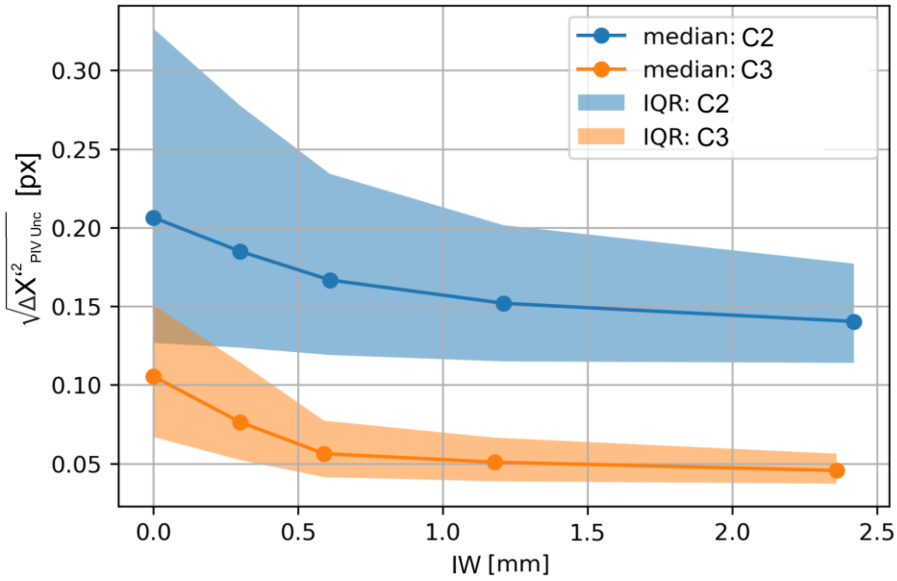

Fig. 31 Measurement uncertainty for C2 and C3 in relation to the chosen IW size

Table 10 Measurement uncertainty for all cameras

camera	$\Delta X'_{\mathrm{PIV\ Unc}}$ **[px]**
C2 (= C1)	0.2
C3	0.1

4.3.3. Flow Turbulence Intensity

With the help of the measurement uncertainty estimated in the previous section and the measured laser jitter (see **section 4.2.2**), the flow turbulence intensity can be determined (see **eq. (4-3)**). The flow turbulence intensity is required to estimate its effect on stagnation point heat fluxes and particle-induced heating augmentation effects.

The equation **eq. (4-3)** is applied on the filtered (filter 1-3) valid vector data to estimate turbulence intensity. To avoid effects of the detected velocity gradient (see **Fig. 28**) on the turbulence intensity estimation, all velocity data are related to the temporal mean of the respective IW, and not a global mean velocity of the entire FOV.

The resulting medians and IQRs of the turbulence intensity in relation to the chosen IW size for test run V60 are depicted in **Fig. 32**. Since the number of valid vectors for the C3 PTV evaluation is less than 1000, this datapoint was excluded from further consideration. The calculated median Tu values for each camera barely coincide within their IQR range. This behaviour was also observed for the other investigated flow conditions. Because C3 provides a lower optical resolution and because the PTV median is based on significantly less vectors than the PIV median of the smallest IW size (1513 vs. 231669), the third quantile (upper bound of IQR) value of C2 with IW = 64 px (~ 0.3 mm) is chosen as a conservative estimation for turbulence intensity. This value is marked as a red dashed line in **Fig. 32**.

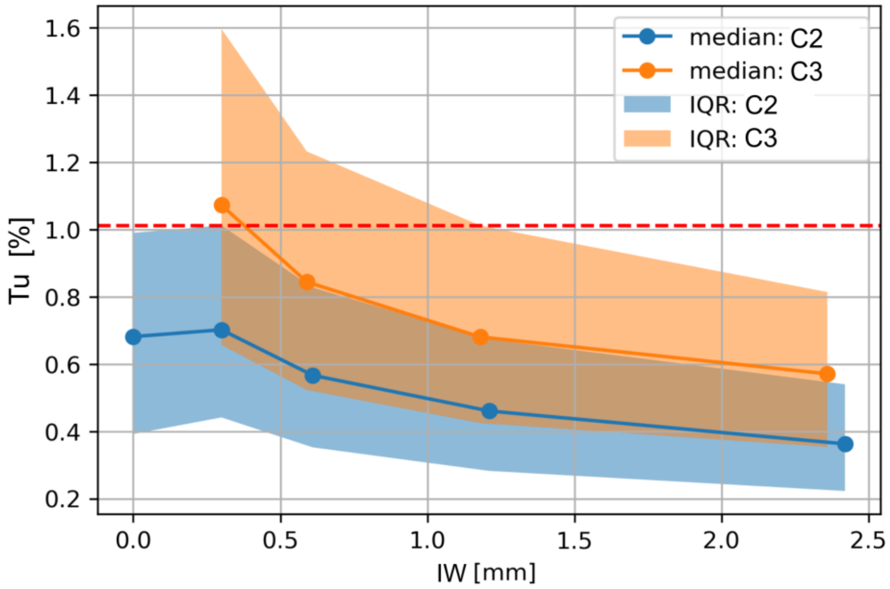

Fig. 32 Measured turbulence intensity for C2 and C3 in relation to the IW size, run V60

The turbulence intensities for all investigated flow conditions are summarized in **Table 11**. Not only the stagnation conditions but also the freestream Reynolds number, based on 1m, $Re_{\infty 1m}$, is listed. The measured turbulence intensity does not differ strongly from approximately 1 % for all investigated flow conditions. This relatively low turbulence intensity allows to assume that no turbulent particle-free flow is present in the GBK facility and that the measured stagnation point

heat fluxes (see **section 6.3.1**) can be estimated with common laminar stagnation point heat flux approximations. A turbulence intensity of 1 % is assumed for all test conditions in the following.
If the analysis of the turbulence intensity is extended, the results of the presented procedure can be cross-checked with a pulse-time variation procedure for turbulence measurements, as proposed in [71].

Table 11 Determined flow turbulence intensities for investigated flow conditions

Run ID	**T_0 [K]**	**p_0 [MPa]**	**$Re_{\infty 1m}$ [-]**	**Tu [%]**
V58	374.6	0.494	$4.24*10^7$	**0.94**
V59	374.2	1.382	$1.19*10^8$	**0.88**
V60	373.5	0.949	$8.18*10^7$	**1.03**
V61	473.7	0.949	$5.96*10^7$	**1.08**
V62	302.8	0.949	$1.09*10^8$	**1.06**

4.4. Conclusion

In this section, fundamental analyses of the GBK facility, of its flow, as well as of the general optical setup were made. The results of this section are summarized as follows:

- The use of the three-way-ball-valve is not appropriate to control particle seeding, since it generates pressure and temperature oscillations when it is active
- The pulse time separation must be controlled by an additional photodiode to exclude systematic timing errors
- No peak-locking effects were observed in the PIV analysis, so the setup of the optical systems appears to be appropriate for PIV and PTV
- A negative x-velocity gradient was observed in the flow field close to the nozzle exit for all flow conditions, which can be neglected in particle mass flow rate analyses
- The measured gas velocity is in good agreement with theoretical predictions and maximum 1.4 % lower for all investigated flow conditions
- Measurement uncertainties for the low-resolution camera system are approximately 0.1 px, while they are 0.2 px for the high-resolution camera system
- The flow turbulence is estimated conservatively to be 1 % for all investigated flow conditions

Since the conducted measurements were reasonable, the following sections can focus on measurement technique improvement and individual particle characterization (see **section 5**) as well as on heat flux measurements and heating augmentation analyses (see **section 6**).

5. Individual Particle Characterization

5.1. Purposes & Structure

As pointed out in **section 1**, there is no particle-induced heating augmentation data set in literature, where all relevant particle characteristics, namely number, size, and velocity, were measured simultaneously. To fill this gap, new experiments with an individual particle characterization measurement technique are intended. Shadowgraphy was selected to characterize particles individually, since it is capable to determine particle velocity, size, and projected shape simultaneously and because it can visualize shock structures, which can be affected by rebounded particles (see **section 2**). In this section, an advanced additional correction procedure of shadowgraphy data, achieved with a commercial software code, is presented to minimize uncertainties in the determination of particle size and the measurement volume. The shadowgraphy approach including the additional correction allows measuring quantitative particle mass flow rate G_p values in a small FOV.

In particle-induced heating augmentation literature, G_p is derived from total particle mass measurements and the assumption of spatially and temporally homogenously seeded particles. The total particle mass is the difference of the total particle mass in the respective storage weighted before and after each test run. Since the total particle mass measurement is elaborative, it is tested in this section if the total particle mass measurement can be simplified by using a small particle collection probe.

If it is not assumed that particles are homogenously distributed across the nozzle exit, a spatial resolved qualitative G_p distribution at the nozzle exit is required to reconstruct quantitative G_p values from total particle mass measurements. These distributions are named 'distribution profile' or 'profile' in the following. One approach to get a qualitative distribution profile is based on a light scattering signal, as it was done in [13]. However, this approach does not consider individual particle size or velocity. Another qualitative and quantitative G_p distribution profile approach is tested, which is based on PTV and which considers individual particles.

Since there is no standard particle mass flow rate measurement technique, different quantitative G_p value approaches are compared to each other, namely shadowgraphy, quantitative PTV, qualitative PTV + total particle mass measurement, and the scattered light signal approach. These comparisons help to identify an appropriate measurement approach to determine G_p accurately.

The purposes of this section are summarized as follows:

- Check, if total particle mass measurements can be simplified with the help of a particle collection probe
- Experimental determination of particle density
- Comparison of particle size distributions achieved with several measurement approaches and -devices

- Determination of particle mass flow rate by measuring individual particle characteristics like particle number, size, and velocity
- Estimation of measurement uncertainties for all relevant particle characteristics
- Determination of quantitative particle mass flow rate distribution profiles across the GBK nozzle

The agenda of this section is organized as follows: First, the experimental setup is described, followed by particle flux calculation formulations and a detailed explanation of the implemented measurement approaches.

The first analysis is about the particle density. Here, measured particle velocities at the nozzle exit are compared to one-dimensional isentropic calculations and pycnometer measurements are conducted. Then, particle size distributions are compared to those of commercial measurement devices to estimate the validity of the presented measurement approaches. Finally, G_p distribution profiles are discussed. For all analyses, measurement uncertainties for the respective particle characteristics were derived with the help of an extensive error propagation analysis.

This section summarizes the work described in the publications [15] and [16]. While in [15] particle mass flow rate measurement procedures are established and tested on a specific flow condition, [16] is about the implementation of improvement suggestions, the advanced measurement procedure development, the comparison of the procedure's results with validated measurement techniques, and the application of those procedures on several GBK flow conditions.

5.2. Methods

In the following, first the experimental setup and the test conditions are described. Then, the mathematical formulation to determine particle mass flow rate is presented. This formulation helps to clarify which particle parameters have to be addressed. In the end, it is explained how these particle parameters are derived by means of the implemented measurement approaches.

5.2.1. Test Facility Setup

The general test setup is described in **section 3.4** and **section 3.5** and illustrated in **Fig. 8** and **Fig. 16**. Tests were conducted with a closed container and an aerosol spectrometer mounted at the outlet of the injection probe. Particles were collected with the injection collection probe to check if particle total mass flow can be predicted only with the collected particle mass, while the aerosol spectrometer was used to check the absence of particle seeding beyond the measurement time. The latter one was identified to be a significant error source in determining total particle mass measurements [15]. To avoid pressure and temperature deviations during particle seeding (see **section 4.3.1**), the particle seeding was controlled with an additional mechanical device as part of the seeding system. Due to an ongoing patent process, a detailed description of these devices is not part of this work.

5.2.1.1. Total Particle Mass

Before and after each test, the seeding device as well as the collection probe, if mounted, was weighted. These weightings were used to determine total particle masses. The total particle masses, especially the total particle mass passing the nozzle $M_{p\ nozzle}$ is required for the determination of G_p (see **section 5.2.5**). It is defined as follows:

$$M_{p\ nozzle} = \Delta M_{seeding\ device} - M_{p\ collected} \tag{5-1}$$

The parameter $\Delta M_{seeding\ device}$ is the mass difference of the seeding device before and after each run. The seeding device mass was determined with a Kern DS60K0.2 balance. The total particle mass, collected with the injection collection probe and the closed container, is expressed by $M_{p\ collected}$. It was measured with a Kern PCB 1000-2 balance. The uncertainty of $M_{p\ collected}$ was assumed to be 0.05 g, while the uncertainty of the $\Delta M_{seeding\ device}$ measurement was the spread of weighting the seeding device three times. It was assumed that no particles deposited within the facility. This assumption was confirmed with the aerosol spectrometer measurements, in which no particles during the heat-up and shut-down phase of the GBK facility were detected.

The difference between $M_{p\ nozzle}$ and $\Delta M_{seeding\ device}$ was not measured in runs in which the aerosol spectrometer was installed at the injection collection probe. To fill this lack of information, $M_{p\ collected}$ was interpolated. The interpolation data was taken from runs in which the collection probe was installed.

The relation between collected particle mass $M_{p\ collected}$ and mass differences of the seeding device $\Delta M_{seeding\ device}$ is illustrated in **Fig. 33**. The collected particle mass is around 1/44 of the total particle mass loss of the seeding device. This relation is independent of particle material. In some tests the aerosol spectrometer was installed and hence, $M_{p\ collected}$ could not be determined. For these tests, $M_{p\ nozzle}$ was assumed to be:

$$M_{p\ nozzle} = \Delta M_{Seeding\ device} * (1 - 1/44) \tag{5-2}$$

In runs in which the aerosol spectrometer was installed, no unintended seeding was observed. It is assumed that this was also the case for all other runs.

An idea was to predict $M_{p\ nozzle}$ by only considering $M_{p\ collected}$. Although there is a linear relation between those values, this relation is too noisy for proper prediction in future studies.

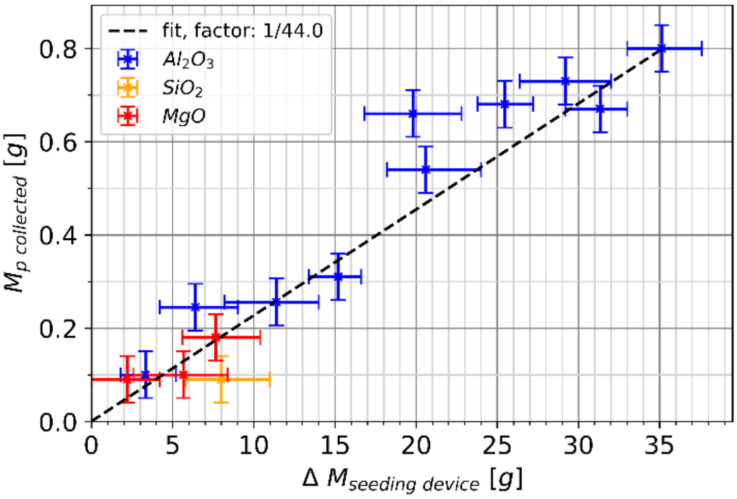

Fig. 33 Relation between total particle mass loss in the seeding device and the particle mass, collected with the injection collection probe

5.2.2. Optical Setup

The non-intrusive measurement technique setup was similar to those described in **section 4**. It included a shadowgraphy system and a PTV setup. An overview of the optical setup is sketched in **Fig. 16**.

The optical magnification of the high-resolution system was increased to 327.5 px/mm by increasing the optical amplification level of the 'Zoom Module'. The aperture control of the long-distance microscope was set to the middle position, resulting in an aperture opening of approximately 17 mm in diameter. C1 and C2 were equipped with a 550 nm long-pass filter. The working distance between lens and focus plane was 361 mm. The resulting shadowgraphy FOV was 3.2 x 7.8 mm². Particle shadow displacements were between 40 and 80 px. The Depth-of-Field (DOF) was less than 6 mm for particles smaller 60 µm.

The low-resolution camera C3 for PTV recordings is identical to those described in **section 4**. Its resulting FOV was 4.1 x 39.4 mm². A 532 nm bandpass filter was placed between focus plane and camera lens. The particle displacements in C3 recordings were between 5 and 10 px.

In first tests the PTV laser sheet thickness was determined by comparing the detected particle number concentration (PpV) of PTV and shadowgraphy (see [15]). Because this procedure depended on shadowgraphy data, an additional calibration was performed to determine laser sheet thickness independently (see **section 5.2.5.2.3**). The laser light intensity was optimized to decrease saturation effects of large particles in the PTV recordings.

The FOVs of both camera systems are sketched in **Fig. 34**: C3's FOV (red rectangle) covered the entire nozzle exit flow, whereas C1 and C2's FOV (blue rectangle) were used for high-resolution image acquisition on the symmetry axis. Only the data in front of the probe bow shock were evaluated to exclude particle deceleration behaviour. The final areas of data evaluation were

1 x 4.8 mm² for shadowgraphy (purple rectangle) and 1 x 30 mm² for PTV. The origin of the coordinate system was located at the probe tip.

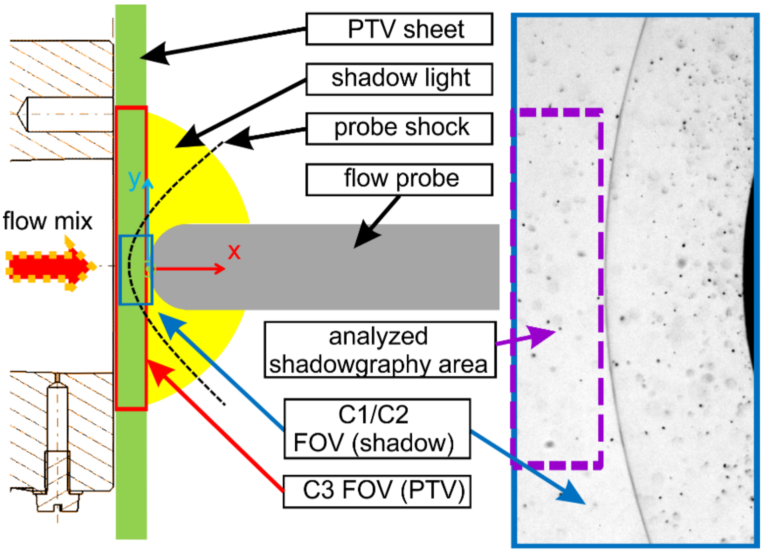

Fig. 34 Sketch of FOVs: shadowgraphy FOV (blue), PTV FOV (red). Only data in front of the shock is evaluated (shadowgraphy: purple)

5.2.3. Test Conditions

A total of 23 tests were considered in the following analysis. While the nozzle contour and the resulting Mach number remained constant, T_0, p_0, and particle material were varied. The unit Reynolds number of the flow (Re_∞) ranged from $5*10^7$ to $1.5*10^8$ per meter. An overview of the considered tests is given in **Table 12**, where the tests are sorted by particle material, T_0, and p_0. The subscript 'main' stands for the heated main flow, while the subscript 'mix by' stands for the particle-laden bypass flow. The measurement locations are sketched in **Fig. 7**. The reference flow condition was $T_0 = 373$ K and $p_0 = 0.96$ MPa. Four different p_0 levels, namely 1: 0.6 MPa, 2: 0.96 MPa, 3: 1.3 MPa, and 4: 1.7 MPa, and five different T_0 levels, namely 1: 303 K, 2: 338 K, 3: 373 K, 4: 473 K and 5: 545 K, were tested with Al_2O_3 particles. For the other materials, only the variation in p_0 was performed. These conditions were selected to cover the entire GBK operation range. A synonym was defined for each run in the form: material – temperature level / pressure level – test run repetition – test type. For example, the synonym 'A-32-1-akin' stands for the run with Al_2O_3 particles, on the third temperature level of 373 K, on the second pressure level of 0.96 MPa, first repetition of an 'akin'-type test. In this section, the test type has no relevance on the results. It is included in the synonym to coincide with the test naming from **section 6**. The active seeding time was set to 10 s. Considering a recording rate of 100 Hz, 1000 shadow images were assumed to be enough for proper particle data statistics. The probe was inserted into the flow for 5 s within the seeding time. This was done to evaluate the G_p measurement approaches in front of the probe. The shadowgraphy and PTV evaluation time of every run t_{meas} is given in **Table 12**.

This time was slightly longer than the active seeding time due to the delay of particles running through the facility.

Table 12 Test matrix, sorted by particle material, T_0, and p_0

synonym	**p_0**	**T_0**	**$\dot{m}_{main}$**	**p_{main}**	**T_{main}**	**$\dot{m}_{mix\ by}$**	**$p_{mix\ by}$**	**$T_{mix\ by}$**	**material**	**t_{meas}**	**connected to collection probe**
	[MPa]	[K]	[g/s]	[MPa]	[K]	[g/s]	[MPa]	[K]	[-]	[s]	[-]
A-11-1-akin	0.594	303.3	496.2	0.600	303.7	29.8	0.602	285.8	Al_2O_3	11.51	Palas: 2070HP
A-12-1-akin	0.958	303.5	798.7	0.958	302.9	45.4	-*)	290.9	Al_2O_3	11.51	Palas: 2070HP
A-13-1-akin	1.289	303.8	1084.2	1.301	304.5	64.4	1.303	285.6	Al_2O_3	11.51	collection container
A-14-1-akin	1.686	304.2	1427.8	1.702	304.9	84.4	1.315	287.9	Al_2O_3	11.52	collection container
A-22-1-akin	0.951	338.5	762.5	0.961	342.6	46.3	0.962	289.9	Al_2O_3	11.51	collection container
A-22-1-qsum	0.950	338.2	746.0	0.959	342.2	46.6	0.959	290.1	Al_2O_3	14.31	collection container
A-31-1-akin	0.593	374.4	444.6	0.600	381.9	26.6	0.599	293.2	Al_2O_3	11.51	collection container
A-31-1-qsum	0.594	373.3	451.3	0.601	381.5	27.0	0.600	294.0	Al_2O_3	14.33	collection container
A-32-1-akin	0.952	374.5	716.8	0.962	381.5	45.1	0.962	292.7	Al_2O_3	11.53	collection container
A-32-2-akin	0.952	374.7	719.2	0.961	382.3	45.5	0.960	290.9	Al_2O_3	11.51	Palas: 2070HP
A-33-1-akin	1.287	373.2	973.3	1.299	379.1	62.7	1.300	293.0	Al_2O_3	11.53	collection container
A-33-1-qsum	1.286	373.2	972.1	1.300	380.3	63.2	1.300	292.0	Al_2O_3	14.31	collection container
A-34-1-akin	1.682	373.0	1273.4	1.699	378.7	82.7	1.698	292.5	Al_2O_3	11.51	collection container

A-34-1-qsum	1.686	373.4	1268.9	1.702	381.5	83.6	1.703	292.4	Al_2O_3	14.31	collection container
A-42-1-qsum	0.952	473.6	633.2	0.961	492.3	46.1	0.963	292.3	Al_2O_3	14.31	collection container
A-52-1-qsum	0.952	544.9	588.5	0.961	573.5	45.5	0.962	293.3	Al_2O_3	17.80	collection container
S-31-1-akin	0.593	374.8	449.2	0.600	383.1	26.7	0.599	292.3	SiO_2	11.51	Palas: 2300HP
S-32-1-akin	0.952	374.0	723.7	0.962	382.2	45.6	0.961	289.7	SiO_2	11.51	Palas: 2300HP
S-33-1-akin	1.288	373.6	973.9	1.301	380.7	63.2	1.301	289.5	SiO_2	11.53	collection container
M-31-1-akin	0.594	373.7	449.2	0.600	383.1	27.6	0.600	290.1	MgO	11.53	collection container
M-32-1-akin	0.950	373.5	720.5	0.959	380.7	45.6	0.959	291.7	MgO	11.51	Palas: 2070HP
M-33-1-akin	1.290	373.7	981.8	1.303	381.5	63.0	1.303	288.9	MgO	11.51	collection container
M-34-1-akin	1.684	373.3	1267.4	1.701	380.3	82.9	1.701	290.4	MgO	11.51	collection container

*) defective sensor

5.2.4. Particle Flux Calculation Formulations

In this section the particle flux calculation formulations are addressed, to get an overview which particle parameters are required to determine particle mass flow rate from individual particle characteristics. An illustration of particle flux calculation based on individual particles is given in **Fig. 35**. The volume-of-interest (VOI) has the dimensions L_y, L_x, and a thickness d. It is located at the position X and Y. All particles which are located in VOI at time t are summarized with n_p (t,X,Y).

The VOI thickness d of the shadowgraphy system depends on the particle size d_p, as shown in **section 5.2.5.1.2**. As a consequence, it is placed within the sigma sign of **eqs. (5-3)**, **(5-4)**, and **(5-5)**. For PTV, d is the light sheet thickness, because it is smaller than the DOF of the PTV system (see **section 5.2.5.2.3**).

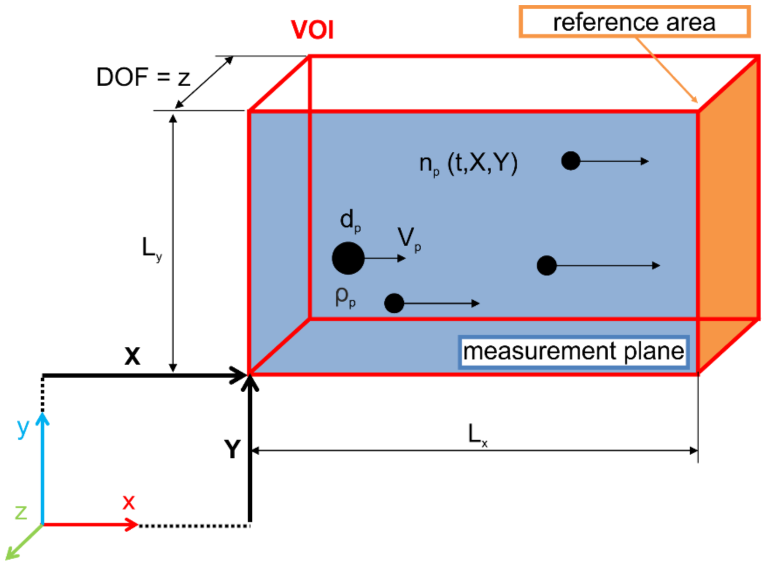

Fig. 35 Sketch of volume-of-interest (VOI) for G_p determination

The particle number concentration or the number of particles per measurement volume is expressed by the abbreviation PpV and is defined as follows:

$$PpV\ (t,X,Y) = \frac{1}{L_x * L_y} * \sum_{i=1}^{n_p\ (t,X,Y)} \frac{1}{d_i}, \quad [PpV] = \frac{1}{m^3} \tag{5-3}$$

The particle mass flow rate G_p can be determined with the following formulation, assuming spherical particles and the same particle density for all particles:

$$G_p\ (t,X,Y) = \frac{4}{3} * \pi * \frac{\rho_p}{L_x * L_y} * \sum_{i=1}^{n_p\ (t,X,Y)} \frac{\left(\frac{d_{p\,i}}{2}\right)^3 * V_{p\,i}}{d_i}, \quad [G_p] = \frac{kg}{m^2 s} \tag{5-4}$$

The particle kinetic energy flux is described with a similar equation. This parameter is important in **section 6**:

$$\dot{e}_{kin}(t,X,Y) = \frac{4}{3} * \pi * \frac{\rho_p}{L_x * L_y} * \sum_{i=1}^{n_p\ (t,X,Y)} \frac{\left(\frac{d_{p\,i}}{2}\right)^3 * V_{p\,i}{}^3}{d\ _i}, \quad [\dot{e}_{kin}] = \frac{W}{m^2} \tag{5-5}$$

The parameter ρ_p is the particle density which is assumed to be constant for all particles. The individual particle size and velocity are expressed with d_p and V_p, respectively.
Data are measured on the x-y measurement plane, while e.g. G_p is referenced on the y-z reference plane. The definition of VOI has influence on the measured G_p, as long as particles are not

distributed homogeneously in the VOI. For example, if the upper half of the VOI in **Fig. 35** is considered, only one particle is counted and hence, G_p would be significantly smaller. Generally, larger VOI result in smooth temporally resolved G_p values, while small VOI sizes compared to particle size lead to mostly zero values with sporadic extrema for G_p, especially in low particle concentration flows.

The particle mass concentration c_m is determined by:

$$c_m = \frac{G_p}{\rho_g \, V_g} \tag{5-6}$$

The parameter V_g is the gas velocity and ρ_g is the gas density.
The particle volume concentration c_v is the particle mass concentration multiplied by the flow/particle density ratio:

$$c_v = c_m \frac{\rho_g}{\rho_p} = \frac{G_p}{\rho_p \, V_g} \tag{5-7}$$

While G_p is a spatially and temporally resolved value, $M_{p\ nozzle}$ is an integral value. By assuming a semi-axisymmetric G_p distribution, the calculated total particle mass $M_{p\ calc}$ can be defined as follows:

$$M_{p\,calc} = \pi * \int_{0}^{t_{meas}} \int_{\frac{-d_{nozzle}}{2}}^{\frac{d_{nozzle}}{2}} G_p(t,y) * |y| * \, dy * dt \tag{5-8}$$

Considering the time-averaged $\overline{G_p}$, **eq. (5-8)** is reduced to:

$$M_{p\,calc} = \pi * t_{meas} \int_{\frac{-d_{nozzle}}{2}}^{\frac{d_{nozzle}}{2}} \overline{G_p}(y) * |y| * \, dy \tag{5-9}$$

The parameter d_{nozzle} is the nozzle exit diameter, while t_{meas} is the evaluation time of shadowgraphy and PTV (see **Table 12**). It is assumed that all particles passed the nozzle during this evaluation time period. A time-resolved Palas aerosol spectrometer was installed to confirm this assumption (see **section 3.4.1** and **section 5.2.1.1**).

5.2.5. Measurement Approaches

The mathematical formulations in **section 5.2.4** have shown, that particle size, particle velocity, particle density, and the size of the measurement volume are required for particle mass flow rate determination, if individual particle characteristics are considered.

Three different approaches are developed to determine particle mass flow rate. While two approaches, namely shadowgraphy and PTV, were used to determine particle mass flow rate from individual particle parameters, the scattered light intensity approach is only capable to estimate particle mass flow rate. An overview of the three approaches to determine G_p is sketched in **Fig. 36**: shadowgraphy (red), PTV (blue), and scattered light intensity (green). The three approaches are interdependent.

In the following subsections, it is explained how particle size, particle velocity, the size of the measurement volume (shadowgraphy and PTV), and the particle mass flow rate (shadowgraphy, PTV, and scattered light intensity) are determined with the respective measurement approach.

It must be noted that the development of the measurement approaches were done iteratively, so that simplified approaches were used in the earliest published research article [15]. The recent processing steps are explained in detail in the respective subsections.

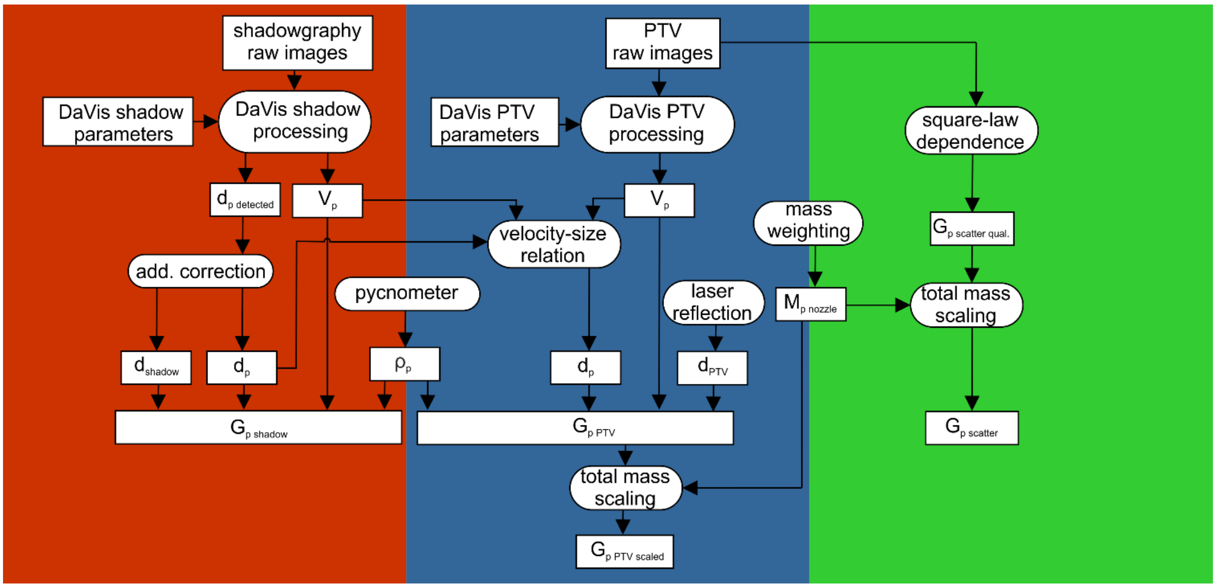
shadowgraphy raw images
DaVis shadow parameters
DaVis shadow processing
$d_{p\ detected}$
V_p
add. correction
d_{shadow}
d_p
pycnometer
ρ_p
$G_{p\ shadow}$
PTV raw images
DaVis PTV parameters
DaVis PTV processing
V_p
velocity-size relation
d_p
laser reflection
d_{PTV}
$G_{p\ PTV}$
total mass scaling
$G_{p\ PTV\ scaled}$
mass weighting
$M_{p\ nozzle}$
square-law dependence
$G_{p\ scatter\ qual.}$
total mass scaling
$G_{p\ scatter}$

Fig. 36 Sketch of shadowgraphy (red), PTV (blue), and scattered light intensity (green) measurement procedures for G_p determination

5.2.5.1. Shadowgraphy Approach

In the framework of the implemented shadowgraphy image processing in this study, particles were detected by means of the LaVision 'DaVis ParticleMaster Shadowgraphy' software. This code has been widely used for particle and bubble characterization, e.g. in [63] and follows the processing steps of image normalization, denoising, binarization, and filtering. Normalization is done with the help of the so-called normalization radius (NorRad), which is the size of a strict-sliding maximum filter. The larger NorRad, the stronger image intensity smoothing effects. Noise reduction can be set with three pre-defined levels ‘weak’, ‘medium’, and ‘strong’. The binarization threshold level (BiThr) divides the normed image into black and white areas (see **Fig. 37**). An overview of all DaVis ParticleMaster Shadowgraphy V10.1 particle detection parameters can be found in **Table 13**.

Table 13 Final detection parameters of LaVision DaVis ParticleMaster Shadowgraphy

parameter name	unit	nominal value
normalization radius NorRad	px	10
pixel noise reduction	-	‘WEAK’
binarization threshold BiThr	%	13
minimum shadow area	px	3
minimum (gradient) slope	%	3
dark level	count	0
maximum size deviation	%	50
particle displacement range in x-direction	px	40±60
particle displacement range in y-direction	px	0±5

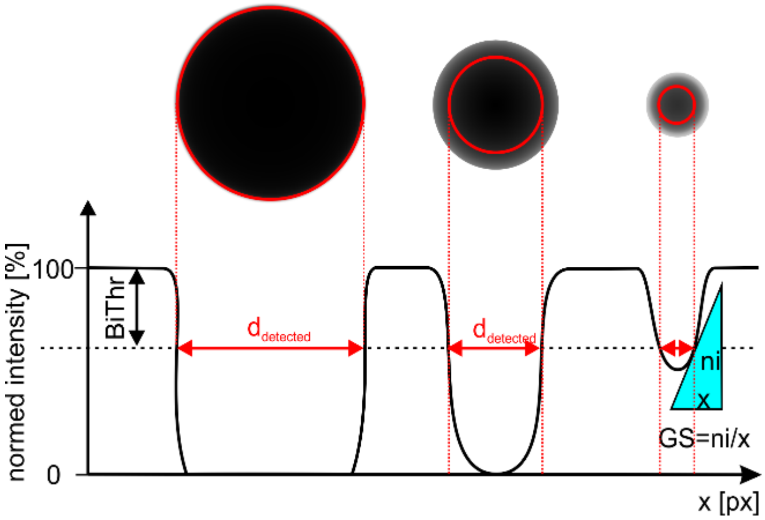

Fig. 37 Gray-levels of differently sized shadows, adapted from [45]. Graphical definitions of BiThr and GS are included

General gray-level distributions for differently sized particle shadows and the definition of BiThr and GS are sketched in **Fig. 37**. As depicted in **Fig. 37** and discussed in [64] for DaVis, the BiThr has significant influence on the detected particle size ($d_{p\ \mathrm{detected}}$). While only large and focused particles are detected with high BiThr values, low values allow detecting also smaller particles, whereby also background noise might be recognized as ghost particles. The default value of BiThr is 50 %, given by LaVision [56].

To measure particles down to 5 to 10 µm in size with the presented optical setup, low binarization thresholds were required, which were significantly lower than the LaVision default value. Furthermore, the minimum detectable shadow area had to be set to 3 px. LaVision states a meaningful minimum value of the minimum detectable shadow area to be 10 px. For lower values, a significant reduction of particle diameter measurement precision has to be expected. To circumvent this, an additional size correction was established. The effect of any particle detection parameter, especially of BiThr, or the NorRad on the particle size measurement can be cancelled out with the additional size correction. As a consequence, the parameter BiThr could be used to control the minimum detectable particle size if applying the additional size correction, while its effect on the final particle size was eliminated. This additional size correction is described in **section 5.2.5.1.1**.

A Depth-of-Field calibration was performed with a customized calibration glass target, containing black dots in the diameter range of 3 to 100 µm, mostly in steps of 5 µm. The target was moved from – 3 mm to 3 mm on the z-axis through the focus plane in 0.1 mm steps (see e.g. **Fig. 3**). Images were pre-processed, so that dirt on the target and the lenses were digitally removed. With the help of these calibration data, an additional size correction procedure was developed and the shadowgraphy measurement volume thickness was defined. It was assumed that the appearance of calibration dots behaves similar to the appearance of particle shadows in a supersonic flow.

5.2.5.1.1. Particle Size Determination

This section explains how particle sizes were determined with the help of shadowgraphy and the additional size correction. The latter one and its application to data from DaVis ParticleMaster-Shadow is described in detail.

Following [45], the additional size correction depended on the measured particle size and the defocus level. It is common to use the intensity gradient at the detected particle boundary as defocus parameter, which is called 'gradient slope' (GS) in the following. It is a measure of particle contour sharpness which again is a measure of particle defocus position. The parameter GS is defined within the ParticleMaster-Shadow software as the normalized intensity decrease per pixel at the detected particle / dot rim [56]. A graphical explanation is given in **Fig. 37**.

In the following, the particle / calibration target dot diameter, provided by DaVis ParticleMaster-Shadow without application of an additional size correction, is named $d_{p\ \mathrm{detected}}$ or $d_{p\ \mathrm{uncorrected}}$. If the size correction is applied it is named $d_{p\ \mathrm{corrected}}$ or just d_p. Since the calibration target dot diameter is known a-priori, this diameter is referenced to be $d_{p\ \mathrm{True}}$. Because $d_{p\ \mathrm{corrected}}$ depends on the size correction quality, it does not need to be the same as $d_{p\ \mathrm{True}}$.

With the help of the DOF calibration, the relation between detected and uncorrected size $d_{p\ \mathrm{detected}}$, GS and true size of the calibration dots $d_{p\ \mathrm{True}}$ was found, which is depicted in **Fig. 38**. The x-axis represents the GS, the y-axis represents the detected dot size $d_{p\ \text{detected}}$, and the dot color represent the true dot size $d_{p\ \text{True}}$. For $d_{p\ \text{True}}$ values larger 20 µm (light green), the detected dot size increase with decreasing GS value, while it is the other way around for $d_{p\ \text{True}}$ values smaller than 20 µm. Dots of the same color are on a line for GS values larger than 15 %. For lower GS values, the points 'spread' around a virtual line. This behaviour can be explained by different dot appearances between dots placed in front of the focus plane, and dots, which were placed behind the focus plane.

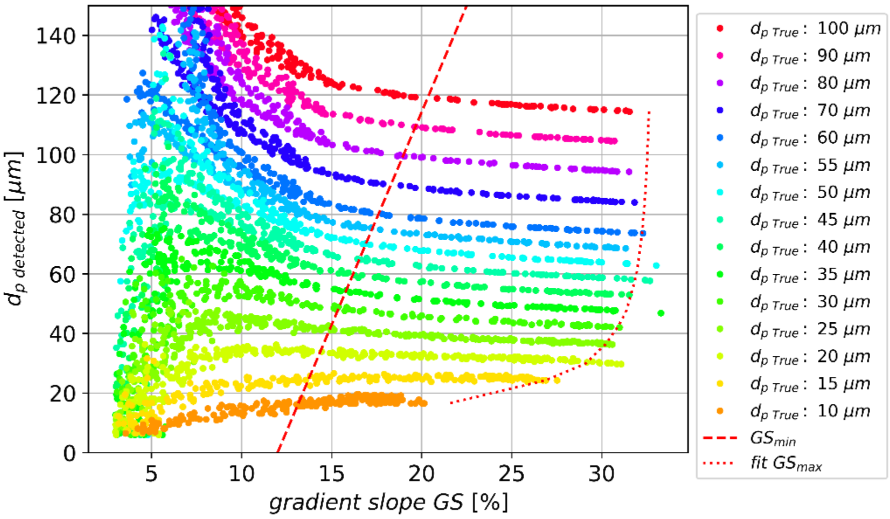

Fig. 38 Relation between detected size, true size and gradient slope GS

The additional size correction required a clear relationship between GS, $d_{p\ \text{True}}$ and $d_{p\ \text{detected}}$, where same-colored dots are on a virtual line. To account only these dots, a minimum GS offset was introduced, which is marked as dashed red line in **Fig. 38**. Only data 'on the right-hand side' of the dashed red line are considered in the following. The crossing of the red dashed line at $d_{p\ \text{detected}} = 0$ µm is called 'minimum GS offset' in the following. The minimum GS limit depended on the relation between $d_{p\ \text{detected}}$, $d_{p\ \text{True}}$ and GS, which again depends on the optical setup and DaVis particle detection parameters. Correction polynomials were defined, allowing to achieve the true size of dots, based on its detected size and GS value. The relation between GS, $d_{p\ \text{detected}}$, and $d_{p\ \text{True}}$ is described by the following generic exponential term:

$$\frac{d_{p\ detected}}{d_{p\ True}} = a + b * e^{-c*\frac{GS}{GS_{max}}}, \qquad a, b, c = f(d_{p\ True}) \tag{5-10}$$

The parameter GS_{max} in **eq. (5-10)** is the maximum gradient slope and depends on $d_{p\ \text{True}}$. It can be described with the following equation:

$$GS_{max} = f + \frac{g - f}{1 + \left(\frac{d_{p\ True}}{h}\right)^{i}} \tag{5-11}$$

It is marked as a red dotted line in **Fig. 38**. The generic parameters f, g, h, and i in **eq. (5-11)** for GS_{max} determination were found with a curve fit on the existing data.

For each $d_{p\ True}$ value the coefficients a, b, and c of **eq. (5-10)** were fit. To achieve the $d_{p\ True}$ value of a measured ($d_{p\ detected}$, GS) couple, distinct ($d_{p\ detected}$, GS) ranges were defined for each $d_{p\ True}$ value. These ranges were defined with a two-dimensional linear interpolation between the measured correction polynomials (see **eq. (5-10)**). These ranges are also called ‘rainbow stripes’ in the following. Exemplary correlations are plotted in **Fig. 39**: each rainbow stripe belongs to a specific $d_{p\ corrected}$. If the detected dots fall within one of the stripes, its size is corrected to the corresponding $d_{p\ corrected}$. Each stripe has a width of 2.5 µm. The lowest defined $d_{p\ corrected}$ is 7.5 µm. It is assumed that the resulting particle size uncertainty is a half of a rainbow stripe width, meaning it is 1.25 µm for each particle.

The correction polynomials were fitted for each segment of the calibration plate, meaning that the correction functions are spatial resolved. A calibration segment has the dimension of 1 x 1.2 mm². The consideration of the correction functions is called additional size correction in the following.

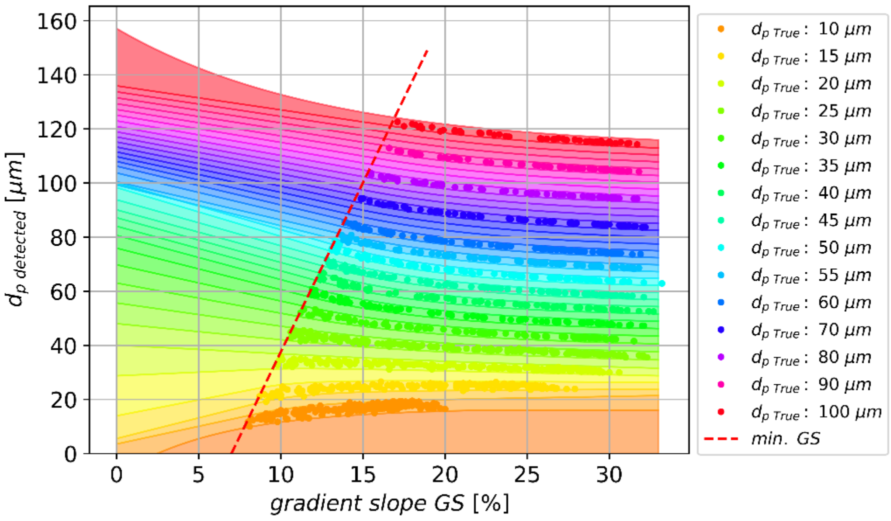

Fig. 39 ‘Rainbow plot’: correlation between detected dot size, GS, true dot size and assigned correct dot size

The quality of this size correction can be described with the size error mean and -standard deviation:

$$\bar{\varepsilon}_{d_{P\,corr}} = \left| \frac{\sum_{i=1}^{n} \frac{d_{p\,corrected,i} - d_{p\,true}}{d_{p\,true}}}{n} \right| \tag{5-12}$$

$$\sigma_{d_{P\,corr}} = \left| \sum_{i=1}^{n} \left(\frac{d_{p\,corrected,i} - d_{p\,true}}{d_{p\,true}} - \bar{\varepsilon}_{d_{p\,corr}} \right)^{2} \right| \tag{5-13}$$

The mean and standard deviation size errors for the uncorrected data were calculated in a similar manner. **Table 14** lists the mean and the standard deviation of the shadowgraphy size errors before (uncorrected) and after application of the additional size correction (corrected). These errors were calculated for the calibration target dots. The size correction leads to significant lower mean and standard deviation of the size error. If all calibration dots of a specific size class were assigned correctly, both the mean and the standard deviation size error are zero. As an initial guess, it is assumed in the following that the maximum size error is caused by the assignment into discrete size classes, resulting in a maximum standard deviation of size error of 1.25 µm.

The minimum detectable size of shadowgraphy ($d_{p\ min}$) is defined as the particle size which can barely be detected, while the minimum size at which all dots can be detected is named $d_{p\ min,\ full}$. Both parameters were determined with the help of the count efficiency (CE) (see **section 5.2.5.1.2** and **Fig. 40**). With the selected settings, 5 µm-large calibration dots were barely detected in the focus plane (z = 0 mm). This size is defined as the minimum detectable size $d_{p\ min}$. The minimum size at which all dots can be detected $d_{p\ min,\ full}$ is 10 µm. For simplicity, it was assumed that particles smaller 10 µm were 'invisible' for shadowgraphy.

Table 14 Size uncertainty before and after additional correction for shadowgraphy, C1

Size Class $d_{p\ True}$ [µm]	**uncorrected:**		**corrected:**			
	$\bar{\varepsilon}_{d_{p\ uncorr}}$ [%]	$\sigma_{d_{p\ uncorr}}$ [%]	$\bar{\varepsilon}_{d_{p\ corr}}$ [%]	$\sigma_{d_{p\ corr}}$ [%]	$\bar{\varepsilon}_{d_{p\ corr}}$ [µm]	$\sigma_{d_{p\ corr}}$ [µm]
10	76.6	11.4	1.1	5.1	0.1	0.5
15	65.1	4.4	0.3	2.1	0.0	0.3
20	59.1	4.5	0.0	0.7	0.0	0.1
25	52.6	5.2	0.0	0.0	0.0	0.0
30	46.9	5.6	0.0	0.0	0.0	0.0
35	41.5	5.0	0.3	1.5	0.1	0.5
40	38.0	4.6	0.0	0.0	0.0	0.0
45	34.3	4.1	0.0	0.0	0.0	0.0
50	31.5	3.6	0.0	0.0	0.0	0.0
55	28.9	3.3	0.0	0.0	0.0	0.0
60	26.8	2.8	0.0	0.4	0.0	0.2
70	22.9	2.2	0.0	0.0	0.0	0.0
80	20.1	1.8	0.0	0.0	0.0	0.0
90	18.1	1.4	0.0	0.0	0.0	0.0
100	16.4	1.2	0.0	0.0	0.0	0.0

5.2.5.1.2. Measurement Volume Thickness

The measurement volume thickness is fundamental for the determination of the particle mass flow rate (see **section 5.2.4**). In this section, the effect of the additional size correction on the measurement volume thickness is described.

The measurement volume thickness ($d_{GS\ min}$), was defined as the focus depth, in which particle / dot sizes could be properly detected and corrected with the help of the described additional size correction. Depending on the implemented optics, it can be described as a function of particle / dot diameter. Following the remark made in [38, 39], it is necessary to control if all dots within a defined measurement volume thickness are detected. To check if this was the case for $d_{GS\ min}$, the count efficiency (CE) is considered. The count efficiency is the ratio between detected dots of a specific true dot size and the number of dots of a specific true size on the calibration plate:

$$CE_{dp} = \frac{n_{p\ detected}}{n_{p\ calibration\ target}} \tag{5-14}$$

The count efficiency can only be calculated for the calibration dots data. It depends on the true dot size. The measurement volume thickness in which CE = 1 is named $d_{CE=1}$. The measurement volume thickness $d_{GS\ min}$ can be used as final shadowgraphy measurement volume thickness d_{shadow}, as long as the following condition is met:

$$d_{GS\ min} \leq d_{CE=1} \tag{5-15}$$

If the requirement of **eq. (5-15)** is not fulfilled, the parameter min GS offset has to be increased to reduce $d_{GS\ min}$. So, the final shadowgraphy measurement volume thickness d is defined as the minimum volume thickness, which is limited by the minimum GS and in which the count efficiency CE is 1. The count efficiency for the investigated z-positions and the final shadowgraphy detection parameters (see **Table 13**) are plotted in **Fig. 40**.

For some z-positions and calibration dot sizes, CE is larger than 1. This is an effect of particle detection at low BiThr values: Unfocussed shadows were split into multiple shadows, resulting in CE larger than 1. This split effect was excluded by considering $d_{CE=1}$, because it is the maximum continuous measurement volume thickness in which CE is always 1. Shadowgraphy measurement volume thicknesses for individual dot sizes are plotted in **Fig. 41**. The factor $d_{CE=1}$ is larger than $d_{GS\ min}$ for all calibration dot sizes. As a consequence, it is assumed that the count efficiency is always sufficiently high in $d_{GS\ min}$, which is used as final shadowgraphy measurement volume thickness d_{shadow} in the following. The general measurement volume thickness uncertainty is assumed to be 0.1 mm, which is equivalent to one step in z-direction in terms of the DOF calibration.

Similar to the additional size correction, the d_{shadow} determination was done individually for each camera and for 1x1.2 mm² sections of the shadowgraphy images.

The presented measurement volume thickness determination is valid as long as shadows of particles in supersonic flows behave similar to circular dots on a glass-target. A comparison between bubble-based and glass-target-based calibrations was made in [39], showing differences in the detected measurement volume thickness. In future studies, it has to be checked whether shadowgraphy's measurement volume thickness, measured by means of a glass target without flow, can be applied to the supersonic flow environment.

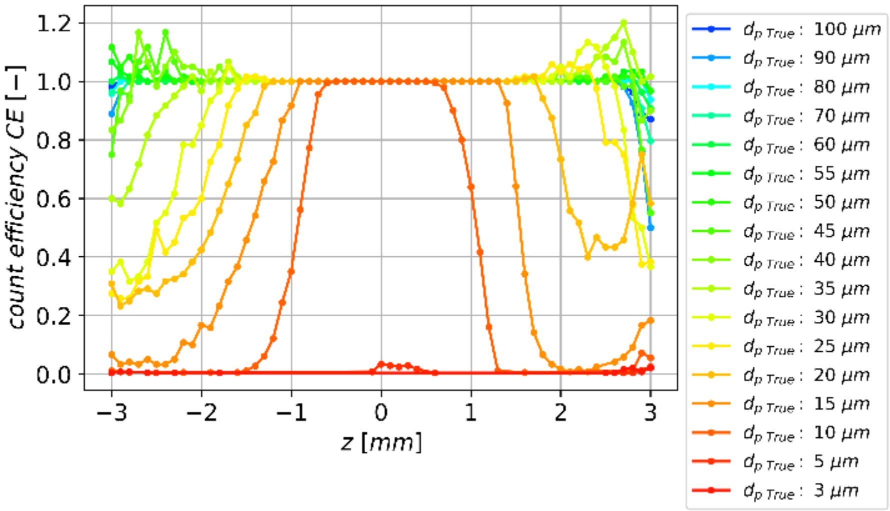

Fig. 40 Count efficiency vs. z-position, BiThr = 13 % and NorRad = 10 px, C1

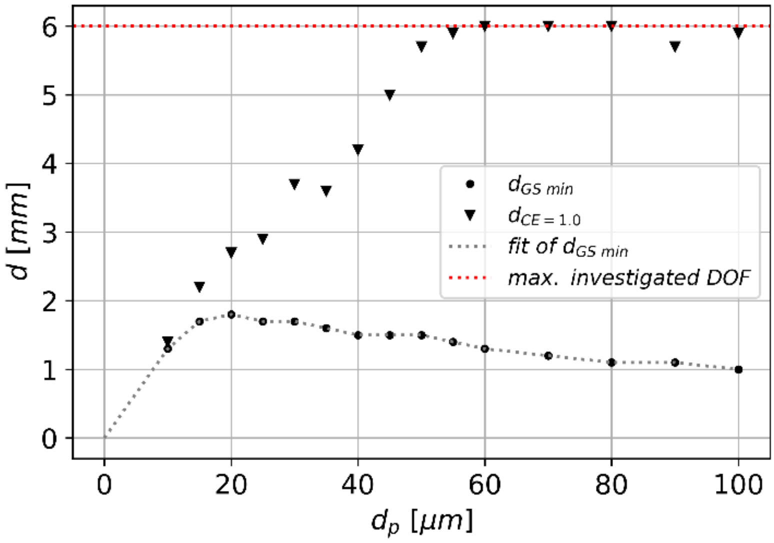

Fig. 41 Relation between $d_{GS\ min}$ and $d_{CE=1}$, depending on calibration dot size. $d_{CE=1}$ is always larger than $d_{GS\ min}$

5.2.5.1.3. Velocity Measurement

The shadow velocity was determined with the help of cross-correlation (see **section 3.3**): Two illumination pulses with the predefined Δt were used to generate two shadow images. The shadow displacement on these two images was measured. The ratio between displacement and time separation is the shadow velocity. The particle displacement measurement uncertainty $\Delta X'_{PIV\,Unc}$ was estimated for small MgO-PIV particles in **section 4.3.2**. It was 0.2 px for the shadowgraphy system.

5.2.5.1.4. Data Filtering

Additional filters were applied on the corrected shadowgraphy data, which are listed in **Table 15**. The theoretical velocity is the gas velocity at the nozzle exit, assuming one-dimensional isentropic gas dynamics. The minimum velocity filter in x-direction of 300 m/s as well as the velocity filter in y-direction were used to omit incorrectly assigned small and slow particle shadows for all test conditions. The x-direction velocity filter contains the strongest false vector deletion of small and slow 'particles' without affecting real vectors of larger particles.

Table 15 Overview of applied filters on shadowgraphy data

parameter	unit	filter
u (x-direction velocity)	m/s	300 to theoretical velocity
v (y-direction velocity)	m/s	-20 to 20
GS	%	min. GS to 100

5.2.5.2. PTV Approach

Another approach to measure particle mass flow rate is based on PTV. In the following, the general PTV data processing is described.

PTV images were processed with the help of LaVision DaVis FlowMaster software. A 'subtract-over-time' filter was applied for pre-processing, subtracting the time-average image from all other images. The vector-processing was split into two steps: First, regular PIV vector fields were achieved. Here, a multi-pass vector calculation with an initial interrogation window size of 96x96 px² and a final interrogation window size of 24x24 px² was used. The overlap was set to 50 %. In a second step, PTV vector data were calculated, based on the PIV vector fields (see **section 3.3.1**). The allowed particle size range was between 2 and 500 px, the correlation window size was set to 32 px. A variation in correlation window size resulted in negligible differences of the PTV data.

5.2.5.2.1. Velocity Measurement

PTV velocity uncertainty was calculated in the similar manner as described in **section 4.2.5**: PTV uncertainty was interpolated from PIV evaluations with an interrogation window size of 8x8 px for particles larger than 1 µm. This interrogation window size was a trade-off between the large particle image sizes (large interrogation window size) and the idea that each interrogation window should contain only one particle image (small interrogation window size due to high particle concentration). The relative PTV velocity uncertainty for larger Al_2O_3 particles depending on particle velocity is depicted in **Fig. 42**. Here, the mean velocity uncertainty over several velocity classes is illustrated. The data were taken across the entire nozzle exit of test A-32-2-akin (see **Table 12**).

The bars indicate the velocity uncertainty interquartile range (IQR). **Fig. 42** clearly shows that the lower the particle velocity (= the larger the particles, as shown in **section 5.3.1**), the higher the relative velocity uncertainty. The velocity uncertainty for large particles is much larger compared to those of the PIV-MgO material (see **section 4.3.2**).

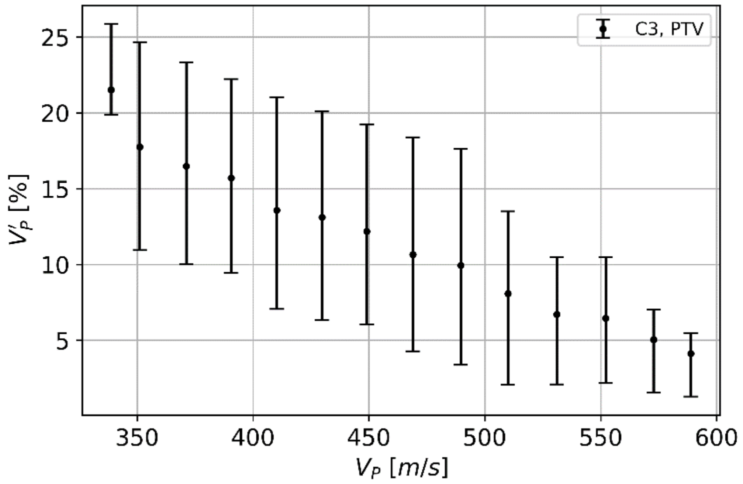

Fig. 42 Adapted PTV velocity uncertainty for different particle velocities across the entire nozzle exit, C3

5.2.5.2.2. Particle Size Determination

To achieve particle mass flow rates from PTV velocity data, the size of the particles and the size of the PTV measurement volume had to be estimated. In the following, the particle size determination in terms of the PTV measurement approach is described.

The investigated particles achieved lower velocities than the gas velocity, which is caused by their large inertia and the small size of the nozzle. Their final velocity depended on their size. Thus, a monotonical relation between d_p and V_p was defined, depending on flow conditions and the particle material. This relation is called particle velocity-size relation (VSR). It is based on the shadowgraphy data and is only applicable to the investigated flow setup. Assuming the validity of the velocity-size relation over the entire nozzle exit, PTV velocity data can be converted into size data:

$$d_{p\,PTV} = VSR(V_{p\,PTV}) \tag{5-16}$$

The particle size uncertainty for the PTV measurement approach is calculated as follows: The minimum and the maximum particle velocity for every individual particle is calculated considering the individual particle velocity uncertainty:

$$\begin{aligned} V_{p\,PTV\,max} &= V_{p\,PTV} + V'_{p\,PTV}, \\ V_{p\,PTV\,min} &= V_{p\,PTV} - V'_{p\,PTV} \end{aligned} \tag{5-17}$$

The minimum and the maximum particle velocity is converted with the VSR to a maximum and minimum particle size, respectively:

$$\begin{aligned} d_{p\ PTV} &= VSR\left(V_{p\ PTV}\right), \\ d_{p\ PTV\ max} &= VSR\left(V_{p\ PTV\ min}\right), \\ d_{p\ PTV\ min} &= VSR(V_{p\ PTV\ max}) \end{aligned} \tag{5-18}$$

The particle size error $\varepsilon_{dp\ PTV}$ is defined to be the maximum difference between $d_{p\ PTV\ max}$ or $d_{p\ PTV\ min}$ and $d_{p\ PTV}$:

$$\varepsilon_{dp\ PTV} = max\begin{pmatrix} d_{p\ PTV\ max} - d_{p\ PTV} \\ d_{p\ PTV} - d_{p\ PTV\ min} \end{pmatrix}, \tag{5-19}$$

This estimation of the particle size error of the PTV system is conservative and depends on the found velocity-size relation VSR. The steeper the gradient of the VSR, the smaller $\varepsilon_{dp\ PTV}$.

The IQR range of the PTV's particle size uncertainty in relation to the particle size is illustrated in **Fig. 43**. The size uncertainty is scaled to the detected particle size. The uncertainty is up to 200 % for particles smaller 25 µm, while it is approximately 60 % for particles larger than 40 µm.

The resulting PTV particle sizes and the respective uncertainties are discussed in **section 5.3.3** and **section 5.3.4.1**.

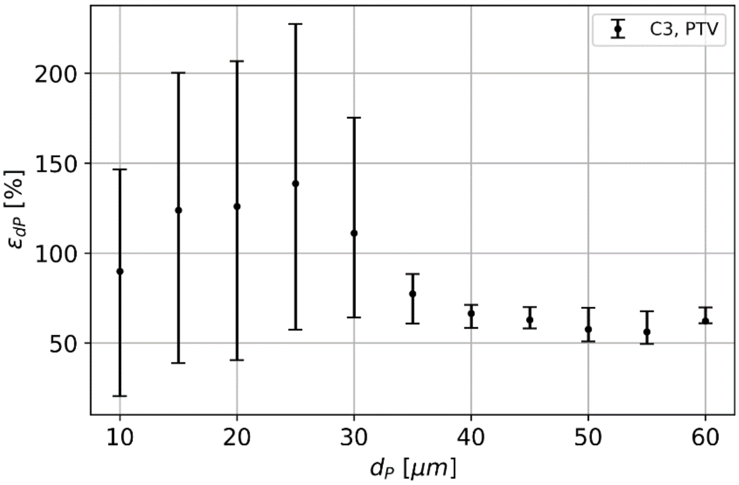

Fig. 43 PTV's particle size uncertainty vs. estimated particle size

5.2.5.2.3. Measurement Volume Thickness

The PTV measurement volume thickness (d_{PTV}) was assumed to be the light sheet thickness, since this was much smaller than the DOF of the PTV camera C3. In contrast to shadowgraphy, the d_{PTV} only depends on the y-position.

To measure the light sheet thickness accurately, a tilted calibration plate was moved through the focus-plane while the laser was switched on the lowest power level and the flow was turned off. Recordings were made with the C3 camera. The width of the laser reflections at different y-positions was measured, which was converted into the laser sheet thickness. This was done for the 'Master' (first) and 'Slave' (second) laser pulse. The uncertainty of the measurement volume thickness estimation was assumed to be 3 px, which were approximately 75 µm. The measured laser sheet thickness is plotted in **Fig. 44** for both laser pulses, namely 'Master' and 'Slave'. The sheet thickness increased from top to bottom, from approximately 0.25 mm to approximately 0.5 mm. The mean of both laser pulses is marked with a red dashed line. This mean is considered as PTV measurement volume thickness in the following. It was assumed that all particles were detected by PTV within its measurement volume.

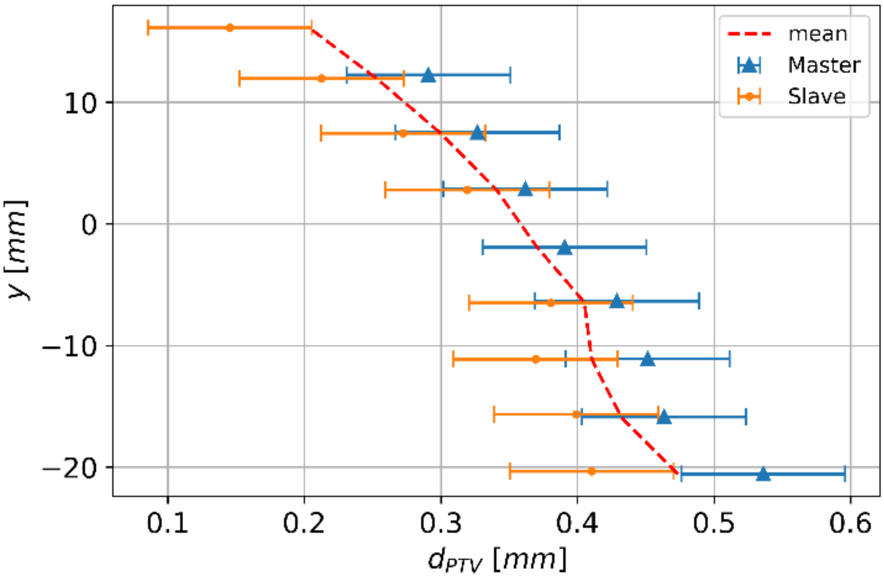

Fig. 44 PTV light sheet thickness for both laser pulses at different y-positions

5.2.5.2.4. Data Filtering

Several filters were applied onto the PTV data. These are listed in **Table 16**. All these filters were used to exclude false vectors. The limitation of the velocities components is identical to the shadowgraphy filtering (see **section 5.2.5.1.4**). The limitation of the correlation value is a recommendation given in [66]. The limitation of the particle size excluded single slow particles, whose size were derived to be unphysically large.

Table 16 Overview of applied PTV data filters

parameter	unit	filter
u (x-velocity component)	m/s	300 to theoretical velocity
v (y-velocity component)	m/s	-20 to 20
d_p	µm	0 to 60
correlation value	-	0.6 to 0.7

5.2.5.2.5. Mass Flow Rate Scaling

The resulting particle mass flow rate, based on PTV data, was calculated with the help of **eq. (5-4)** and is named $G_{p\ PTV}$. According to **eq. (5-9)**, a total particle mass $M_{p\ PTV}$ was calculated:

$$M_{p\ PTV} = \pi * t_{meas} \int_{\frac{-d_{nozzle}}{2}}^{\frac{d_{nozzle}}{2}} \overline{G_{p\ PTV}}(y) * |y| * \, dy \tag{5-20}$$

If the calculated $M_{p\ PTV}$ did not coincide with $M_{p\ nozzle}$, the $G_{p\ PTV}$ value was also scaled to fit to $M_{p\ nozzle}$. The resulting scaled particle mass flow rate is named $G_{p\ PTV\ scaled}$. The scaling was done with the following formulation:

$$\overline{G_{p\ PTV\ scaled}}(y) = \frac{M_{p\ nozzle}}{M_{p\ PTV}} * \overline{G_{p\ PTV}}(y) \tag{5-21}$$

Differences between $G_{p\ PTV}$ and $G_{p\ PTV\ scaled}$ are discussed in **section 5.3.4.2**.

5.2.5.3. Scattered Light Intensity Approach

Another approach for determining the spatially resolved particle mass flow rate profile used scattered light intensity profiles across the nozzle exit. This method was presented in [13] and was also included in [15]. Following the square-law dependence between scattered light of particles and their diameter [75] and **eq. (5-4)**, it was assumed that the following relationship between scattered light intensity and the qualitative particle mass flow rate ($G_{p\ scatter\ qual.}$) is valid:

$$scattered\ light\ intensity^{1.5} \sim {d_p}^3 \sim G_{p\ scatter\ qual.} \tag{5-22}$$

The scattered light signal was taken from the PTV camera C3. Only images were considered, which were recorded during the measurement time t_{meas}. Afterwards, the average from all of these images was subtracted from every image. The subtracted images were summed up and the mean intensity for every y-position was built. According to **eq. (5-9)**, a total particle mass $M_{p\ scatter\ qual.}$ was calculated:

$$M_{p\ scatter\ qual.} = \pi * t_{meas} \int_{\frac{-d_{nozzle}}{2}}^{\frac{d_{nozzle}}{2}} \overline{G_{p\ scatter\ qual.}}(y) * |y| * \, dy \tag{5-23}$$

Similar to PTV, the $G_{p\ scatter\ qual.}$ value was scaled to fit to $M_{p\ nozzle}$. The resulting particle mass flow rate is named $G_{p\ scatter}$. The scaling was done with the following formulation:

$$\overline{G_{p\ scatter}}(y) = \frac{M_{p\ nozzle}}{M_{p\ scatter\ qual.}} * \overline{G_{p\ scatter\ qual.}}(y) \tag{5-24}$$

5.3. Analysis

As mentioned in **section 5.1**, the first analysis is about the particle density. As a first approach, measured particle velocities at the nozzle exit were compared to one-dimensional isentropic calculations. Then, pycnometer measurements were analysed. Particle size distributions are compared to those of commercial measurement devices to estimate the validity of the presented measurement approaches. Finally, G_p uncertainties, spatially resolved distribution profiles, and quantitative values are discussed.

5.3.1. Particle Velocities at the Nozzle Exit

Particle density (ρ_p) is one key parameter to describe particle mass flow rate accurately (see **eq. (5-4)**). The initial idea was to determine particle density by comparing measured and calculated particle velocities at the nozzle exit. This idea followed a procedure similar to the one described in [76]. In that work, particle density was adapted to fit calculated particle velocities to experimentally measured data.

In the following, experimental data of the shadowgraphy approach were considered. Particle motion was computed with the following equation, considering only dominating drag forces [77]:

$$m_p * \frac{dV_p}{dt} = \frac{\pi}{8} * {d_p}^2 * \rho_g * C_D * \left(V_g - V_p\right) * \left|V_g - V_p\right| \qquad (5\text{-}25)$$

Here, m_p is the mass of the particle, V_g is the gas velocity, and C_D is the particle drag coefficient. Particles are assumed to be spherical in **eq. (5-25)**. A forth order Range-Kutta scheme was used for solving this ordinary differential equation. The applied procedure is one-way-coupled, meaning that only the surrounding fluid affects the particle motion, but not vice-versa.

Three correlations to describe particle drag were taken into account, namely Henderson [78], Parmar [79], and Loth [80] drag correlation. The explicit drag formulations are given in the **Appendix**.

To solve **eq. (5-25)**, the local flow states, e.g. velocity or density, were required. These parameters were calculated with the help of the one-dimensional isentropic gas equations, local Mach numbers, as well as experimental determined p_0 and T_0. The local Mach number on the symmetry axis of the convergent-divergent nozzle was taken for computation. Three Mach number modelling approaches were compared: isentropic Mach number calculation based on the nozzle expansion ratio (1D), methods of characteristics (MOC) and an axisymmetric flow calculation with the DLR Tau code [81] without viscous effects. The resulting Mach number profiles, as well as the radius contour of the nozzle can be found in **Fig. 45**. The Mach number profile based on TAU shows agreement with the supersonic solution of MOC. Because the TAU simulation is similar to MOC and contained also data in the subsonic regime, its Mach profile was used for particle motion calculation. The simulations started at the beginning of the convergent part of the nozzle. It was assumed that the initial particle velocity was in equilibrium with the surrounding flow for every particle size, so

$V_{p,x0}$ = 24.39 m/s. The choice of the initial particle velocity has only minor impact on the resulting particle velocity at the nozzle exit.

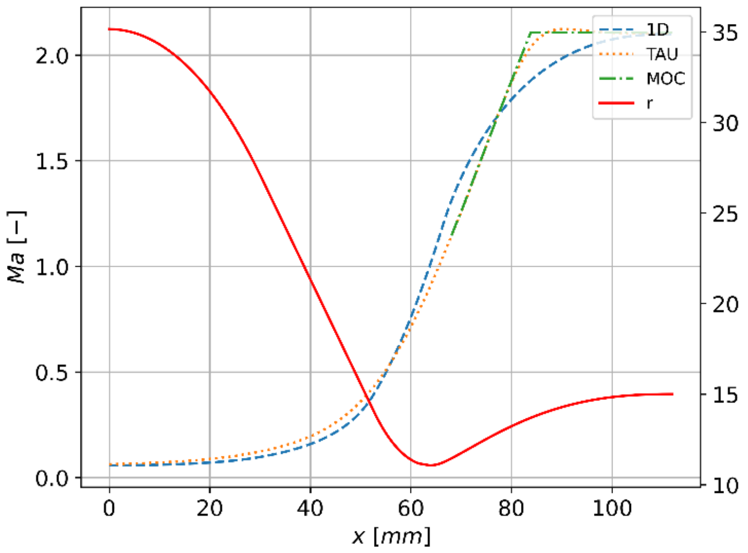

Fig. 45 Nozzle contour and Mach Number contours along the nozzle axis, calculated with different methods

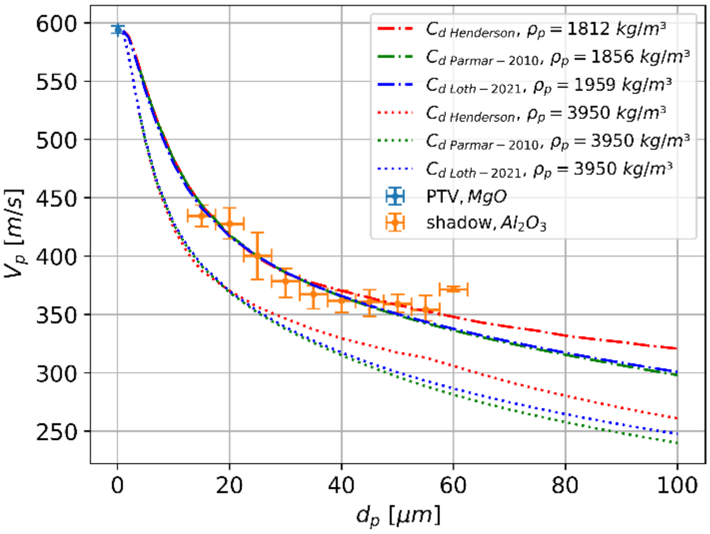

Fig. 46 Particle velocity vs. particle size 2.5 mm downstream of the nozzle exit, assuming different drag models and particle densities

The measured and calculated relations between particle velocity and particle size for the reference flow condition are illustrated in **Fig. 46**.

The shown experimental data are taken from the analysis described in [15], in which the shadowgraphy resolution was not as high as described in the previous subsections. The experimental data sets of that study greatly coincided with those of [16] and the presented data. Since the velocity-size relation was investigated and simulated in detail in the study with lower shadowgraphy resolution, the respective experimental data is shown in **Fig. 46**.

The orange markers belong to experimental data gained with shadowgraphy. Here, only particles with a detected centricity larger than 90 % were included. Centricity is the ratio between short and long axis of the detected shadow. It was assumed that a high centricity value result in a high sphericity of the particle. With this constraint, particles from ten runs were summed up to be 2567. The size error bars correspond to the 'rainbow' stripe width of the shadowgraphy's additional size correction (like in **Fig. 39**); the velocity error bars represent the IQR of particle velocity for the respective size classes. The light blue marker indicates PTV velocity measurements with tracer particles made of PIV-MgO, whose size is set to be 0.2 µm.

The dotted lines belong to calculations with different drag models and an Al_2O_3 pure substance density of $\rho_p = 3950\ kg/m^3$. The 'kink' in the Henderson relation is caused by the change of subsonic to transonic formulation for particles larger than 55 µm at the nozzle exit. **Fig. 46** shows that results from all three drag models did not agree very well with experimental data, if the Al_2O_3 pure substance density was used.

As a consequence, the calculated relations were fitted to the experimental data by adapting ρ_p, like it was done in [76]. The relations with adapted ρ_p are indicated with the dash-dotted lines; the red, green, and blue lines belong to the Henderson, Parmar, and Loth drag model, respectively.

The optimized particle density was less than a half of 3950 kg/m³ for all three drag correlations (see legend of **Fig. 46**). The adaption of ρ_p led to good agreement of experiment and theory. It must be noted that the optimized particle density depends on the selected particles and the chosen drag model.

Although a reduction of the particle density is possible due to e.g. agglomerations, there is not enough evidence for this drastic reduction by half. An experimental validation of particle density was required, as it is described in **section 5.3.2**. Since the measured particle density of Al_2O_3 particle is close to the nominal value 3950 kg/m³ (see **section 5.3.1**), there could be only two reasons for this discrepancy in particle velocity comparison: The measurement of particle size and particle velocity is incorrect, or the one-dimensional calculations and the implemented drag coefficients were incorrect or did not fit to the particles. Since the particle velocity measurement error is determined in **section 4.3.2** to be significantly smaller and because the measured particle size distribution is in agreement to independent particle size measurements (see **section 5.3.3**), the one-dimensional particle velocity calculations seem to be the reason for the detected discrepancy.

This discrepancy was also reported in [4], without any comment about the analytical model. In a recent study [14], simulated drag coefficients were lower than its experimentally determined counterparts for particles in two phase flows. The authors assumed that the differences are likely due to differences in particle surface state and the shape of the particles. Also in [13] it was pointed out that particle shape could lead to differences between measured and numerically calculated particle velocities.

Also recent results of a cooperation with NASA Ames indicate that the main driver for the velocity discrepancy is the consideration of particle shape in the drag formulations. It seems that the consideration of particle shadow centricity in the experimental data is not sufficient to exclude particle shape effects. This can be reasoned by the fact, that the detected shadow is only a two-dimensional projection of the three-dimensional particle. However, since here only the particle density is of fundamental importance for particle mass flow determination, the detailed second particle velocity comparison with the advanced drag model calculation results was not performed in this work.

5.3.2. Particle Density Analysis

As it was shown in **section 5.3.1**, it was not possible to derive particle density from particle velocity measurements accurately. Therefore, a reliable technique was used to determine particle density experimentally. The use of a 100 ml-large pycnometer was chosen, which was independent of tests in the GBK facility. A sartorius ED6202s scale with a maximum capacity of 6200 g and a display accuracy of 0.01 g was used for scaling. The pycnometer was filled with distilled water at approximately 290 K. The assumed water density was 998.8 kg/m³. The particle density of MgO was additionally measured with the help of paraffin oil, having a density of 845.9 kg/m³. This was done to exclude any reaction processes of MgO and H_2O to magnesium hydroxide, $Mg(OH)_2$. The particle material and the liquid were shaken until no air bubbles within the pycnometer were visible any more. Each material density was measured three times with water.

These measurements results are summarized in **Table 17**. Reference particle densities for Al_2O_3, MgO and SiO_2 were taken from [14] and [13], [82], and [2], respectively. The given difference is the difference between reference value and the mean value of the three pycnometer measurements.

Table 17 Pycnometer measurement results

parameter	unit	Al_2O_3	MgO	SiO_2
measured ρ_p, run 1, H_2O	kg/m³	3846	3165	2630
measured ρ_p, run 2, H_2O	kg/m³	3907	3056	2640
measured ρ_p, run 3, H_2O	kg/m³	3901	3182	2638
measured ρ_p, run 4, paraffin oil	kg/m³	-	3091	-
measured ρ_p, run 5, paraffin oil	kg/m³	-	3174	-
measured ρ_p, mean	**kg/m³**	**3884**	**3133**	**2636**
reference ρ_p	kg/m³	3950	3580	2650
difference	**%**	**-1.7**	**-12.5**	**-0.5**

The pycnometer results indicated that the measured density ρ_p of Al_2O_3 and SiO_2 particles agreed to reference values from literatures, while the measured MgO density was 12.5 % lower. This significant decrease can be caused, first, by a partial chemical reaction of MgO with humidity, resulting in $Mg(OH)_2$, whose density is around 2380 kg/m³, and second, by contamination during the additional sieving process. A reaction of MgO with water within the pycnometer during the measurement could be excluded, because no difference in MgO density between water-filled pycnometer measurements and paraffin-oil-filled pycnometer measurements was observed. Another pycnometer measurement with smaller-sized MgO particles were made, which were not additionally sieved. The resulting particle density was even lower than 3133 kg/m³, which seems to exclude contamination as the only reason for the low density. As a consequence, careful attention must be given to the reactivity of particle material and its storage in future studies.

For the following analyses, the mean measured values are taken for particle mass flow rate calculations. A particle density uncertainty of 38 kg/m³, 77 kg/m³, and 6 kg/m³ for Al_2O_3, MgO, and SiO_2 particles are assumed, respectively. These uncertainties correspond to the largest difference between measured and mean densities.

5.3.3. Particle Size Distributions

To start with a simpler validation of the implemented measurement approaches, particle size distributions are compared to reference measurements in a first step. This can be reasoned by the fact, that the determination of particle size is less complicated than the determination of particle mass flow rate.

The reference measurements were conducted independently of the GBK facility or flow conditions. These reference data were achieved with a dynamic image analysis device ‘PartAn SI’ of Microtrac. The Al_2O_3 size distribution of test run A-32-1-akin is shown in **Fig. 47**, while the MgO size distribution of test run M-32-1-akin is illustrated in **Fig. 48**. Although there is no reference size distribution of SiO_2 particles available, the shadowgraphy and PTV size distributions of test run S-32-1-akin are given in **Fig. 49**. The size bins correspond to shadowgraphy uncertainty, so their width is 2.5 µm. Since the variable measurement volume thickness of shadowgraphy has decisive influence on particle size distribution visualization, it was considered in the following plots, indicated with the addition ‘DOF corr’.

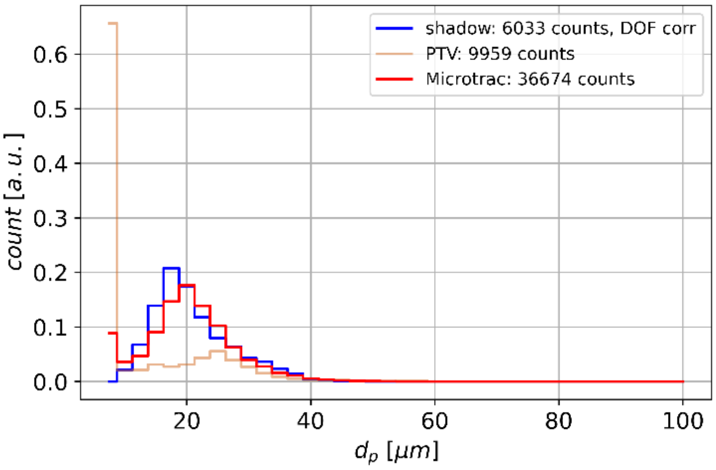

Fig. 47 Particle size distribution, Al_2O_3, run A-32-1-akin

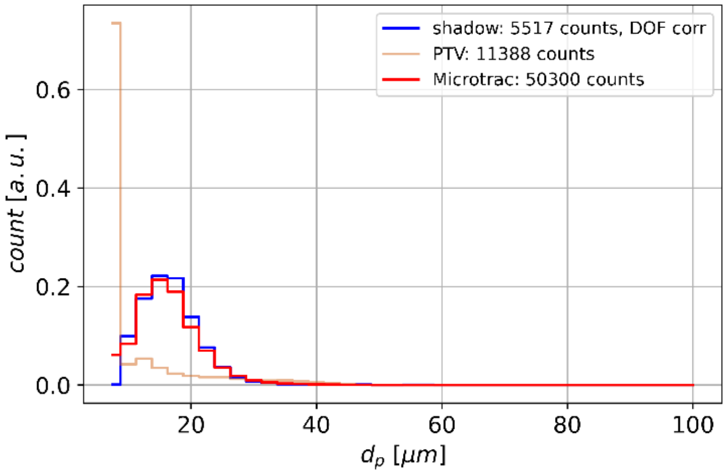

Fig. 48 Particle size distribution, MgO, run M-32-1-akin

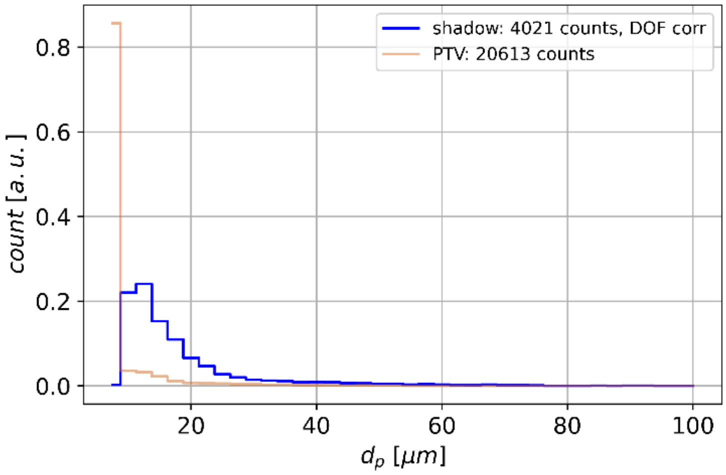

Fig. 49 Particle size distribution, SiO_2, run S-32-1-akin

The presented shadowgraphy procedure and the additional size correction resulted in a good agreement of particle size distribution of Al_2O_3 and MgO particles, compared to reference measurements by Microtrac. Shadowgraphy detected slightly more Al_2O_3 particles in the range of 15 to 17.5 µm. It can be concluded that the implemented additional size correction of the shadowgraphy approach works correct.

Because particle agglomeration effects in the reference measurements were minimized, it is concluded that Al_2O_3 particles and MgO particle did not show significant agglomeration within the GBK flow. The SiO_2 particle size distribution tends to smaller particles than those of MgO and Al_2O_3. Some SiO_2 particles up to 80 µm were detected. This agglomeration behaviour of SiO_2 particles was also described in [83]. In future studies, reference size distribution measurements should clarify if SiO_2 particles were agglomerated.

PTV-based size distributions were in poor agreement with the Microtrac reference size distributions for all of the investigated flow conditions. As expected, most of PTV's detected particles were in the size range of 0 to 7.5 µm for which PTV was originally developed. It is assumed that the large velocity uncertainty is responsible for that poor agreement (see **section 5.2.5.2.2**).

5.3.4. Particle Mass Flow Rate

After comparing particle size distributions in the previous section, particle mass flow rates are investigated in the following. Therefore, not only the particle size, but also the particle velocity, particle density, and the measurement volume have to be considered. First, a general uncertainty analysis of particle mass flow rate determination is made, which is required for the following analyses. Then, spatially-resolved particle mass flow rate distribution profiles across the nozzle exit are investigated. In the end, quantitative particle mass flow rate values of the flow center are discussed.

5.3.4.1. Uncertainty

Linear error propagation theory was implemented generally to determine uncertainties. The python implementation of the uncertainty analysis included a python package by [84]. In terms of the shadowgraphy and PTV approach, particle mass flow rate was calculated with **eq. (5-4)**. Hence, particle mass flow rate uncertainty depended on the uncertainties of particle number, velocity, size, density, and the size of the measurement volume. It was assumed that particle mass flow rate uncertainty of the scattered light intensity approach only depends on $M_{p\ nozzle}$ uncertainty. This was also the case for $G_{p\ PTV\ scaled}$.

Apart from that, it was checked how the resulting shadowgraphy G_p is affected by single DaVis shadowgraphy detection parameters, namely BiThr and NorRad. Therefore, a parameter variation of BiThr and NorRad was performed. A change of BiThr required also the adaption of the min GS offset to account for a measurement volume thickness in which CE is 1 (see **section 5.2.5.1**).

In the following, shadowgraphy data from the test run A-32-1-akin (see **Table 12**) were taken to determine the G_p uncertainty of the presented shadowgraphy approach, including the additional size correction and the d_{shadow} determination. The parameter setting as well as the resulting mean G_p value and its uncertainty are given in **Table 18**.

An increase of NorRad results in a decreased G_p, which can be explained by stronger smearing effects, so that more particles remain undetected. G_p increases if BiThr and minimum GS offset are also increased. This behaviour can be reasoned by a general trend of a measurement volume thickness decrease with increasing BiThr. With increasing BiThr, the volume thickness decreases faster than the number of detected particles.

The average of all G_p mean values is approximately 6.1 kg/m²s, close to the result with the setting NorRad = 10 px and BiThr = 13 %. The G_p uncertainty for each parameter setting is approximately 0.04 kg/m²s, namely up to 1 %. The maximum difference between G_p mean values and their average value is approximately 30 %. The percentage of particles smaller than $d_{p\ min,\ full}$ = 10 µm, which are the 'invisible' particles for shadowgraphy, on the total G_p is less than 2 % for Al_2O_3 particles. Since the variation of G_p mean values is significantly larger than the respective G_p uncertainties, an overall uncertainty of 30 % for shadowgraphy's G_p determination of all tests was assumed in the following. The parameter setting of NorRad = 10 px and BiThr = 13 % was chosen for the following analysis.

Table 18 Parameter variation effects on shadowgraphy's G_p. The parameter variation has more influence on G_p than the estimated uncertainty based on individual particle parameter uncertainties

NorRad	**BiThr**	**min. GS offset**	**G_p**
[px]	[%]	[%]	[kg/m²s]
10	13	12	6.19±0.04
5	13	12	6.89±0.04
15	13	12	5.69±0.04
25	13	12	5.21±0.03
10	10	12	4.28±0.03
10	20	14	7.24±0.05
10	30	20	7.02±0.04

The particle mass flow rate uncertainties of the three measurement approaches are summarized in **Table 19**. While shadowgraphy's uncertainty was set to 30 %, the uncertainty of $G_{p\ \mathrm{PTV}}$, $G_{p\ \mathrm{scattered}}$, and $G_{p\ \mathrm{PTV\ scaled}}$ varied for each test run. As a consequence, not only the mean, but also the corresponding interquartile ranges IQR of the respective particle mass flow rate uncertainties are listed.

Table 19 Relative particle mass flow rate uncertainties of all measurement approaches

parameter	**unit**	**mean (IQR) uncertainty**
$G_{p\ \mathrm{shadow}}$	%	30
$G_{p\ \mathrm{PTV}}$	%	76 (40 – 100)
$G_{p\ \mathrm{scattered}}$ / $G_{p\ \mathrm{PTV\ scaled}}$	%	28 (11 – 37)

While the particle mass flow rate uncertainty of shadowgraphy, the scaled scattered light intensity approach, and the scaled PTV approach are comparable, the unscaled PTV approach uncertainty is more than twice as high. Considering only these values, it can be concluded that the PTV approach is not accurate enough to measure particle mass flow rates. The significant PTV uncertainty is based

on velocity uncertainties up to 25 % (see **section 5.2.5.2.1**), which are increased to particle size uncertainties up to 200 % (see **section 5.2.5.2.2**) by the use of the particle velocity-size relation conversion.
The general PTV approach uncertainty has to be decreased to conclude if the quantitative PTV approach is generally feasible. This uncertainty can be significantly decreased with two strategies: increasing the particle displacement of the PTV recordings, and decreasing saturation effects caused by large particles. The latter was done with the help of a laser light intensity reduction, resulting in moderate success. As a conclusion, increasing the particle displacement from the current value of 5 to 10 px seems to be the best way to decrease PTV uncertainty. Since PTV and shadowgraphy used the same illumination source, a simultaneous measurement could be quite challenging with this setup, though.

5.3.4.2. Profiles at the Nozzle Exit

The four particle mass flow rate profiles based on the three measurement approaches are compared for each particle material and for the reference flow condition. These profiles are illustrated in **Fig. 50**, **Fig. 51**, and **Fig. 52** for Al_2O_3, MgO, and SiO_2 particles, respectively. Solid, dotted, and dash-dotted lines are representing the mean G_p values, while the transparent areas illustrate the respective measurement uncertainty (see **section 5.3.4.1**). Shadowgraphy results are colored red, PTV data are colored blue, scaled PTV data are colored golden and scattered light intensity data are colored green.

The general qualitative particle mass flow rate distributions of all particles are similar, considering the scaled PTV approach or the scaled scattered light intensity approach (see **Fig. 50**, **Fig. 51**, and **Fig. 52**): High G_p values are reached in a core flow, while it is significantly lower in the outer areas. The size of the core flow is approximately the size of the nozzle throat, although it varies slightly with the investigated particle material. It ranges from y = -7 to 7 mm for Al_2O_3 particles, from approximately y = -9 to 9 mm for MgO particles, and up to y = -12 to 12 mm for SiO_2 particles. This is caused by the particle inertia, which is driven by particle size and particle density [13, 15]. The larger particle inertia, the smaller the core flow. G_p distributions of Al_2O_3 and MgO particles have high extrema at the core flow edges. This phenomenon was already observed in [15]. Assuming that particles are homogeneously distributed within the mixing chamber, it seems that high inertia particles are accumulating along the convergent nozzle wall until they reach the nozzle throat, which is 22.13 mm in diameter. Up to here, they have been accelerated towards the flow center due to the convergent nozzle profile shape. Behind this point, they are not spread in radial direction again, leading to an accumulation of particles on y-positions slightly closer to the symmetry axis than the nozzle throat radius. This observed phenomenon could be also a consequence of aerodynamic focussing in supersonic nozzles, which was already numerically demonstrated for smaller particle sizes [85]. The G_p distribution of SiO_2 has no extrema at the core flow edges, and the scattered light intensity approach measured a significant larger core flow than the scaled PTV approach for these particles. This behaviour can be explained by much smaller SiO_2 particle inertia, sizes and lower particle densities.

In general, all measurement approaches measured an almost homogeneous G_p distribution in the measurement y-range of shadowgraphy. As a result, it is concluded that averaging the G_p values in the y-range between - 2.4 and 2.4 mm to compare quantitative G_p values is feasible in the following.

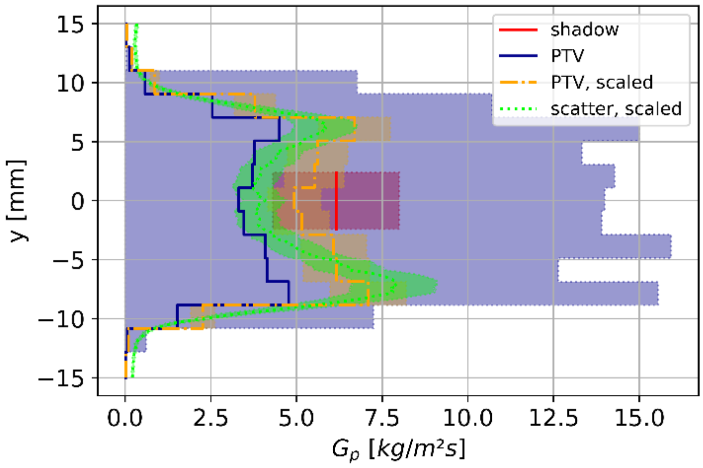

Fig. 50 Particle mass flow rate profiles, run A-32-1-akin, p_0 = 0.952 MPa, T_0 = 374.5 K, Al_2O_3

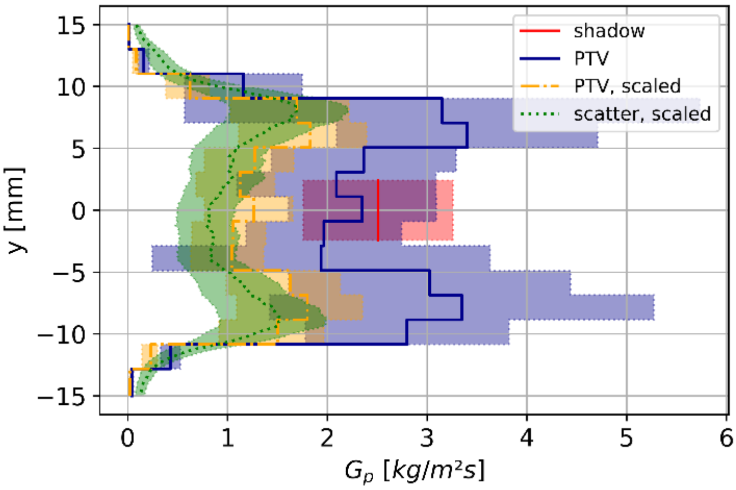

Fig. 51 Particle mass flow rate profiles, run M-32-1-akin, p_0 = 0.950 MPa, T_0 = 373.5 K, MgO

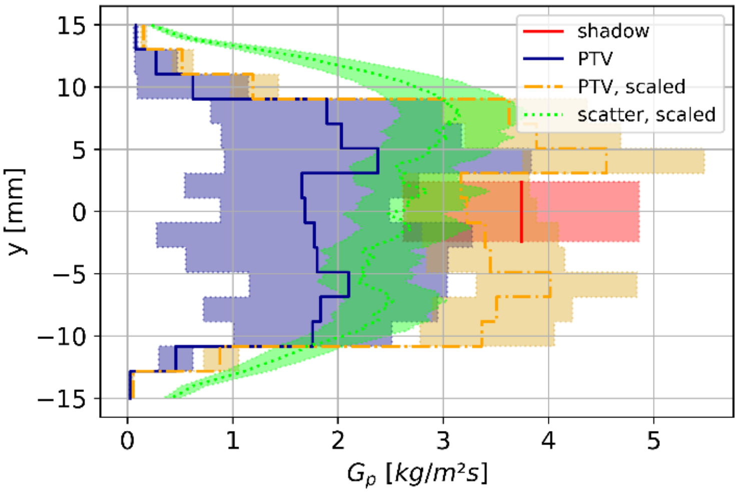

Fig. 52 Particle mass flow rate profiles, run S-32-1-akin, p_0 = 0.952 MPa, T_0 = 374.0 K, SiO_2

5.3.4.3. Quantitative Comparison

To compare the resulting quantitative particle mass flow rates for all investigated flow conditions and particle materials, the particle mass flow rates were only considered and averaged in the y-range between -2.4 and 2.4 mm. This y-range correspond to the shadowgraphy's FOV.

In literature, simple dust catcher probes were used for reference purposes. While simple dust catcher probes suffered from collecting particles in preliminary tests in the GBK facility, the results of the scaled scattered light intensity approach were used for referencing. This is reasoned by the fact that this technique was already used in a similar manner in [13]. Generally, an improvement of dust catcher probes for the use in the GBK facility is recommended in future studies, to have reference particle mass flow rates like in [10, 12].

The comparisons are illustrated in **Fig. 53**, **Fig. 54**, and **Fig. 55**. The colors represent the selected particle material. Linear fits were calculated and plotted as dashed lines for the visualization of a general behaviour between the respective measurement approaches. A unity line with unitary angular coefficient is also shown for better orientation.

The quantitative PTV approach resulted not only in a poor agreement of the particle size distribution (see **Fig. 47** to **Fig. 49** in **section 5.3.3**), but also the particle mass flow rates showed large uncertainties of up to 100 %, preventing useful interpretation of the results (see **Fig. 54** and **section 5.3.4.1**).

The scaling of the PTV profile to the total mass of seeded particles resulted in approximately 12 % higher particle mass flow rates, compared to those of the scaled scattered light intensity (see **Fig. 55**). The similarity of G_p of both scaled approaches can be explained by the fact that a similar qualitative G_p profile at the nozzle exit was derived by both approaches and that these profiles were scaled to $M_{p\,\mathrm{nozzle}}$ in the same way. Both scaled approaches have a G_p uncertainty of approximately 28 % (IQR 11 – 37 %) which is dominated by the uncertainty of $M_{p\,\mathrm{nozzle}}$. As expected, the larger the $M_{p\,\mathrm{nozzle}}$, the lower its relative uncertainty. In future, it seems to be advisable to increase the total mass of seeded particles by increasing particle mass flow rate or by increasing measurement time.

Shadowgraphy's G_p is approximately 58 % higher than those of the scaled scattered light intensity (see **Fig. 53**). Assuming that the latter one is correct and considering the fact that shadowgraphy measured the particle size distribution and velocity properly, the main driver for the increased G_p could be an underestimated measurement volume thickness d_{shadow}. However, in the study of [39], it is proposed that a DOF calibration with the help of a glass-target tends to an overestimated d_{shadow}. Furthermore, the consideration of the determined measurement volume thicknesses in particle size distribution comparisons led to feasible size distributions (see **Fig. 47** to **Fig. 49**), which allows assuming that the relative measured measurement volume thicknesses are correct.

On the other hand, it is also feasible that shadowgraphy's G_p is correct and that the scaled scattered light intensity approach and the scaled PTV approach are underestimating G_p. This can be true if the assumption of the semi-axisymmetric flow is not appropriate. Taking the single particle injection point within the mixing chamber into account, particles can accumulate on the x-y plane. This fact would increase shadowgraphy's G_p, but not the G_p values of the scaled scattered light intensity and the scaled PTV data, because these are scaled to the total particle mass. To close this gap of information, it has to be shown in future studies whether the particle mass flow rate distribution is axisymmetric or semi-axisymmetric. In any case, the shadowgraphy's G_p values are considered in the following analyses.

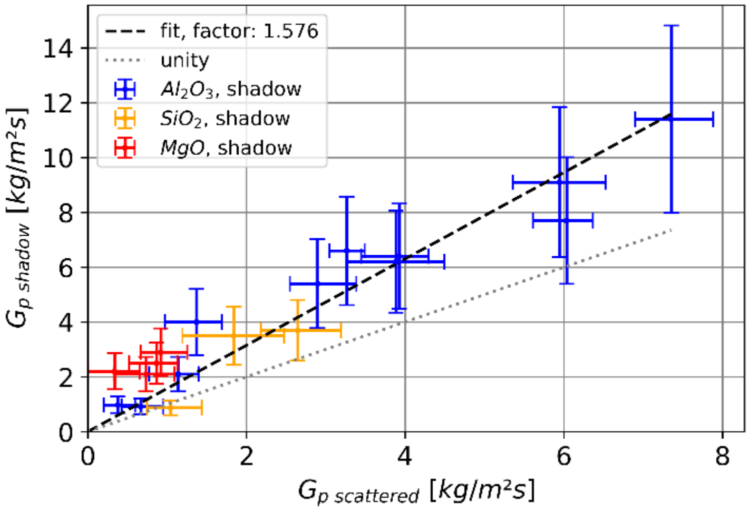

Fig. 53 Comparison of G_p in the y-range of -2.4 to 2.4 mm, measured with the scattered light intensity approach and shadowgraphy

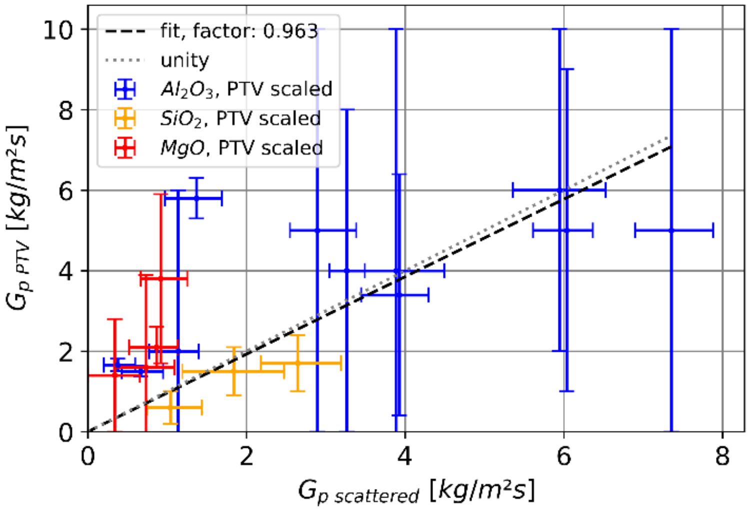

Fig. 54 Comparison of G_p in the y-range of -2.4 to 2.4 mm, measured with the scattered light intensity approach and the PTV approach

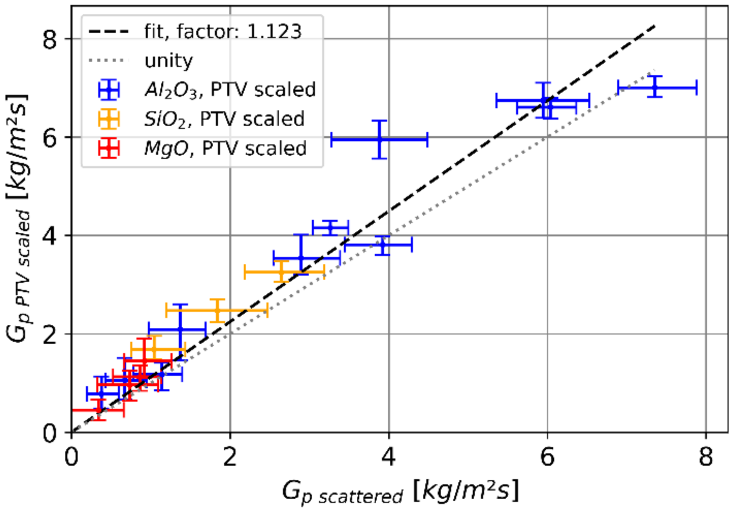

Fig. 55 Comparison of G_p in the y-range of -2.4 to 2.4 mm, measured with the scattered light intensity approach and the scaled PTV approach

5.4. Conclusion

In this section, three different approaches were established and compared to determine particle mass flow rate in supersonic flows. In terms of shadowgraphy, a new complex correction procedure was implemented, correcting out-of-focus effects of particles down to 10 µm and considering the count efficiency of the particle detection algorithm for the first time. Up to now, there is no other study in which particle mass flow rates were determined quantitatively with the help of a simultaneous and individual determination of particle number density, particle size, and -velocity in supersonic flows. The developed shadowgraphy approach significantly increases the validity of particle mass flow rate measurements, since it considers individual particle characteristics, which was not the case in heating augmentation literature so far.

The results of this section can be summarized as follows:

- one-way coupled simulations underestimated particle velocities at the nozzle exit. The unconsidered particle shape is possibly the main driver for these discrepancies
- pycnometer measurements resulted in an approximately 12.5 % lower MgO particle density, which can be caused by a chemical reaction of MgO with humidity to the significant lighter $Mg(OH)_2$
- shadowgraphy's size distributions of Al_2O_3 and MgO particles showed a good agreement with reference data, while SiO_2 particles seemed to agglomerate
- shadowgraphy's particle mass flow rate uncertainty of up to 30 % is dominated by the DaVis ParticleMaster software parameter variation
- the particle mass flow rate uncertainty of the scaled PTV and the scaled scattered light intensity approaches are in the range of 11 to 38 %, while it is in the range of 40 to 100 % for the unscaled PTV approach
- the particle mass flow rate is concentrated in a core flow, whose size depends on the nozzle throat size and on particle inertia
- the qualitative particle mass flow rate profile of the PTV approach and the scaled scattered light approach are similar for Al_2O_3 and MgO particles
- the scaled PTV approach detected only 12 % higher particle mass flow rates in average than the scaled scattered light intensity approach, which can be explained by the same scaling
- shadowgraphy detected 58 % higher particle mass flow rates in average than the scaled scattered light intensity approach, which can be caused by particle accumulation along the shadowgraphy measurement plane
- the measurement of particle mass flow rate with the shadowgraphy approach seems to be feasible for the following heating augmentation analyses

This section showed that shadowgraphy and the developed additional size correction led to valid particle size distributions and to reasonable particle mass flow rates. This approach was used in the following section to measure kinetic energy fluxes of particles.

6. Particle-Induced Heating Augmentation

6.1. Purposes & Structure

The experimental data base of particle-induced heating augmentation is limited. There is only a limited number of experimentally determined a_{kin} coefficients for a limited number of materials (see **Table 2**). Furthermore, these a_{kin} coefficients were determined with the help of particle mass flow rates, which are based on significant assumptions (see **section 1**). An extension of experimentally determined a_{kin} coefficients in supersonic particle-laden flows is of high importance.

This section presents new experiments concerning the determination of the a_{kin} coefficient. Therefore, the measurement of the stagnation point heat flux is required (see e.g. **eq. (6-9)**). In a first step, the stagnation point heat flux measurements in particle-free flows are validated by a comparison with the well-known stagnation point heat flux approximation by Fay and Riddell [86]. With the help of highly-resolved shadowgraphy (see **section 5**), particle kinetic energy fluxes are measured, considering individual size and velocity of both, incident and rebounded particles. As a novum, it is investigated how the kinetic energy flux of incident particles is affected by particle deceleration within the shock layer. The temporally-resolved kinetic energy flux of rebounded particles $\dot{e}_{kin\,reb}$ is considered in the analysis of the accommodation coefficient a_{kin} for the first time. Since differences in the a_{kin} coefficient for elastic or erosive particle reflection environments are predicted in literature (see **section 2.1.2**), the reflection mode of the investigated flow conditions is derived with **eq. (2-2)**. The measured a_{kin} coefficients are compared to measurements and predictions from literature.

With the help of the measured a_{kin} coefficients and **eq. (3-1)**, the convective heat flux increase is derived from the measured kinetic energy flux and the measured stagnation point heat flux in particle-laden flows. Since public modelling approaches of the convective heat flux increase [7, 9, 10] are limited to flow and particle regimes which do not coincide with the regimes of this work, a comparison with the experimental results is not feasible. For engineering purposes, a simple estimation of the convective heat flux increase is formulated for the investigated flow regime.

The purposes of this section are summarized as follows:

- Validation of measured stagnation point heat fluxes in particle-free and particle-laden flows
- Measurement of kinetic energy flux reduction due to incident particle deceleration within the shock layer
- Measurement of the kinetic energy flux of rebounded particles
- a_{kin} coefficient determination for 20 µm to 60 µm sized Al_2O_3, MgO, and SiO_2 particles in a Mach number 2.1 air flow regime
- Comparison of the measured a_{kin} coefficients to the formulation by [14] and to literature experiments
- Formulation of a simple estimation approach of the convective heat flux increase for the investigated flow regime

The agenda of this section is organized as follows: First, details of the optical setup, the test conditions, and the probe shape are explained. Then, the mathematical formulations of heat flux determination are described. The particle reflection mode of the test conditions and the investigated particle materials are estimated and the procedure to determine the a_{kin} coefficient is explained.

The first analysis is about heat fluxes in particle-free flows. This analysis is followed by the investigation of kinetic energy flux reduction due to particle deceleration within the shock layer and the determination of the kinetic energy flux of rebounded particles. With the help of the determined kinetic energy fluxes, the a_{kin} coefficient is derived. Finally, heat fluxes in particle-laden flows and convective heat flux increases are discussed.

6.2. Methods

6.2.1. Shadowgraphy

The highly-resolved shadowgraphy system was used to measure individual particle size and -velocity. This system is described in detail in **section 5.2.5.1**. Although PTV data were recorded simultaneously, only data of the shadowgraphy system is considered in this section.

An example of the entire shadowgraphy FOV is given in **Fig. 56**. Shadowgraphy was capable to see a part of the incident flow, the bow shock, the shock layer, as well as a part of the probe tip. Incident particles were analysed in an area in front of the shock, called 'freestream' analysis area and marked with a purple rectangle, while rebounded particles were analysed in the shock layer, called 'shock layer' analysis area and marked with an orange rectangle. For each test, the distance between shock and probe, called the shock stand-off distance (Δ) was measured, and hence, the size of the analysis area varied slightly. On average, the incident particles analysis area was approximately 1.4x4.8 mm², while the rebounded particles analysis area was approximately 1.8x4.8 mm². The freestream analysis area is the same as used in the analysis of **section 5** to comply with the validated results of particle mass flow rate. The effect of the analysis area selection on the resulting incident particle mass flow rate and incident particle's kinetic energy is covered in **section 6.3.2**.

Velocity filters were applied on all detected particles to distinguish between incident and rebounded particles accordingly. These filters are listed in **Table 20** and **Table 21**, respectively. The freestream gas velocity was calculated with one-dimensional isentropic relations and is named 'theoretical velocity' in the following. The minimum velocity filter in x-direction of 300 m/s as well as the velocity filter in y-direction for incident particles were used to omit incorrectly assigned small and slow particle shadows for all test conditions. The x-direction velocity filter contains the strongest false vector deletion of small and slow 'particles' without affecting real vectors of larger particles. Regarding rebounded particles, the velocity ranges were set to account every detected rebounded particle with a reversed velocity direction and to neglect any incident particles. The filter velocity values were set manually.

Individual particle characteristics were used to calculate particle mass flow rate G_p and particle kinetic energy flux $\dot{e}_{kin}$. The applied formulations are given in **section 5.2.4**, **eq. (5-4)** and **eq. (5-5)**, respectively.

The shadowgraphy data, namely the particle mass flow rate as well as the particle kinetic energy flux, were additionally smoothed with a rolling-average filter with a length of 25 samples.

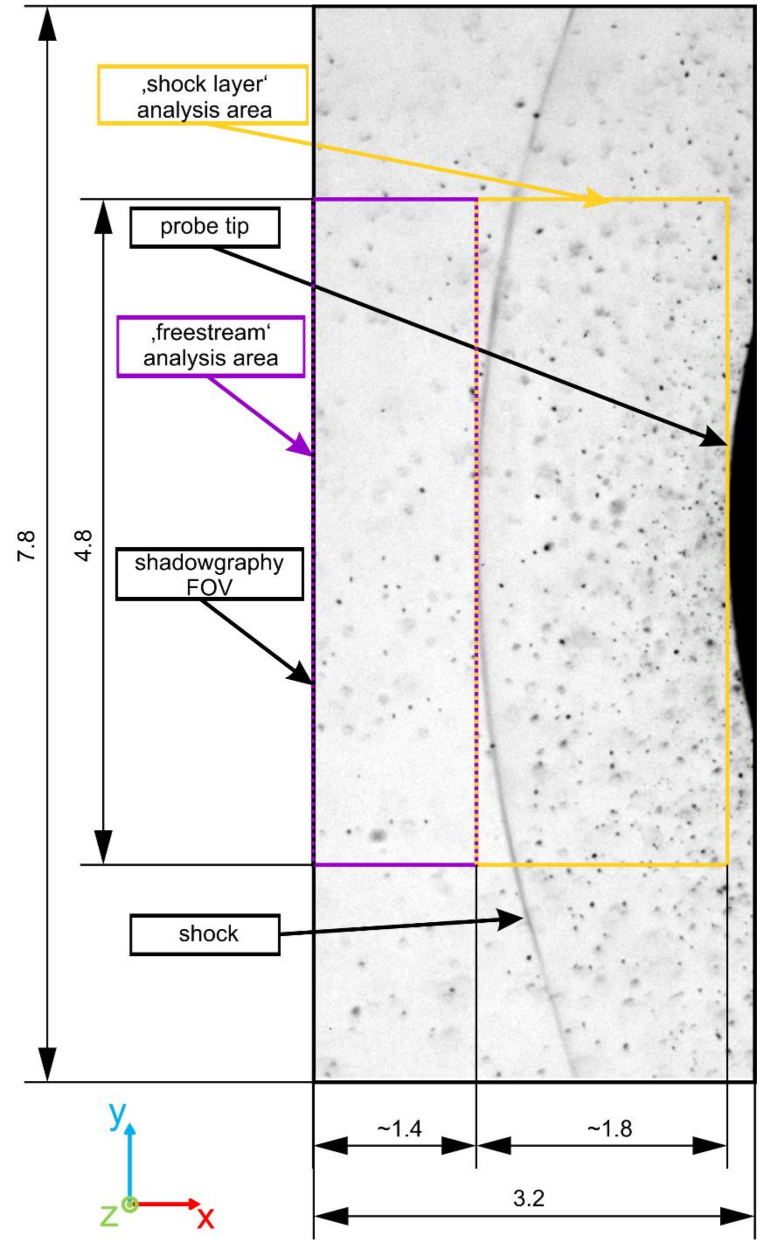
‚shock layer' analysis area
probe tip
‚freestream' analysis area
shadowgraphy FOV
shock
7.8
4.8
~1.4
~1.8
3.2
y
z
x

Fig. 56 Sketch of shadowgraphy's FOV: 'freestream' analysis area (purple) in front of the bow shock, while the 'shock layer' analysis area contains the entire shock layer (orange)

Table 20 Overview of applied filters to detect incident particles

parameter	unit	filter
u (x-direction velocity)	m/s	300 to theoretical velocity
v (y-direction velocity)	m/s	-20 to 20

Table 21 Overview of applied filters to detect rebounded particles

parameter	unit	filter
u (x-direction velocity)	m/s	-600 to -20
v (y-direction velocity)	m/s	-200 to 200

6.2.2. Test Conditions and Test Types

A total of 31 tests were performed, of which 29 were considered in the following analysis. Two tests were unconsidered because of a sensor- and a seeding malfunction. An overview of the considered tests is given in **Table 22**, where the tests are sorted by particle material, T_0, p_0, repetition, and test type. The analysed tests are the same as described in **section 5.2.3**, **Table 12**. As a reminder, a synonym was defined in the form: material - temperature level / pressure level - test run repetition - test type. For example, the synonym 'A-32-1-q0' stands for the run with Al_2O_3 particles, on the third temperature level of 373 K, on the second pressure level of 0.96 MPa, first repetition of test type 'q0'. The four different p_0 levels were 1: 0.6 MPa, 2: 0.96 MPa, 3: 1.3 MPa, and 4: 1.7 MPa. The five different T_0 levels were 1: 303 K, 2: 338 K, 3: 373 K, 4: 473 K and 5: 545 K.

The **Table 22** also lists the air mass flow $\dot{m}_{air}$, the Reynolds number based on the probe nose diameter d_{Probe}, the shock stand-off distance Δ, and the temporal mean of the particle mass concentration c_m. The active seeding time was set to 10 s in particle-laden flow test types 'akin' and 'qsum'. Differences in the listed p_0 and T_0 between **Table 12** and **Table 22** are caused by different time periods for which the temporal means are given. While in **Table 12** the 'seeded flow' period is considered, **Table 22** contains temporal means for the 'probe in seeded flow' period. The different periods are explained in the following.

Table 22 Test matrix, sorted by particle material, T_0, and p_0, and test type

synonym	p_0	T_0	$\dot{m}_{air}$	Re_{dProbe}	Δ	c_m
[-]	[mPa]	[K]	[g/s]	[-]	[mm]	[%]
A-11-1-akin	0.594	303.3	529.8	$8.13*10^5$	1.88	0.700
A-11-1-q0	0.594	302.8	530.8	$8.14*10^5$	1.86	0.000

A-12-1-akin	0.958	303.7	847.2	$1.31*10^6$	1.93	0.293
A-13-1-akin	1.288	303.5	1152.0	$1.76*10^6$	1.88	0.363
A-14-1-akin	1.686	303.9	1507.9	$2.30*10^6$	1.86	0.178
A-22-1-akin	0.950	338.4	803.4	$1.12*10^6$	1.77	0.837
A-22-1-qsum	0.950	338.1	787.2	$1.12*10^6$	1.75	0.064
A-31-1-akin	0.593	373.8	476.1	$6.10*10^5$	1.81	0.094
A-31-1-q0	0.594	373.8	478.3	$6.11*10^5$	1.87	0.000
A-31-1-qsum	0.594	373.1	478.5	$6.13*10^5$	1.73	0.798
A-31-2-q0	0.594	373.1	478.1	$6.13*10^5$	1.71	0.000
A-32-1-akin	0.951	374.2	765.2	$9.77*10^5$	1.80	0.639
A-33-1-akin	1.286	373.2	1032.9	$1.33*10^6$	1.78	0.042
A-33-1-q0	1.288	373.6	1029.9	$1.33*10^6$	1.74	0.000
A-33-1-qsum	1.286	373.2	1039.5	$1.33*10^6$	1.70	0.076
A-34-1-akin	1.682	373.3	1354.7	$1.73*10^6$	1.81	0.191
A-34-1-q0	1.681	373.3	1361.2	$1.73*10^6$	1.72	0.000
A-34-1-qsum	1.685	373.4	1358.5	$1.74*10^6$	1.72	0.064
A-42-1-q0	0.951	473.9	682.4	$7.15*10^5$	1.76	0.000
A-42-1-qsum	0.952	473.4	680.3	$7.16*10^5$	1.76	0.88
A-52-1-q0	0.950	543.5	633.3	$5.98*10^5$	1.82	0.000
A-52-1-qsum	0.952	544.0	637.4	$5.99*10^5$	1.86	1.06
M-31-1-akin	0.594	373.6	476.6	$6.11*10^5$	1.69	0.242
M-32-1-akin	0.949	373.5	764.1	$9.78*10^5$	1.70	0.218
M-33-1-akin	1.289	373.5	1036.7	$1.33*10^6$	1.71	0.096
M-34-1-akin	1.684	373.7	1355.4	$1.73*10^6$	1.68	0.115
S-31-1-akin	0.592	373.9	476.3	$6.09*10^5$	1.70	0.776
S-32-1-akin	0.951	373.7	764.4	$9.79*10^5$	1.70	0.514
S-33-1-akin	1.288	373.6	1034.9	$1.33*10^6$	1.70	0.057

Three different test types were conducted: so-called ‘q0’ tests focused on the determination of the stagnation point heat flux in a particle-free flow, so-called ‘akin’ tests focused on the determination of the a_{kin} coefficient, and the measurement of the stagnation point heat flux in a particle-laden flow was investigated in so-called ‘qsum’ tests. While in ‘q0’ and ‘qsum’ test types the probe was inserted into the flow for 5 s, the injection time was set to 185 s in runs of the ‘akin’ test type. The idea was to heat the probe in a particle-free flow up to a quasi-stationary temperature level, so that convective heating effects can be excluded. This procedure is similar to those described in [4, 11, 29]. The probe was heated up in a particle-free flow for 180 s, which was sufficient to achieve a constant temperature at the thermocouple’s back end. After this heating period in a particle-free flow, the particle injection was activated for 10 s, and the probe was removed from the flow 5 s after the particle injection start. All tests of the ‘akin’ test type were also used to extract the stagnation point heat flux in a particle-free flows $\dot{q}_0$ by evaluating the first 5 s after probe injection. The time curves of the probe’s temperatures are given in **Fig. 57** for the reference flow condition in an ‘akin’-type test. The measurement period is in between the two red dashed lines. There is a small time delay between measurement start at t = 0 s and probe injection. The particle injection started at t = 180 s, marked with a blue dotted line. The particles’ impact increased the measured stagnation point surface temperature. It is assumed that the application of the Cook-Felderman method [87] (see **eq. (6-6)**), starting at the particle injection, is valid for the period of particle injection. This was reasoned by constant temperatures at both ends of the coaxial-thermocouple prior particle injection. As a consequence, the resulting stagnation point heat flux corresponds only to the direct energy transfer from particles into the probe $\dot{q}_\mathrm{a}$. It was observed that a lower quasi-stationary surface temperature at the stagnation point T was measured, compared to the stagnation temperature T_0. The measured quasi-stationary surface temperature at the stagnation point T is in far agreement to the recovery temperature T_{rec}.

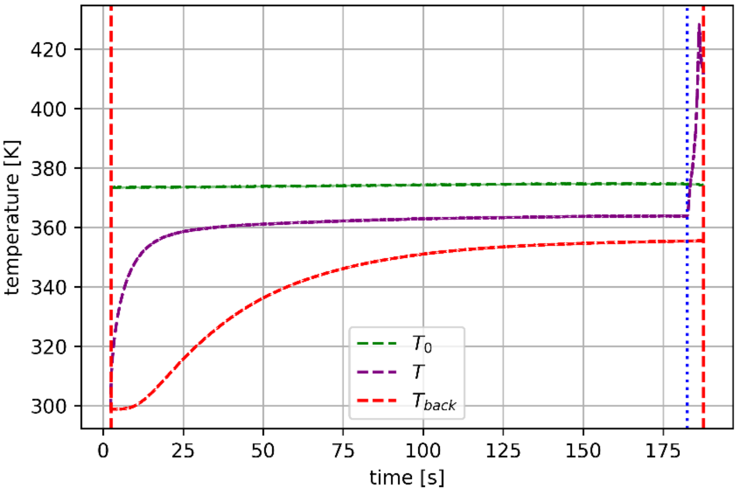

Fig. 57 Temperature time curve of the coaxial-thermocouple (purple: front, red: back) and the facilities’ T_0 of test run A-32-1-akin

6.2.3. Probe Shape

Since a decrease in the shock stand-off distance Δ from 1.93 mm to 1.68 mm during the entire test series (see **Table 22**, tests are not sorted in chronological order) was measured, it was investigated if this is caused by physical effects as described in **section 2.1**, e.g. **Fig. 2a**, or by a probe shape change.

To do so, the probe head shape was scanned once with a Keyence VR-5000 optical microscope after the tests made with Al_2O_3 and before tests made with SiO_2 and MgO. The probe shape profiles of a vertical (z = 0 mm) and of a horizontal (y = 0 mm) plane are depicted in **Fig. 58**. A hemispherical profile is shown for reference purposes. It turned out that the seeded particles slightly eroded the probe head, resulting in a change of the probe head shape from hemispherical to parabolic. As a consequence, it was concluded that the probe shape change is the main reason for the shock stand-off distance decrease. The probe shape change and its effects on the measured heat fluxes were not considered in the following analyses.

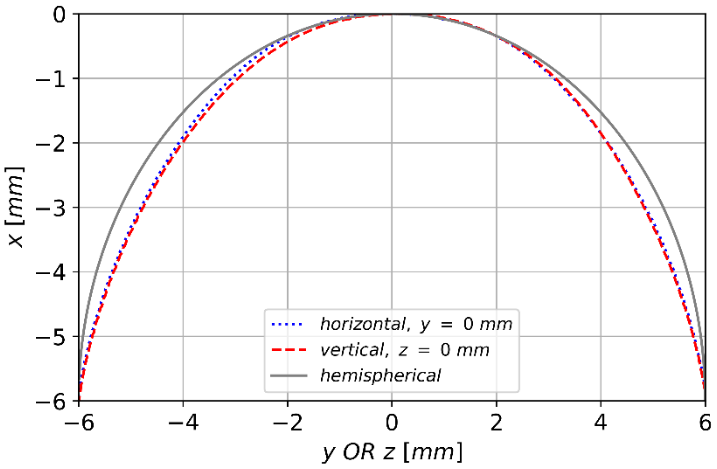

Fig. 58 Probe shape during the test series, horizontal (y = 0 mm) and vertical (z = 0 mm) profile

6.2.4. Stagnation Point Heat Flux

Stagnation point heat fluxes were required for the investigation of heating augmentation, especially for the determination of the a_{kin} coefficient. The implemented mathematical formulations to determine stagnation point heat fluxes are described in the following. The theoretical approximation by Fay-Riddell is used as reference when comparing stagnation point heat fluxes in particle-free flows.

6.2.4.1. Theoretical Stagnation Point Heat Flux

The stagnation point heat flux can be described in an equilibrium flow boundary layer around a hemispherical shaped probe with the formulation by Fay-Riddell [86]:

$$\dot{q}_{FR} = 0.76\,Pr^{-0.6}(\rho_w \mu_w)^{0.1}(\rho_e \mu_e)^{0.4}\left[1 + (Le^{0.52} - 1)\left(\frac{h_D}{h_{0e}}\right)\right](h_{0e} - h_w)\sqrt{\left(\frac{du_e}{dx}\right)_s} \quad (6\text{-}1)$$

The parameter Pr is the Prandtl number, ρ_w, μ_w, and h_w are the gas density, the dynamic gas viscosity, and the gas enthalpy at the stagnation point wall, respectively. The parameters ρ_e, μ_e, and h_{0e} are the gas density, the dynamic gas viscosity, and the total gas enthalpy at the boundary layer edge on the symmetry axis. The dissociation enthalpy of the gas is expressed by h_D. The Lewis number is expressed by Le. The term $(du_e/dx)_s$ is the velocity gradient at the stagnation point. Considering the modified Newtonian flow theory, the velocity gradient can be expressed by:

$$\frac{du_e}{dx} = \frac{1}{R_N}\sqrt{\frac{2*(p_s - p_\infty)}{\rho_s}} \tag{6-2}$$

In this formulation, the static pressure at the stagnation point is p_s and the ambient pressure in the freestream is p_∞.

The **eq. (6-1)** is the approximation for the stagnation point heat flux, which was established on calculations within the parameter range listed in **Table 23**. Here, the parameter C_1 is the recombination rate parameter and H is the simulated flight attitude. However, this approximation is widely used for reference reasons, as e.g. summarized in [88].

Table 23 Parameter range for which the Fay-Riddell approximation was established

parameter	unit	range
Pr	-	0.71
Le	-	1, 1.4, 2
C_1	-	0 to ∞
V_∞	m/s	1768 to 6949
H	m	7620 to 36576
T_w	K	300 to 3000

In this work, it is assumed that Le is always 1, and that all enthalpies can be expressed by:

$$h_x = c_{p\,gas} * T_x \tag{6-3}$$

The subscript ‘x’ is a generic placeholder. The heat capacity $c_{p\,gas}$ is assumed to be constant (see **Table 6**). Furthermore, it is assumed that the gas temperature at the boundary layer edge T_e is the stagnation temperature of the flow, T_0. As a consequence, h_{0e} is calculated with the help of **eq.(6-3)** and T_0. It is assumed that the gas temperature at the stagnation point wall is the wall temperature T_w. The gas densities ρ_w and ρ_e are calculated by means of the ideal-gas assumption, the static pressure at the stagnation point p_s, and the respective gas temperatures T_w, and $T_e = T_0$. It is assumed that the static pressure at the stagnation point p_s can be expressed by p_{02}, which is the stagnation pressure in the shock layer. This is calculated by means of the Pitot-Rayleigh relation. All dynamic viscosities are calculated with the formulations of Sutherland [89]:

If T_x larger than 120 K:

$$\mu_x = 17.89 * \left(\frac{398}{T_x+110}\right) * \left(\frac{T_x}{288}\right)^{1.5} * 10^{-6},\ [\mu_x] = \frac{kg}{m\ s} \tag{6-4}$$

Else:

$$\mu_x = 8.33 * \left(\frac{T_x}{120}\right) * 10^{-6} \tag{6-5}$$

The temporal change of the measured stagnation point surface temperature of the coaxial-thermocouple T_w was considered to achieve a temporal-resolved heat flux approximation with **eq. (6-1)**.

6.2.4.2. Experimental Stagnation Point Heat Flux

The stagnation point heat flux $\dot{q}_{\mathrm{SP}}$ was derived with the Cook-Felderman equations [87]. The following equations were used for calculation [90-92]:

$$\dot{q}_{SP}(t_n) = \frac{2\sqrt{\rho c k}}{\sqrt{\pi}} \sum_{i=1}^{n} \frac{\Theta(t_i) - \Theta(t_{i-1})}{(t_n - t_i)^{0.5} + (t_n - t_{i-1})^{0.5}} \tag{6-6}$$

with:

$$\Theta(t_i) = T(t_i) - T(t_0) \tag{6-7}$$

Here, the term ρck is the coaxial thermocouple material constant, and $\theta(t_i)$ is the difference between stagnation point surface temperature T at time t_i and the initial stagnation point surface temperature at time t_0. The specific material constant was determined experimentally by comparing the coaxial thermocouple to a calibrated coaxial thermocouple from Shock Wave Laboratory of RWTH Aachen University [93]. Therefore, both thermocouples were mounted each on a flat-faced cylinder. These cylinders were placed in comparable supersonic flows. The coaxial thermocouple material constant was adjusted to match the measured heat flux of the calibrated reference coaxial thermocouple. A general uncertainty of this process was assumed to be 5 %.

The **eq. (6-6)** is based on the theory of one-dimensional heat conduction into a semi-infinity body with constant material properties. Following [94], lateral heat fluxes have only minor impact on the measured stagnation point heat fluxes due to the choice of stainless steel as probe material. The given equation is only valid as long as the temperature at the coaxial thermocouple's back end T_{back}

is constant. T_{back} was measured with a second thermocouple which was placed at the coaxial thermocouple's back end. In the following analyses, it was assumed that **eq. (6-6)** can be applied as long as:

$$\Theta_{back}(t_i) = T_{back}(t_i) - T_{back}(t_0) < 0.1\ K \tag{6-8}$$

The thermocouple's raw signals were recorded with 50000 Hz. In a first step, the raw signal was smoothed with the help of a 500-sample-length rolling-average filter and down-sampled to the shadowgraphy's recording rate of 100 Hz. This signal was additionally smoothed with a second rolling-average filter with a length of 25 samples to agree with shadowgraphy data smoothing. The resulting temperature signal was used for heat flux computation.

6.2.5. Particle Reflection Mode

As described in **section 2.1.2**, it was predicted that the particle reflection mode has impact on the a_{kin} coefficient. To consider the particle reflection mode in the following analyses, the limiting impact velocity V_{p*} was calculated to differ between the elastic and erosive reflection mode (see **eq. (2-1)**). As a reminder, particles with higher impact velocity than V_{p*} are referred to be erosive, while particles with slower impact velocity are referred to be elastic. The factor V_{p*} depends only on material properties of the particles and the probe.

Considering the investigated particle materials and all present materials of the probes, V_{p*} was calculated for each particle / probe material combination in **Table 24**. Material properties of chromel were taken into consideration for the following analyses, because the major cross section of the coaxial-thermocouple is made of it.

Table 24 V_{p*} for all particle / probe material combinations

V_{p*} [m/s]	**Al_2O_3**	**MgO**	**SiO_2**
stainless steel	387	285	418
constantan	380	282	412
chromel	**448**	**302**	**468**

6.2.6. Modelling of the A_{kin} Coefficient

One purpose of **section 6** is to compare measured a_{kin} coefficients with the prediction model deduced in [14], which is described in the following. This model considers the energy flux from particles to the solid for elastic particle reflection. It includes normal and tangential velocity components of incident, rebounded, and chaotized particles. Chaotized particles are incident particles interacting with rebounded particles. The authors of [14] mentioned that the concentration of chaotized particles is low in flows with initial particle mass concentrations up to

30 %. Since in this work only particle concentrations lower than 1 % were investigated, it is assumed that chaotized particles are of minor importance in the following analyses. Considering only the normal velocity components and neglecting chaotized particles, the parameter a_{kin} can be modelled with the following equations:

$$a_{kin} = \frac{\dot{q}_{SP}}{\dot{e}_{kin\,inc} - \dot{e}_{kin\,reb}} = \left[1 + \frac{\sigma_s}{\sigma_p}\left(\frac{c_s}{c_p}\right)^3\right]^{-1} \tag{6-9}$$

with:

$$c_j = \left(\frac{E_j}{\rho_j}\right)^{0.5} \quad of\ j - material \tag{6-10}$$

The parameters $\dot{q}_{\mathrm{SP}}$, E and ρ_j are the Young's modulus and the density of the j-material, respectively. Here, the subscript 's' stands for the sample material, while the subscript 'p' stands for the particle material. The heat transfer aspect is neglected on the left-hand side in in **eq. (6-9)**. The formulation results are given in **Table 25**, considering the material properties listed in **Table 7**. The influence of the selected probe material on the estimated a_{kin} coefficient is not significant.

Table 25 Estimated a_{kin} coefficient for elastic reflection and for all particle/probe material combinations. The right term of eq. (6-9) was used for computation

a_{kin} **[-]**	Al_2O_3	**MgO**	SiO_2
stainless steel	0.95	0.79	0.73
constantan	0.97	0.86	0.82
chromel	**0.94**	**0.76**	**0.70**

6.3. Analysis

This section is organized as follows: First of all, the measured stagnation point heat fluxes in particle-free flows are compared to approximations from literature. Then, particle flows are investigated, starting with the determination of particle energy fluxes of incident particles in the freestream and in the shock layer, followed by the determination of the kinetic energy flux of rebounded particles. The a_{kin} coefficient is derived from measured stagnation point heat fluxes and the measured particle energy fluxes in particle-laden flows of test-type 'akin' (see **section 6.2.2**). In the end, stagnation point heat fluxes in particle-laden flows are investigated, in which convective heating augmentation and direct energy transfer from impacting particles occur simultaneously.

6.3.1. Heat Flux in Particle-Free Flows

To evaluate how accurate stagnation point heat fluxes were measured with the presented experimental setup, heat flux data of particle-free flow tests were compared to the reference approximation by Fay and Riddell [86] (see **section 6.2.4.1**). The time curves of the stagnation point heat fluxes of reference test run A-32-1-akin are illustrated in **Fig. 59**. The time on the x-axis was set to zero when the probe reached its final position within the flow. The heat flux calculation was terminated if one of the following conditions was met: the back-end thermocouples detected a temperature increase (see **eq. (6-8)**) or the probe was rejected out of the flow. The measured heat flux signal is coloured light-orange. The down-sampled heat flux signal is smoothed with a rolling-average smoothing filter, indicated with 'RA'. The smoothed signal is coloured red. The approximation of the stagnation point heat flux $\dot{q}_{\mathrm{FR}}$ is shown as a blue line for comparison purposes. The temporal change of the stagnation point surface temperature T of the coaxial-thermocouple was considered in the calculation of a temporal-resolved $\dot{q}_{\mathrm{FR}}$.

The experimentally determined stagnation point heat flux is in accordance with the approximation for approximately 0.5 s for the exemplarily shown test run. Since the approximated heat flux decreases stronger, the differences become larger with increasing measurement time. This can be reasoned by lateral heat fluxes and a relatively small probe diameter, compared to the coaxial thermocouple diameter. Lateral heat fluxes are neglected in the Fay-Riddell approximation. Another aspect could be the validity of **eq. (6-8)** for several-second measurement periods, since it is commonly used for the heat flux calculation in the millisecond range.

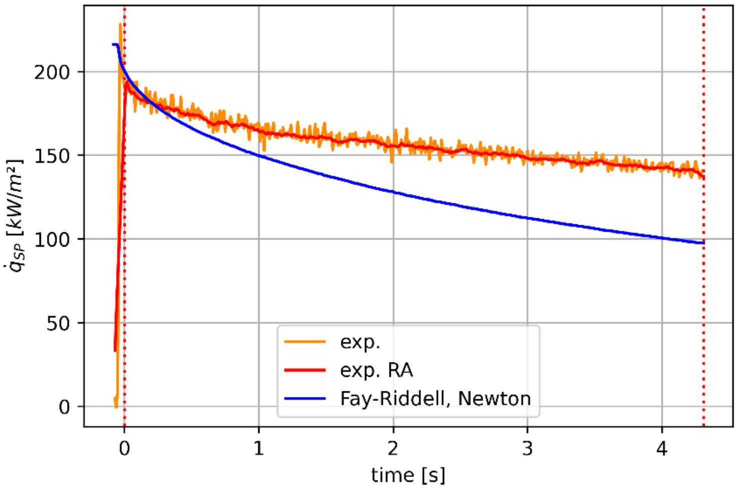

Fig. 59 Differences between measured stagnation point heat flux, A-32-1-akin, and an approximation, based on the equations of [86] and the probe temperature T

The average as well as the interquartile ranges (IQR) for the time span of 0.5 s were computed for all investigated flow conditions. The two test types 'q0' as well as 'akin' were considered. The comparison is depicted in **Fig. 60**. The mean values are shown as dots, and the IQRs are shown as error bars. A linear fit identifies the relation between measured heat fluxes $\dot{q}_{SP}$ and approximated heat fluxes $\dot{q}_{\mathrm{FR}}$. All experimentally-determined heat fluxes were on average -1.3 % lower than the approximated heat fluxes.

The small deviation between experiments and approximation indicates that the heat flux measurements were reliable and can be used for a_{kin} coefficient calculation for the above-mentioned time period of 0.5 s.

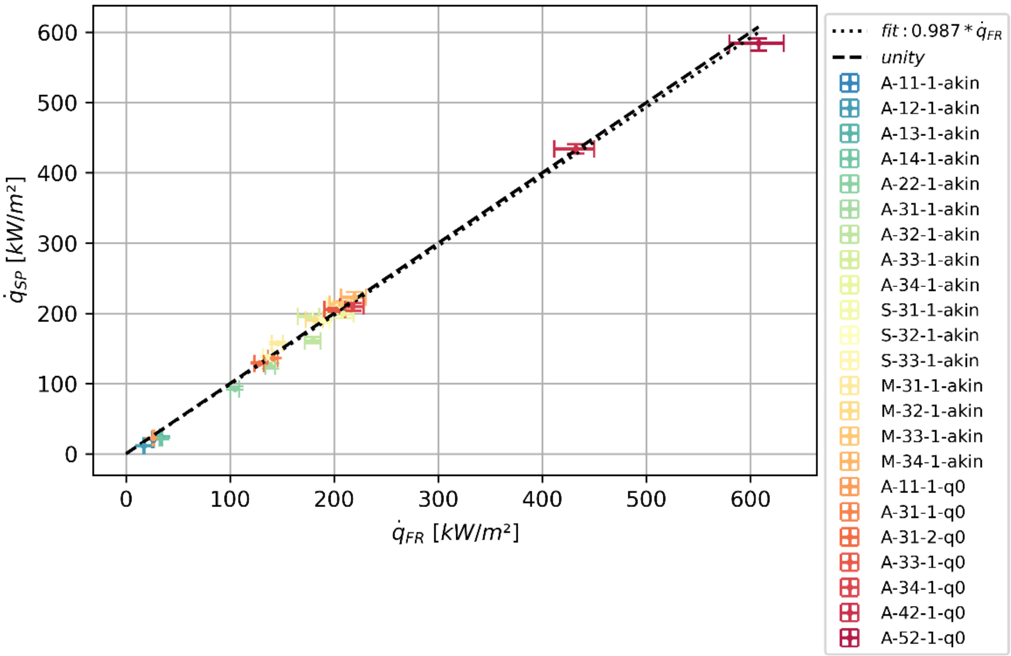

Fig. 60 Comparison of temporal mean of approximated and experimentally determined stagnation point heat fluxes

6.3.2. Energy Flux of Incident Particles

The determination of the a_{kin} coefficient requires the measurement of the stagnation point heat flux and the measurement of the kinetic energy flux of incident particles. One fundamental parameter to determine of the kinetic energy flux is the particle velocity. While in literature the particle velocity at impact was only computed (see **section 1**), this section is about the measurement of particle velocity, and hence, the kinetic energy flux of particles, in the shock layer. Generally, particles are decelerated when entering the shock layer. The effect of particle deceleration on the resulting kinetic energy flux of all incident particles at reference flow condition for three particle materials is illustrated in **Fig. 61**, **Fig. 62**, and **Fig. 63**. The orange error bars represent the velocity IQR of all particles in the freestream (‘fs’, see **section 6.2.1**), while the blue error bars represent the velocity IQR of all particles in the shock layer (‘sl’). The red dotted lines represent the limiting impact velocity V_{p*} (see **Table 24**). The blue dotted lines represent the theoretical gas velocity in the freestream, while the green dotes lines illustrate the theoretical gas velocity in the shock layer.

The kinetic energy flux of incident particles with sizes up to the given value on the x-axis is called 'cumulated' kinetic energy flux ($cum.\dot{e}_{kin}$) in the following. The parameter $cum.\dot{e}_{kin}$ is considered for both analysis areas, the freestream and the shock layer. Both of the cumulated kinetic energy fluxes are scaled to $\dot{e}_{kin\,fs}$, the kinetic energy flux of all incident particles in the freestream. These ratios are shown as light bars. The colors correspond to the freestream and the shock layer analysis area, respectively. As an example, approximately 50 % of the kinetic energy flux in the freestream is distributed on particles smaller than 22.5 µm (Al_2O_3), 17.5 µm (MgO), or 40 µm (SiO_2) (light orange bars). The darker parts of the bars represent the ratio of the cumulated erosive kinetic energy flux $cum.\dot{e}_{kin\,erosive}$ and $\dot{e}_{kin\,fs}$. The cumulated erosive kinetic energy flux considers only particles faster than V_{p*} (see **section 6.2.5**).

Generally, the velocity of incident particles is in between the theoretical gas velocity in the freestream and the theoretical gas velocity in the shock layer. Smaller particles decelerated faster due to their lower inertia. As a consequence, the absolute velocity difference of particles in the freestream and the shock layer increases with decreasing particle size. The velocity IQR range of particles in the shock layer is larger compared to those of particles in the freestream, especially for smaller particle sizes. This is caused by the continuous deceleration of particles in the shock layer and the summation of particles just entering the shock layer and particles already travelling through the shock layer.

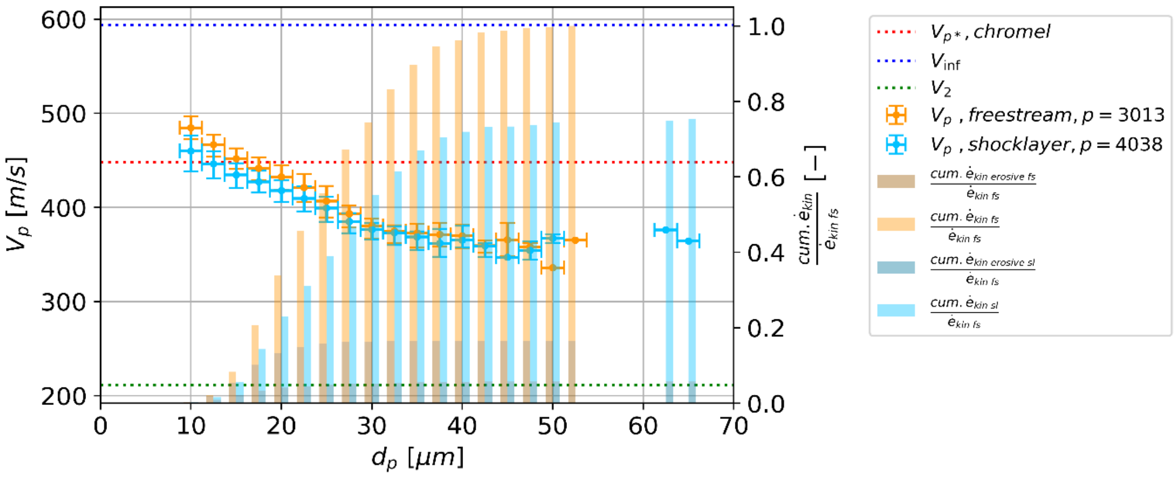

Fig. 61 Relation between particle velocity, size, and the kinetic energy of incident particles in the freestream and in the shock layer, run ID A-32-1-akin

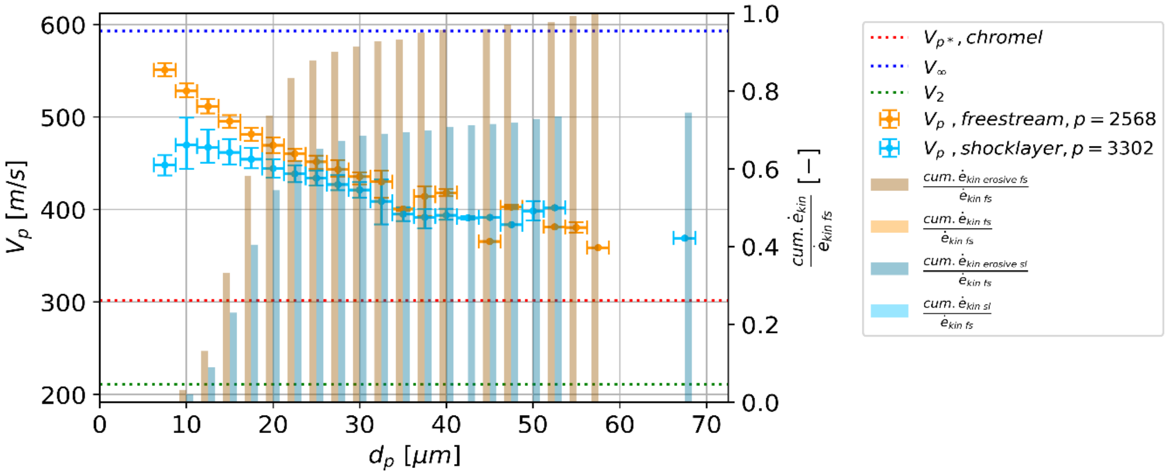

Fig. 62 Relation between particle velocity, size, and the kinetic energy of incident particles in the freestream and in the shock layer, run ID M-32-1-akin

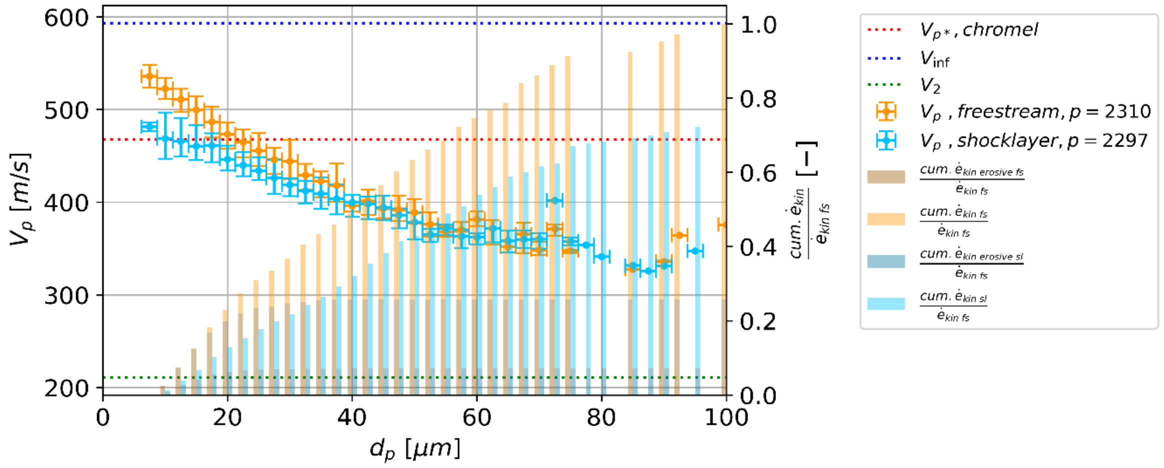

Fig. 63 Relation between particle velocity, size, and the kinetic energy of particles, run ID S-32-1-akin

A summary of detected kinetic energy flux reduction in the shock layer is given in **Table 26**. The kinetic energy flux of incident particles in the shock layer is up to 29 % smaller than those of particles in the freestream. The detected erosive percentage of the kinetic energy flux is reduced significantly for Al_2O_3 and SiO_2 particles in the shock layer. No erosive percentage reduction for MgO particles was measured, because the decelerated particles are still faster than V_{p*}. These energy flux reductions are mainly caused by the particle deceleration. The deceleration depends on particle inertia and the drag force on the particles in the shock layer.

The distribution of kinetic energy flux on particles with different size is a complex function depending on particle size, particle material, and flow conditions (compare **Fig. 61**, **Fig. 62**, and **Fig. 63**). The kinetic energy flux of incident particles in the shock layer $\dot{e}_{kin\ inc\ sl}$ is considered in the following for a_{kin} coefficient determination.

Table 26 Kinetic energy flux reduction due to particle deceleration within the shock layer, test type 'akin'

synonym	**Re$_{dProbe}$**	$\frac{\dot{e}_{kin\,inc\,erosive\,fs}}{\dot{e}_{kin\,inc\,fs}}$	$\frac{\dot{e}_{kin\,inc\,erosive\,sl}}{\dot{e}_{kin\,inc\,sl}}$	$\frac{\dot{e}_{kin\,inc\,sl}}{\dot{e}_{kin\,inc\,fs}}$
[-]	[-]	[%]	[%]	[%]
A-11	$8.13*10^5$	0	0	76
A-12	$1.31*10^6$	1	0	77
A-13	$1.76*10^6$	7	1	73
A-14	$2.30*10^6$	19	1	71
A-22	$1.12*10^6$	6	3	74
A-31	$6.10*10^5$	3	1	92
A-32	$9.77*10^5$	16	7	75
A-33	$1.33*10^6$	36	14	87
A-34	$1.73*10^6$	66	29	79
M-31	$6.11*10^5$	100	100	82
M-32	$9.78*10^5$	100	100	74
M-33	$1.33*10^6$	100	100	82
M-34	$1.73*10^6$	100	99	72
S-31	$6.09*10^5$	8	5	82
S-32	$9.79*10^5$	25	9	72
S-33	$1.33*10^6$	27	11	83

6.3.3. Energy Flux of Rebounded Particles

While the kinetic energy flux of rebounded particles was never measured and considered in particle-induced heating augmentation literature so far, this section discusses if its neglection is feasible in the following analyses.

The scaled difference between incident particle kinetic energy flux $\dot{e}_{kin\,inc}$ and rebounded particle kinetic energy flux $\dot{e}_{kin\,reb}$ is compared in **Fig. 64** to estimate the influence of the rebounded particle kinetic energy flux on the determination of the a$_{kin}$ coefficient (see **eq. (6-11)**). The bars indicate the mean and the interquartile range (IQR) of each test. The scaled difference of the kinetic energies $\dot{e}_{kin\,reb}$ and $\dot{e}_{kin\,inc}$ is slightly increasing with increasing $\dot{e}_{kin\,inc}$ for Al_2O_3 and SiO_2 tests. It is always larger than 97.5 %, meaning that $\dot{e}_{kin\,reb}$ is always less than 2.5 % of $\dot{e}_{kin\,inc}$. Almost no rebounded MgO particle were detected. The question arises whether these particles broke up during impact into pieces which are smaller than 5 µm (the resolution limit of the implemented shadowgraphy system, see **section 5.2.5.1.1**) or whether they stuck on the probe surface. Future investigations of the probe surface could give answers to this. Generally, a larger kinetic energy flux of rebounded particles would increase the a_{kin} coefficient, if the formulation of **eq. (6-9)** is considered. However, it is assumed that the neglection of the kinetic energy flux of rebounded particles $\dot{e}_{kin\,reb}$ is reasonable for the determination of the a_{kin} coefficient.

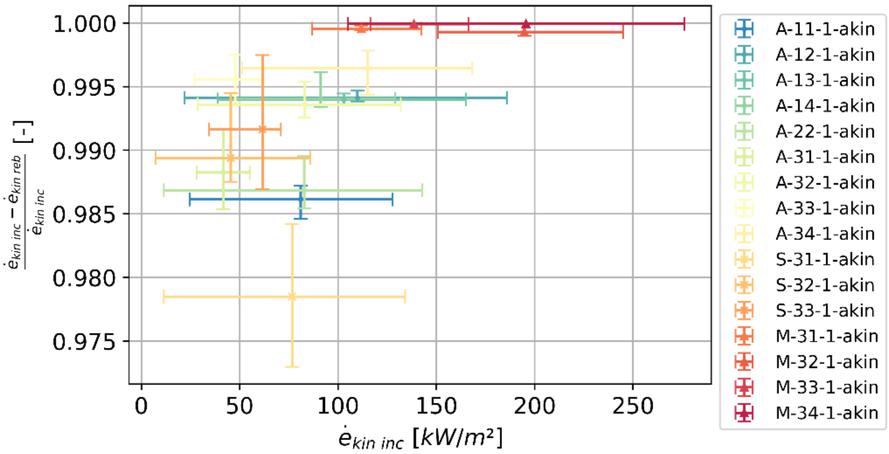

Fig. 64 Significance of rebounded particle kinetic energy flux, compared to incident particle kinetic energy flux for all 'akin'-type tests

6.3.4. A_{kin} Coefficient

The time curves of the relative stagnation point surface temperature θ as well as $\dot{e}_{kin\,inc\,sl}$ are plotted in **Fig. 65** and **Fig. 66**, respectively. Data of all 'akin'-type tests made with Al_2O_3 particles were considered for these plots. The given time on the x-axis is set to 0 at the start of the particle injection, which is approximately 180 s after probe injection (see **Fig. 57**). Significant unexpected variations of the $\dot{e}_{kin\,inc\,sl}$ were observed. While for most of the tests $\dot{e}_{kin\,inc\,sl}$ is increasing with time, some tests show maximum $\dot{e}_{kin\,inc\,sl}$ right after seeding start and its decrease with increasing time. These unexpected variations of the $\dot{e}_{kin\,inc\,sl}$ were caused by an unregulated particle seeding rate of the seeding device. The stored particles in the seeding device stuck together slightly, which could not be dissolved satisfactorily within the device. The relative stagnation point surface temperature behaves similar to $\dot{e}_{kin\,inc\,sl}$. Data before the maximum achieved stagnation point surface temperature are marked with a solid and a dashed line, the data beyond this point are marked with a dotted line. The difference between the solid line and a dashed line is explained below.

Considering the results of **section 6.3.3** and following the common neglection of the heat transfer aspect, the a_{kin} coefficient is determined experimentally with the following equation:

$$a_{kin} = \frac{\dot{q}_{SP}}{\dot{e}_{kin\,inc\,sl} - \dot{e}_{kin\,reb\,sl}} \sim \frac{\dot{q}_{SP}}{\dot{e}_{kin\,inc\,sl}} \qquad (6\text{-}11)$$

It must be noted that only particles in the shock layer were considered in the determination of $\dot{e}_{kin\ inc\ sl}$, which are already decelerated (see section **6.3.2**). Particles in the shock layer were chosen, since it is more physical to investigate the relation between the kinetic energy of the particles, which are almost impacting, and the measured heat flux than considering the kinetic energy of particles in the freestream. Apart from that, also the coefficient $a_{kin\ fs}$ was calculated (see **eq. (6-12)**) to consider the kinetic energy flux of particles in the freestream. This is caused by the fact that all determined a_{kin} coefficients from literature are based on freestream particles, because only these were measured. The coefficient $a_{kin\ fs}$ was calculated with the following equation:

$$a_{kin\ fs} = a_{kin} * \frac{\dot{e}_{kin\ inc\ sl}}{\dot{e}_{kin\ inc\ fs}} \tag{6-12}$$

The kinetic energy ratio in **eq. (6-12)** is given in **Table 26**.

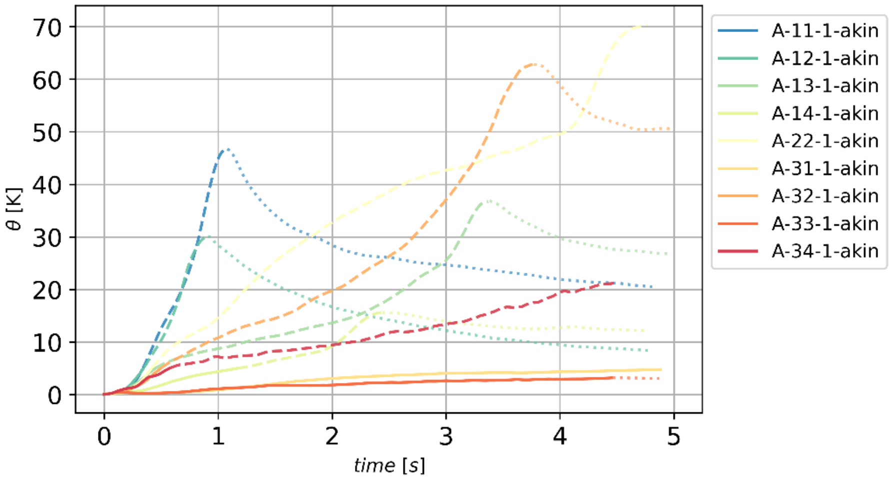

Fig. 65 Temporal change of θ for all 'akin'-type tests with Al_2O_3 particles

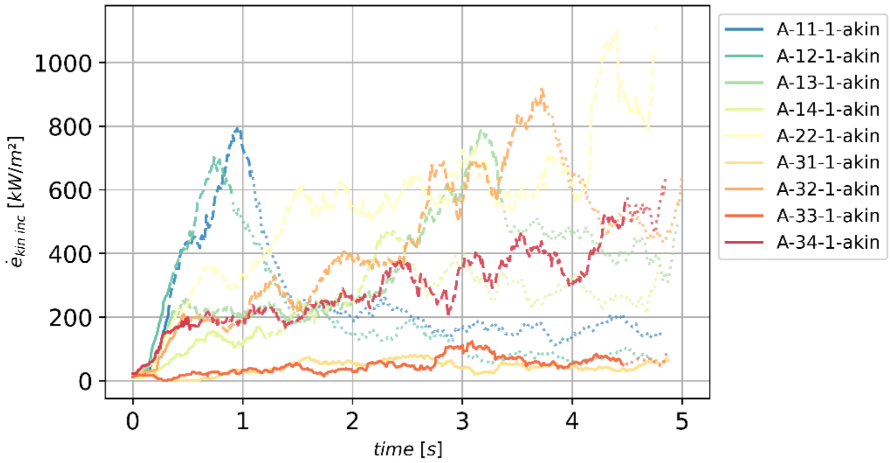

Fig. 66 Temporal change of $\dot{e}_{kin\ inc\ sl}$ for all 'akin'-type tests with Al_2O_3 particles

The ratio of kinetic energy of shock layer particles and the heat flux of all Al_2O_3 tests is shown in **Fig. 67**. Like in **Fig. 65** and **Fig. 66**, data before the maximum achieved stagnation point surface temperature are marked with a solid and a dashed line, the data beyond this point are marked with a dotted line. The a_{kin} coefficient is decreasing when the maximum stagnation point surface temperature, or to be precise, the maximum incident particle energy flux, is reached. Furthermore, it becomes smaller than zero when the stagnation point surface temperature or respectively, the incident particle energy flux, is decreasing for a longer time period (see A-12-1-akin). This can be explained by convective cooling effects and the variation of the incident particle energy flux. Due to the direct energy transfer, the particle energy flux heats up the probe to temperatures higher than achievable particle-free flow stagnation point temperatures. The higher the particle energy flux, the higher the achievable temperature. If the particle energy flux drops from high values, also the maximum achievable temperature decreases and the probe is cooled by convection to the 'new' maximum achievable temperature. In the case of A-12-1-akin, the incident particle energy flux started at a high value and was decreasing constantly. Here, the convective cooling reduced the measured stagnation point heat flux even to negative values, although a significant particle energy flux was measured for the test period. As a consequence, the determination of the a_{kin} coefficient itself depends on the temporal change of the kinetic energy flux of incident particles. Future studies should focus on the improvement of homogeneous particle seeding, since a temporal-homogeneous seeding should simplify the data analysis.

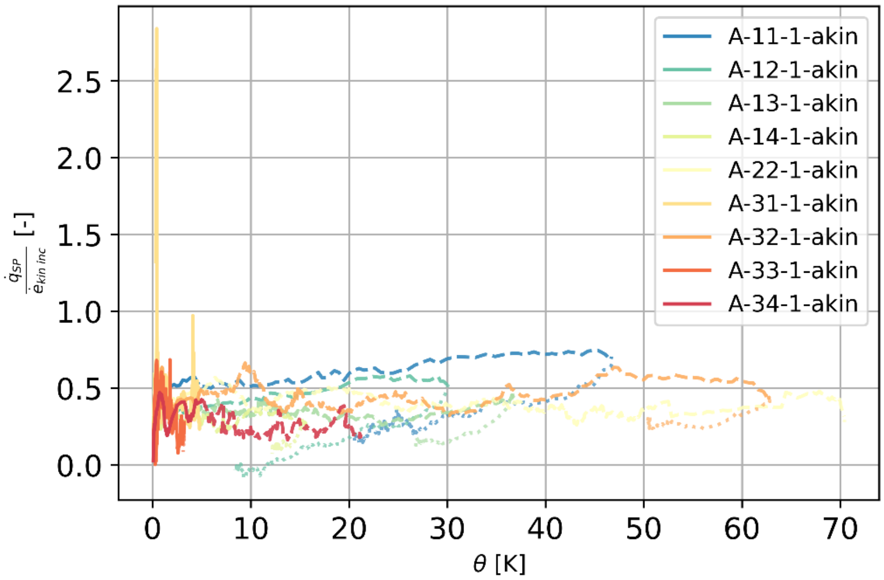

Fig. 67 The a_{kin} coefficient vs. relative stagnation point temperature θ

Generally, the larger the temperature difference θ, the larger the potential impact of convection effects. To minimize the effect of convection cooling on the determination of the a_{kin} coefficient, only data is considered in which θ is smaller than 5 K. This value was estimated to be a good trade-off between much particle data and less convection effects. These data are marked in **Fig. 65**, **Fig. 66**, and **Fig. 67** with a solid line. Peaks of the a_{kin} coefficient larger than unity in **Fig. 67** can be explained by short time periods, in which only few particles were detected (see **Fig. 66**, A-31-1-akin at t = 0.5 s).

The a_{kin} coefficients of all tests are summarized in **Table 27**, considering a θ smaller than 5 K and a maximum measurement time period of 0.5 s (see **section 6.3.1**). The experimentally determined a_{kin} coefficient mean is in the range of 0.24 to 0.50, 0.32 to 0.86, and 0.03 to 0.06 for Al_2O_3, SiO_2, and MgO particles, respectively. The respective mean values are 0.36, 0.70, and 0.05. The mean value of A-31-akin is outside of its IQR. This can be explained by some measured a_{kin} values significantly larger than unity, which are caused by a short time period in which only few particles were detected (see **Fig. 66**, A-31-1-akin at t = 0.5 s).
The influence of the selected θ range on the determined a_{kin} coefficient is investigated by a θ limit variation from 2 to 10 K (see **Table 27**). Since the mean a_{kin} values of the θ limit variations are within the IQR range of the measured a_{kin} values with θ smaller than 5 K, it is concluded that the impact of the θ limit selection on the determined a_{kin} coefficient can be neglected.

To compare the determined $a_{kin\ fs}$ values to the estimations of **eq. (6-9)** for elastic particle reflection (see **section 6.2.6**, predictions given in **Table 25**), it must be considered if the investigated flows provided an elastic or an erosive particle reflection environment. Therefore, the ratio of erosive kinetic energy flux $\dot{e}_{kin\ inc\ erosive\ sl}$ and the kinetic energy flux of all incident particles $\dot{e}_{kin\ inc\ sl}$ within the shock layer was considered to distinguish between an elastic and an erosive particle reflection environment. While all Al_2O_3 and SiO_2 tests can be seen as elastic, all MgO particle tests provided a complete erosive particle reflection environment.
It seems that the simplified formulation overestimates the a_{kin} coefficient by a factor of up to 3 for Al_2O_3 particles. This might be caused by a higher $\dot{e}_{kin}$ detection rate of shadowgraphy, compared to the measurement techniques used in [12]. The difference of up to 29 % of the kinetic energy flux of particles in the shock layer and in the freestream is too small to be an explanation. The derived $a_{kin\ fs}$ coefficient of Al_2O_3 particles is almost the half of the commonly used factor of 0.7 of [11]. The question arises if the literature value is reliable, since it included a general assumption of the particle impact velocity and provided no accurate particle measurement method like in this analysis. Moreover, run-averaged particle mass flow rates were considered although significant changes in the particle mass flow rate in the literature experiments were observed.
For SiO_2 particles, the simplified formulation is in agreement with two of three tests. However, the measured a_{kin} coefficients are at least two times larger than those measured with larger SiO_2 particles in a similar flow with significant higher particle mass flow rates [12]. In those tests, shielding effects could have been occurred, leading to a significant decrease of measured heat flux. Future investigations with SiO_2 particles have to confirm the measured a_{kin} coefficient and to analyse the influence of shielding effects.
Because MgO tests were completely erosive, a direct comparison with the simplified estimation of [14] is not feasible, since the estimation is only applicable to elastic particle reflection environments.

The experimentally determined $a_{kin\ fs}$ coefficient of 0.04 for MgO particles in erosive environments is less than half of the erosive environment suggestion of 0.1 [14].

The determined $a_{kin\ fs}$ coefficients for Al_2O_3 and MgO particles are significantly smaller than the literature predictions. This can be reasoned by the much higher accuracy of the implemented particle measurement method, namely shadowgraphy. Future tests with different particle materials and MgO particles in an elastic particle reflection environment have to confirm this thesis.

Table 27 Measured a_{kin} coefficients for $t \leq 0.5$ s

synonym	**Re_{dProbe}**	$\frac{\dot{e}_{kin\ inc\ erosive\ sl}}{\dot{e}_{kin\ inc\ sl}}$	**a_{kin} (IQR), ($\theta \leq 5K$)**	**a_{kin} ($\theta \leq 2K$)**	**a_{kin} ($\theta \leq 10K$)**	**a_{kin} (eq. (6-9))**	**$a_{kin\ fs}$ ($\theta \leq 5K$)**
[-]	[-]	[%]	[-]	[-]	[-]	[-]	[-]
A-11	$8.13*10^5$	0	0.42 (0.33, 0.51)	0.38	0.45	0.94	0.32
A-12	$1.31*10^6$	0	0.32 (0.29, 0.35)	0.30	0.34	0.94	0.25
A-13	$1.76*10^6$	1	0.34 (0.30, 0.38)	0.32	0.34	0.94	0.25
A-14	$2.30*10^6$	1	0.33 (0.27, 0.38)	0.33	0.33	0.94	0.23
A-22	$1.12*10^6$	3	0.50 (0.41, 0.56)	0.51	0.50	0.94	0.37
A-31	$6.10*10^5$	1	0.34 (0.13, 0.18)	0.34	0.34	0.94	0.31
A-32	$9.77*10^5$	7	0.44 (0.39, 0.48)	0.45	0.44	0.94	0.33
A-33	$1.33*10^6$	14	0.24 (0.07, 0.38)	0.24	0.24	0.94	0.21
A-34	$1.73*10^6$	29	0.32 (0.26, 0.39)	0.30	0.32	0.94	0.25
M-31	$6.11*10^5$	100	0.03 (0.01, 0.05)	0.03	0.03	-	0.02
M-32	$9.78*10^5$	100	0.04 (0.01, 0.05)	0.04	0.04	-	0.03
M-33	$1.33*10^6$	100	0.07 (0.04, 0.09)	0.07	0.07	-	0.06
M-34	$1.73*10^6$	99	0.06 (0.03, 0.10)	0.06	0.06	-	0.04
S-31	$6.09*10^5$	5	0.36 (0.26, 0.45)	0.32	0.39	0.70	0.30
S-32	$9.79*10^5$	10	0.85 (0.51, 1.10)	0.86	0.85	0.70	0.61
S-33	$1.33*10^6$	11	0.89 (0.18, 1.56)	0.83	0.89	0.70	0.74

Since a relation between particle-induced heating augmentation and Re_{dProbe} was found in [11], the dependence of the a_{kin} coefficient on Re_{dProbe} was analysed and is plotted in **Fig. 68**. An increasing a_{kin} coefficient with increasing Re_{dProbe} can be interpreted only in tests with MgO particles. The IQR bars of the a_{kin} coefficient of Al_2O_3 tests are too large for an appropriate relation interpretation.

The significant lower MgO-based a_{kin} coefficients can be explained with stronger cooling or ablation effects in erosive environments. The fact that lower a_{kin} coefficients were measured in an erosive particle reflection environment is in agreement with previous particle-induced heating augmentation studies, in which a decrease of the a_{kin} coefficient from elastic to erosive environments was derived [11, 14].

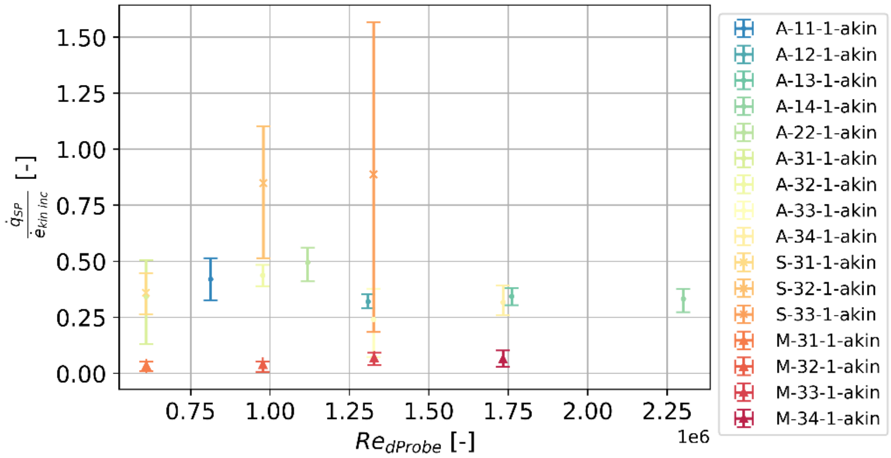

Fig. 68 Measured a_{kin} coefficient vs. Re_{dProbe} for all tests

6.3.5. Heat Flux in Particle-Laden Flows

With the help of the derived a_{kin} coefficients from **section 6.3.4**, the convective heat flux increases $\Delta\dot{q}$ can be derived from heat flux measurements in particle-laden flows of the so-called test type 'qsum' (see **section 6.2.2**). In the following, first the total heat flux augmentation, including convective heat flux increases and the direct energy transfer of impacting particles, are analysed. Then, the convective heat flux increases are discussed.

The time curve of the kinetic energy flux of incident particles for all conducted 'qsum'-type tests are shown in **Fig. 69**. It was intended to achieve similar kinetic energy fluxes. However, the kinetic energy fluxes varied accidentally.

Heat fluxes were only calculated when the probe reached a constant position within the flow and when the back-end thermocouple did not detect a temperature increase. As discussed in **section 6.3.1**, only a time period of 0.5 s was considered to avoid lateral heat flux effects on the coaxial thermocouple.

The ratio of the stagnation point heat flux in a particle-laden flow and in a particle-free flow for all 'qsum'-type tests are illustrated in **Fig. 70**. This ratio is called 'heat flux augmentation' in the following. The measured heat flux augmentation is compared to values from [11]. This study achieved similar Re_{dProbe} and particle mass concentrations c_m, but different Mach numbers. Only data of hemispherical-shaped probes of [11] are presented as black-filled symbols. The respective probe nose diameters were between 25.4 and 76.2 mm. The experimentally determined heat flux augmentation is approximately 3 and in agreement to the heat flux augmentations given in [11], although the spread of those are quite large (see **Fig. 70**). The agreement can be attributed to similar particle mass flow concentrations, similar Re_{dProbe} numbers, and the same gas species [11]. Similar heat flux augmentation 'outliers' in the experimental data were also detected in the work of [11]. In general, these outliers can be caused by inhomogeneous particle seeding and hence, cooling phases, which also affected the determination of the a_{kin} coefficient.

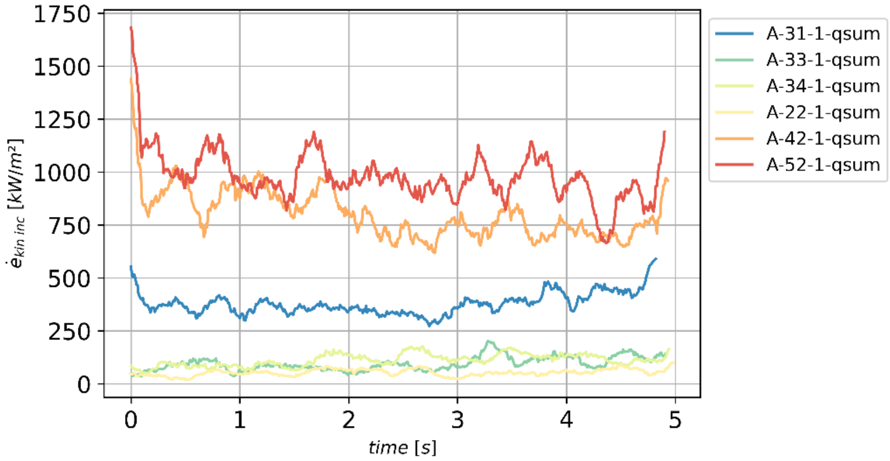

Fig. 69 Kinetic energy flux of incident particles of the 'qsum'-type tests made with Al_2O_3

Compared to other particle-induced heating augmentation studies, the heat flux augmentation is dependent on the seeded particles, the probe shape, and on the flow conditions: Considering similar particle mass concentrations, heating augmentation of just up to 1.4 [13], or even no heating augmentation was measured [12, 18]. These lower heat flux increases can be explained by lower particle inertia [13]. The lower detected heating augmentation of approximately 1.25 in the study of [12] can have multiple reasons, e.g. significantly higher stagnation temperatures, different gas species of the flow, or a flat-faced probe shape.

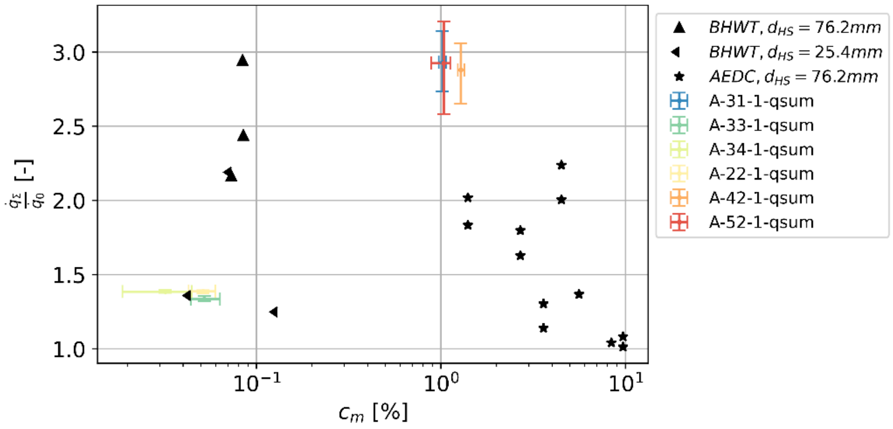

Fig. 70 Ratio of stagnation point heat fluxes in particle-laden and particle-free flows vs. the particle mass concentration c_m for all 'qsum'-type tests. Black-filled data are taken from [11] and were measured with hemispherical-shaped probes

In the following, an engineering approach for the determination of the convective heat flux increase $\Delta\dot{q}$ is derived. Generally, it is easier to estimate the kinetic energy of particles in the freestream than those of particles in the shock layer. As a consequence, the mean of the $a_{kin\ fs}$ coefficient is considered in the following. The mean of the $a_{kin\ fs}$ coefficient for Al_2O_3 particles tests is 0.28 (see **section 6.3.4**). The direct energy conversion from kinetic particle energy into thermal energy, $\dot{q}_a$, was calculated considering this mean value of the $a_{kin\ fs}$ and the kinetic energy flux of incident particles in the freestream. The convective heat flux increase $\Delta\dot{q}$ is derived from **eq. (3-1)**, the measured $\dot{q}_0$, and the calculated $\dot{q}_a$. Several heat flux ratios of all 'qsum'-type tests are summarized in **Table 28**.

The estimation of the convective heat flux increase is complex. Although there are some approaches in literature, these are valid only for different flow regimes. Furthermore, these approaches contain several simplifications to fit with the limited experimental data base. A direct comparison with the presented experiments seems to be not feasible.

The convective heat flux increase depends on multiple parameters. At least for Al_2O_3 particles in the investigated flow condition range, it can be estimated conservatively to be 1.3 times the direct energy transfer of impacting particles, which again is 28 % of the kinetic energy flux of incident particles in the freestream.

Table 28 Summary of measured heat flux ratios in particle-laden supersonic flows

synonym	**p_0**	**T_0**	**Re_{dProbe}**	**c_m**	$\frac{\dot{q}_\Sigma}{\dot{q}_0}$	$\frac{\dot{q}_a}{\dot{q}_0}$	$\frac{\Delta\dot{q}}{\dot{q}_0}$	$\frac{\Delta\dot{q}}{\dot{q}_a}$
[-]	[MPa]	[K]	[-]	[%]	[-]	[-]	[-]	[-]
A-22-1-qsum	0.950	338.1	$1.12*10^6$	0.064	1.30	0.14	0.16	0.82
A-31-1-qsum	0.594	373.1	$6.13*10^5$	0.798	2.35	0.75	0.60	0.61
A-33-1-qsum	1.286	373.2	$1.33*10^6$	0.076	1.22	0.12	0.10	0.62
A-34-1-qsum	1.685	373.4	$1.74*10^6$	0.064	1.29	0.14	0.15	0.86
A-42-1-qsum	0.952	473.4	$7.16*10^5$	0.88	2.08	0.48	0.60	0.96
A-52-1-qsum	0.952	544.0	$5.99*10^5$	1.06	2.21	0.44	0.77	1.33

6.4. Conclusion

For the first time a complete characterization of particle-laden supersonic flows including individual particle characteristics has been carried out and particle-induced heating augmentation has been determined. Particle properties were measured both in the free stream and in the shock layer simultaneously. Compared to literature, the number of assumptions describing these particle-laden flows was significantly reduced. Up to now, this is the first heating augmentation study which measured all relevant particle characteristics, namely particle size and particle velocity in the freestream and in the shock layer using non-intrusive measurement techniques.

One important aspect is the uniformity of particle seeding. Similar to previous literature, significant changes in the particle mass flow rate were observed. Although the seeding device was improved and pressure and temperature fluctuations have been reduced, the improvement of temporal homogeneous particle seeding for simplified data analysis remains an important task of future studies.

The derived a_{kin} coefficient for Al_2O_3 and MgO particle tests is significantly lower than those of the measurements and predictions from literature. The measured heat fluxes in particle-free flows are in good agreement to the Fay-Riddell approximation and the measured heat fluxes in particle-laden flows are comparable to literature values. This fact shows that the general heat flux measurements are valid and that differences in the a_{kin} coefficient come from higher measured kinetic energy fluxes of particles. This can be explained by the much higher accuracy of the implemented shadowgraphy measurement procedure, so that more and even smaller particles were registered. It was reported in **section 5.3.4.3** that shadowgraphy detected in average 58 % higher particle mass flow rates than other measurement approaches. Even if the kinetic energy fluxes of the other measurement approaches were considered, still a discrepancy between reported a_{kin} coefficients from literature and measured a_{kin} coefficients of this work exists. As a consequence, it is highly recommended that future heating augmentation studies give significantly more attention to particle flow characterization. The use of the presented shadowgraphy procedure is one possible solution.

The key findings of this section can be summarized as follows:

- The deceleration of particles in the shock layer reduced the kinetic energy flux of incident particles up to 29 %, depending on particle material and flow conditions
- the measured kinetic energy flux of rebounded particles was less than 2.5 % of the kinetic energy flux of incident particles
- The experimentally determined a_{kin} coefficient is approximately 0.36 for Al_2O_3, 0.7 for SiO_2 particles, and approximately 0.05 for MgO particles
- The measured a_{kin} coefficient for Al_2O_3 and MgO particles is significantly smaller than measurements and predictions from literature
- The measured a_{kin} coefficient for SiO_2 particles is in agreement to literature predictions, but at least two times larger than literature measurements
- The measured heating augmentation, including direct energy transfer from impacting particles and the convective heat flux increase, is in agreement to literature
- The convective heat flux increase can be estimated conservatively to be 1.3 times the direct energy transfer of impacting particles, which is 28 % of the kinetic energy flux of incident particles in the freestream for the investigated flow condition range and Al_2O_3 particles

7. Summary and Outlook

This work has shown that the accurate investigation of particle-induced heating augmentation is complex, as it is stated in numerous previous studies. It contains multiple interdependencies between particles, the probe, and the flow. If the accuracy of particle-induced heating augmentation is intended to be increased, it is necessary to concentrate on single aspects. Based on this fact, this work has focussed on the determination of particle mass flow rate which is known to be one of the most important drivers for heating augmentation in particle laden flows.

A small test facility called GBK was used to focus on measurement technique development. The flexibility of the GBK facility and its small nozzle size allowed to measure different nozzle exit particle velocities for different particle sizes easily. This approach was of high value in terms of measurement technique development, but also for drag formulation evaluation. Not only measurement techniques, but also necessary devices like the seeding generator were adapted and refined. Such numerous refinements were not economically possible in large-scale facilities. All these improvements allowed at all the analysis of heating augmentation effects. However, in future an overall re-design of the seeding device is required to achieve temporal homogenous seeding rates which again simplifies heating augmentation evaluation.

New measurement methods were established and tested to determine particle mass flow rate spatially and temporally resolved, namely shadowgraphy and PTV. Although shadowgraphy is a well-known measurement technique, much effort of this work was put on its refinement to achieve high-quality data of individual particles down to 5 µm in size with velocities up to 700 m/s. These efforts can help to achieve higher measurement accuracies of shadowgraphy to a wide range of scientific and industrial applications. Especially cold-spray applications, in which an optimal particle deposition depends on particle size and particle impact velocity, will profit from these refinements. In terms of particle-induced heating augmentation, shadowgraphy has a high potential in visualizing particle-probe-flow-interactions. Furthermore, it was possible to measure particle size and particle velocity simultaneously for the first time in heating augmentation analyses. The determined a_{kin} coefficients differ from literature values, which can be explained by the much higher accuracy of particle mass flow rate determination. Furthermore, a_{kin} coefficients from literature are rare and were determined only with the help of multiple assumptions. The implementation of shadowgraphy reduced significantly the number of required assumptions for particle mass flow rate, and hence, the a_{kin} coefficient.

Not only this work, but also previous heating augmentation studies found that particle drag formulations suffer in predicting particle velocity accurately. The achieved high-quality data of particle size and velocity is currently used by NASA AMES to develop advanced particle drag formulations.

Generally, future studies concerning heating augmentation or erosion effects will benefit from the basic developments of this work. It is planned to adapt these measurements in arc-heated facilities in the near future, which will encounter new challenges in terms of particle characterization.

8. Appendix

8.1. Overview of Experimental Particle-Induced Heating Augmentation Analysis

Table A 1 Experimental setups for supersonic two-phase flows

Parameter **year**	Unit	Fleener and Watson **1973**	Dunbar et al. **1975**	Polezhaev et al. **1992**	Vasilevski et al. **1999**	Kudin et al. **2013**
flow						
facility		arc heater, AEDC/DETF, BHWT	arc heater, AEDC/DETF, BHWT	liquid fuel combustion chamber, gas dynamic tube	TsAGI UT-1, short-duration	TsAGI GGUM, liquid fuel combustion chamber
gas	-	air	air	combustion gas	air, CO_2, N_2	combustion gas, N_2
M_∞	-	6.1 – 9.5	6.1 – 9.5	2.6 – 4.2	6	2.26, 2.39
$Re_{1\infty}$	1/m	$4.43*10^6 – 6.18*10^7$	$4.43*10^6 – 6.18*10^7$	$5*10^6 - 12.5*10^7$		
$H_{0\infty}$	kJ/kg	279 – 4187	279 – 4187	3700		
$T_{0\infty}$	K				570	290 - 1600
$p_{0\infty}$	MPa	0.02 – 0.203	0.02 – 0.203	20	0.21 – 3.3	1.5
probe						
probe shape	-	hemisphere, disk	hemisphere, disk	hemisphere, disk	hemisphere, disk	hemisphere, disk
nose radius R_N	mm	6.35, 12.7, 30.2, 38.1	12.7, 25.4, 38.1	20, 40	3, 6, 12, 24	8.1, 16.2, 25.65
probe diameter d_{Probe}	mm	12.7, 25.4, 60.4, 76.2	25.4, 50.8, 76.2	40, 80	6, 12, 24, 48	16.2, 32.4, 51. 3
probe material	-	6Al-4V titanium alloy	titanium, Inconel, stainless steel, platinum, graphite	copper	aluminum	M3 grade copper, copper
particle						
particle material	-	MgO, SiC	MgO, SiC, glass	Al_2O_3	Si_3N_4, SiO_2, Fe_2O_3, Cr_2O_3, Fe	SiO_2
nominal d_p	µm	100, 200	100, 200, 650	20, 100, 250	0.12, 0.15, 0.27, 0.75, 2.4, 161	27 - 111

Parameter	Unit	Fleener and Watson	Dunbar et al.	Polezhaev et al.	Vasilevski et al.	Kudin et al.
Year		**1973**	**1975**	**1992**	**1999**	**2013**
particle shape					approximately spherical, except CrO_3 and Fe_2O_3	irregular
material preparation					dried at 450 K, wrapped in metal foil	-
c_m	%	0.001 – 10	0.001 – 10	0.1 – 1	1 – 25	0 - 25
$v_{p\infty}$	m/s	762 - 1707	762 - 1707		1000	564, 907
$v_{p\,imp}$	m/s			1000 - 1500		
general information						
heat flux measurement	-	back face thermocouples, thin skin heat transfer model	back face thermocouple, thin skin heat transfer model	thin wall copper calorimeter with chromel – copper thermocouple	thin wall calorimeter, stainless steel foil band, grounded	calorimeter
particle characterization techniques		analytic ($v_{p\infty}$)	double pulsed holography	analytic ($v_{p\,imp}$)	Philips SEM-515 scanning electron microscope, two wavelength intensity ratio (d_p), analytic ($v_{p\infty}$)	electron microscope, particle storage receiver, kind of LDA
particle concentration measurement		analytically + dust catcher calibration	analytically + dust catcher calibration	analytically + recording membranes	analytically + scattered light registration	optical light attenuation, particle storage receiver

Parameter Year	Unit	Fleener and Watson 1973	Dunbar et al. 1975	Polezhaev et al. 1992	Vasilevski et al. 1999	Kudin et al. 2013
flow visualization techniques	-	1000Hz Schlieren system	shadowgraph	-	shadow method	shadow method, pressure sensor
investigation focus	-	rebounded particle induced turbulence	fundamental heat augmentation analysis	influence of probe size/shape, particle concentration and size, flow pressure and non-equilibrium factors	influence of small particle sizes	fundamental heat augmentation analysis
remarks	-	some data identical to Dunbar et al., additional tests with different Re Number	some data identical to Fleener and Watson		noticed electrical disturbances, data averaged from 4 – 20 ms; tests repeated 3 - 6 times	

8.2. Overview Particle Sizing with Shadowgraphy

Table A 2 Overview of studies concerning particle sizing by means of shadowgraphy

Authors	resolution/ magnification	calibration object, sizes	focus range, steps	in-focus criterion, based on	d-d_p-relation	experimental object/sizes	parameters (d_p, V_p, mass flow)	error/ uncertainty	remarks
(Koh et al. 2001)	2.9x, ~3.1 µm/px	graticule, dots 2 - 300 µm	-2.5 - 1.5 mm, 50 - 100 µm	d_p <30 µm: contrast, d_p >30 µm: gradient	linear, two slopes (<30 µm)		d_p, d_{shadow}	d_p: < 10 %, d_{shadow}: < 10 %	
(Kashdan et al. 2003, Kashdan et al. 2007)	0.7 µm/px	dots on plate, 18-145 µm, ±2 µm	±1.5 mm, 10 µm	70 % of max. halo area and gradient	linear	spray drops, 10 – 100 µm	d_p	statistical uncertainty of cumulative size distribution: 2 - 3 %	comparison: diode and Nd:YAG illumination: affects d_{shadow}, linear d_p correction
(Putkiranta et al. 2008)	5.43 µm/px	dots on plate, 3.5 – 1270 µm	0 - 1.7 mm, 50 µm	no criteria	power law, based on particle recognition	d_p = 79.2 – 1227 µm	d_p	d_p = 79.2 µm: 2.4 %, d_p = 56 µm: 5 %	no out-of-focus d_p correction
(Fdida and Blaisot 2009)	14.08 µm/px / 8.8 µm/px	calibrated discs: 40 / 150 / 300 µm	±5 mm, 0.1 - 0.5 mm	contrast, PSF	constant		d_p	d_p = 40 µm: < 2 %, general: < 5 %	d_{shadow} limited to max d_{shadow} of smallest drop diameter, min d_p = 20 µm

Authors	resolution/ magnification	calibration object, sizes	focus range, steps	in-focus criterion, based on	d-d_p-relation	experimental object/sizes	parameters (d_p, V_p, mass flow)	error/ uncertainty	remarks
(Ghaemi et al. 2010)	0.23 µm/px	-	-	‘sharp boundaries’	constant, 0.05 mm	droplets in effervescent spray, 5 – 55 µm	d, d_p, V_p	-	application of LaVision ParticleMaster, no DOF calibration
(Anand et al. 2012)	2.3 µm/px	dots on plate, 10 – 200 µm, LaVision, mono-disperse droplets 135 µm	DOF correction	area ratio at different thresholds	-	fuel droplets,10 – 200 µm	d_p	mono-droplets: <1 %, spray: < 5 %	application of LaVision ParticleMaster
(Ju et al. 2012)	1.56 µm/px	Patterson globes, circles on plate, 18 – 145 µm	< ±3 mm	70 % of DOF where interior area detectable	linear	glass spheres in water, 70 – 110 µm and 100 – 200 µm	d_p	-	comparisons and advancements of (Kashdan, Shrimpton and Whybrew 2007, Yule et al. 1978)
(Robinson et al. 2012, Robinson et al. 2013)	0.427 µm/px	PS particles dried on glass,1 – 10 µm	100 µm, 1 µm	image size and slope	-	silica particles	d, d_p	d_p mean: 3.7 – 9 %, d_p std.: 2.6 – 7 % (for d_p = 3 – 10 µm)	analysis of Fresnel & Fraunhofer diffraction patterns

Authors	resolution/ magnification	calibration object, sizes	focus range, steps	in-focus criterion, based on	d-d_p-relation	experimental object/sizes	parameters (d_p, V_p, mass flow)	error/ uncertainty	remarks
(Castanet et al. 2013)	5.5-7.5 µm/px	dots on plate, 4 – 500 µm	± 1.5mm, 100 µm	contrast and gradient	linear, two slopes, $d_p < \sim 25$ µm	deflected spray drops, 116 – 171 µm	d_p, V_p	d_p:4 µm if > 40 µm, else < 15µm	additional size correction, contrast only for small particles
(Legrand et al. 2016)	~0.43x, 15 µm/px	dots on plate, 50 – 1000 µm by LaVision	-32 – 36 mm, 1 mm	contrast and gradient	constant 10 mm for d_p 100 – 1000 µm		d, d_p	d_p:10 % up to 10x d_p from focus plane, else < 20 %, < 2 mm in positioning	amount of rejected particles/dots relevant
(Minov et al. 2016)	8.23 µm/px	monodisperse droplets, 119 – 497 µm	10 mm, 50 µm	gradient, contrast	linear, d_p dev.< 1 px	spray: 24 – 543 µm	d_p , V_p	-	
(Warncke et al. 2017)	10 µm/px	dots on plate, 10 – 2000 µm	-10 – 10 mm, 0.5 mm	normalized gradient, image size	function, in range ±9 mm	droplet breakup: 10 – 200 µm	d_p, V_p	d_p, V_p: < 4 %	ITS detection code, d_{shadow} correction

Authors	resolution/ magnification	calibration object, sizes	focus range, steps	in-focus criterion, based on	d-d_p-relation	experimental object/sizes	parameters (d_p, V_p, mass flow)	error/ uncertainty	remarks
(Hufnagel et al. 2018)	~0.88 µm/px	dots on plate, 10 – 200 µm, LaVision	DOF correction	ParticleMaster	linear	erosion in turbines Arizona Test Dust A3, 1 – 120 µm	d_p, mass flow	-	application of LaVision ParticleMaster
(Senthilkumar et al. 2020)	1.2 µm/px	bubbles and dots on plate, 20 – 400 µm	4 mm, steps 10 / 20 / 50 µm	-	linear, based on number of found dots		d_p	d_p = 63 µm, < 1 – 2 %, general < 5 %	Comparison: calib. with bubles vs. dots on plates, det. Particle number must be accounted
(Zhou et al. 2020)	2.8 µm/px	dots on plate, 30 – 240 µm	16 mm, ~ 100 µm	two diameters of two cameras per particle	linear	spray, 50 – 250 µm	d_p, d	d_p: < 3 – 5 %	depth from defocus, two cameras, min. d_p = 23 µm
(Han et al. 2022)	1.7 µm/px	-	-	gradient	constant, ±0.3 mm	lime calcination reactor: particles 15 µm – 1 mm	d_p	-	min d_p = 15 µm, particle volume concentration ~2 %, no DOF calibration

8.3. Drag Correlation

8.3.1. General

The relative particle Reynolds number Re_P is:

$$Re_p = \left(v_g - v_p\right) \frac{\rho_g}{\mu_g} d_p \tag{A-1}$$

The relative particle Mach Number Ma_p is defined as:

$$Ma_p = \frac{\left(v_g - v_p\right)}{\sqrt{\gamma\, R\, T}} \tag{A-2}$$

The Knudsen number Kn is:

$$Kn = \sqrt{\frac{\gamma \pi}{2}} \frac{Ma_p}{Re_p} \tag{A-3}$$

8.3.2. Henderson Drag Correlation

The drag correlation by Henderson, described in [78], is divided into three expressions, depending on Ma_p.

$$C_D\left(Ma_p, Re_p\right) = \begin{cases} C_{D\,sub}\left(Re_p, Ma_p\right), & if \quad Ma_p \leq 1.0 \\ C_{D\,trans}\left(Re_p, Ma_p\right), & if \quad 1.0 < Ma_p \leq 1.75 \\ C_{D,sup}\left(Re_p, Ma_p\right), & if \quad Ma_p > 1.75 \end{cases} \tag{A-4}$$

For $Ma_p < 1$, the drag coefficient is defined as:

$$\begin{aligned} & C_{D\,sub}\left(Ma_p, Re_p\right) = \\ & 24.0\left\{Re_p + S\left[4.33 + \left(\frac{3.65 - 1.53\frac{T_p}{T}}{1.0 + 0.353\frac{T_p}{T}}\right)\exp\left(-0.247\frac{Re_p}{S}\right)\right]\right\}^{-1} \\ & + \exp\left(-\frac{0.5Ma_p}{{Re_p}^{0.5}}\right)\left[\frac{4.5 + 0.38\left(0.03Re_p + 0.48{Re_p}^{0.5}\right)}{1.0 + 0.03Re_p + 0.48{Re_p}^{0.5}} + 0.1{Ma_p}^2 + 0.2{Ma_p}^8\right] \\ & + \left[(1.0 - exp\left(-\frac{Ma_p}{Re_p}\right)\right]0.6S \end{aligned} \tag{A-5}$$

With:

$$S = Ma_p\sqrt{\frac{\gamma}{2}} \tag{A-6}$$

For the subsonic regime, the authors of [78] have used experimental data with Re_p up to 1*10^4. For the regime $Ma_p > 1.75$, the maximum experimental Rep was 5*10^3. In this regime, the drag coefficient can be expressed with:

$$C_{D\,sup}(Ma_\infty, Re_{\infty\,dp}) = \frac{0.9 + \frac{0.34}{{Ma_\infty}^2} + 1.86\left(\frac{Ma_\infty}{Re_{\infty\,dp}}\right)^{0.5}\left(2 + \frac{2}{{S_\infty}^2} + \frac{1.058}{S_\infty}\left(\frac{T_p}{T}\right)^{0.5} - \frac{1}{{S_\infty}^4}\right)}{1 + 1.86\left(\frac{Ma_\infty}{Re_{\infty\,dp}}\right)^{0.5}} \tag{A-7}$$

With:

$$S_\infty = Ma_\infty\sqrt{\frac{\gamma}{2}} \tag{A-8}$$

The subscript '∞' indicates free stream conditions. So, the free stream Reynolds number $Re_{\infty dp}$ is:

$$Re_{\infty\,dp} = v_g\frac{\rho_g}{\mu_g}d_p \tag{A-9}$$

The respective free stream Mach Number Ma_∞ is defined as:

$$Ma_\infty = \frac{v_g}{\sqrt{\gamma\,R\,T}} \tag{A-10}$$

If $1 < Ma_p < 1.75$, the drag coefficient is interpolated linearly:

$$C_{D\,trans} = C_{D\,sub}\big(Ma_p = 1, Re_p\big) + \frac{4}{3}(Ma_\infty - 1)\big(C_{D\,sup}(Ma_\infty = 1.75, Re_{\infty\,dp}) - C_{D\,sub}(Ma_p = 1, Re_p)\big) \tag{A-11}$$

In this work, it is assumed that the particle temperature T_p is always in equilibrium with the surrounding gas temperature T, so:

$$\frac{T_p}{T} = 1 \tag{A-12}$$

8.3.3. Parmar Drag Correlation

The drag correlation by Parmar et al. [79] is based on the following assumptions:

1. Attention is limited to continuum flows:

$$Kn = \sqrt{\frac{\gamma\pi}{2}}\frac{Ma_p}{Re_p} < 0.01 \tag{A-13}$$

2. The particle temperature is constant and equal to the surrounding gas temperature:

$$\frac{T_p}{T} = 1 \tag{A-14}$$

3. In the limit of zero Mach number, the correlation should approach the following correlation:

$$C_{D,std}\left(Re_p\right) = \frac{24}{Re_p}\left(1 + 0.15\,{Re_p}^{0.687}\right) + 0.42\left(1 + \frac{42500}{{Re_p}^{1.16}}\right)^{-1} \tag{A-15}$$

4. Attention is limited to subcritical Reynolds numbers:

$$Re_p \lesssim 2e5 \tag{A-16}$$

5. The Mach number is limited to:

$$0 \le Ma_p \le 1.75 \tag{A-17}$$

6. The critical Mach number is defined as:

$$Ma_{p,cr} \approx 0.6 \tag{A-18}$$

The drag correlation consists of three separate correlations:

$$C_D\left(Ma_p, Re_p\right) = \begin{cases} C_{D,std}\left(Re_p\right) + \left[C_{D,Ma_{p,cr}}\left(Re_p\right) - C_{D,std}\left(Re_p\right)\right]\dfrac{Ma_p}{Ma_{p,cr}}, if\ Ma_p \le Ma_{p,cr} \\ C_{D,sub}\left(Re_p, Ma_p\right), \quad if\ Ma_{p,cr} < Ma_p \le 1.0 \\ C_{D,sup}\left(Re_p, Ma_p\right), \quad if\ 1.0 < Ma_p \le 1.75 \end{cases} \tag{A-19}$$

Drag coefficients for fixed Mach numbers are:

$$C_{D,Ma_p=1}(Re_p) = \frac{24}{Re_p}\left(1 + 0.118\, {Re_P}^{0.813}\right) + 0.69\left(1 + \frac{3550}{{Re_p}^{0.793}}\right)^{-1} \tag{A-20}$$

$$C_{D,Ma_p=1.75}(Re_p) = \frac{24}{Re_p}\left(1 + 0.107\, {Re_P}^{0.867}\right) + 0.646\left(1 + \frac{861}{{Re_p}^{0.634}}\right)^{-1} \tag{A-21}$$

$$C_{D,Ma_{p,cr}}(Re_p) = \frac{24}{Re_p}\left(1 + 0.15\, {Re_P}^{0.684}\right) + 0.513\left(1 + \frac{483}{{Re_p}^{0.669}}\right)^{-1} \tag{A-22}$$

For the supersonic regime, the drag coefficient can be expressed at follows:

$$\begin{aligned} C_{D,sup}(Re_p, Ma_p) \\ &= C_{D,Ma_p=1}(Re_p) \\ &+ \left[C_{D,Ma_p=1.75}(Re_p) - C_{D,Ma_p=1}(Re_p)\right]\, \xi_{sup}(Re_p, Ma_p) \end{aligned} \tag{A-23}$$

$$\xi_{sup}(Re_p, Ma_p) = \sum_{i=1}^{3} f_{i,sup}\,(Ma_p) \prod_{\substack{j\neq i \\ j=1}}^{3} \frac{\log Re_p - C_{j,sup}}{C_{i,sup} - C_{j,sup}} \tag{A-24}$$

$$\begin{aligned} f_{1,sup}\,(Ma_p) = &-2.963 + 4.392\, Ma_p - 1.169{Ma_p}^2 - 0.027{Ma_p}^3 \\ &- 0.233\, exp\left[\frac{1 - Ma_p}{0.011}\right] \end{aligned} \tag{A-25}$$

$$\begin{aligned} f_{2,sup}\,(Ma_p) = &-6.617 + 12.11\, Ma_p - 6.501{Ma_p}^2 + 1.182{Ma_p}^3 \\ &- 0.174\, exp\left[\frac{1 - Ma_p}{0.01}\right] \end{aligned} \tag{A-26}$$

$$\begin{aligned} f_{3,sup}\,(Ma_p) = &-5.866 + 11.57\, Ma_p - 6.665{Ma_p}^2 + 1.312{Ma_p}^3 \\ &- 0.350\, exp\left[\frac{1 - Ma_p}{0.012}\right] \end{aligned} \tag{A-27}$$

$$\begin{aligned} C_{1,sup} &= 6.48 \\ C_{2,sup} &= 8.93 \\ C_{3,sup} &= 12.21 \end{aligned} \tag{A-28}$$

In the intermediate regime the drag coefficient is defined as:

$$\begin{aligned} C_{D,sub}(Re_p, Ma_p) \\ &= C_{D,Ma_{p,cr}}(Re_p) \\ &+ \left[C_{D,Ma_p=1}(Re_p) - C_{D,Ma_{p,cr}}(Re_p)\right]\, \xi_{sub}(Re_p, Ma_p) \end{aligned} \tag{A-29}$$

$$\xi_{sup}\left(Re_p, Ma_p\right) = \sum_{i=1}^{3} f_{i,sub}\ (Ma_p) \prod_{\substack{j\neq i\\ j=1}}^{3} \frac{\log Re_p - C_{j,sub}}{C_{i,sub} - C_{j,sub}} \tag{A-30}$$

$$f_{1,sub}\ \left(Ma_p\right) = \ -1.884 + 8.422\ Ma_p - 13.70 {Ma_p}^2 + 8.162 {Ma_p}^3 \tag{A-31}$$

$$f_{2,sub}\ \left(Ma_p\right) = \ -2.228 + 10.35\ Ma_p - 16.96 {Ma_p}^2 - 9.840 {Ma_p}^3 \tag{A-32}$$

$$f_{3,sub}\ \left(Ma_p\right) = \ 4.362 \pm 16.91\ Ma_p + 19.84 {Ma_p}^2 - 6.296 {Ma_p}^3 \tag{A-33}$$

$$\begin{aligned} C_{1,sub} &= 6.48 \\ C_{2,sub} &= 9.28 \\ C_{3,sub} &= 12.21 \end{aligned} \tag{A-34}$$

8.3.4. Loth Drag Correlation

The drag correlation by Loth [80] is divided into two regimes, namely the rarefraction-dominated regime and the compression-dominated regime. In-between, the authors of [80] indicated a nexus of the drag coefficient at $Re_p = 45$.

$$C_D\ (Ma_p, Re_p) = \begin{cases} \dfrac{24}{Re_p}\left(1 + 0.15\ {Re_p}^{0.687}\right) H_M + 0.42\ C_M \left(1 + \dfrac{42500}{{Re_p}^{1.16\ C_M}} + \dfrac{G_M}{{Re_p}^{0.5}}\right)^{-1}, if\ 45\ < Re_p < Re_{p,crit} \\ \dfrac{C_{D,Kn,Re_p}}{1 + {Ma_p}^4} + \dfrac{{Ma_p}^4\ C_{D,fm,Re_p}}{1 + {Ma_p}^4}, \qquad if\ Re_p \leq 45 \end{cases} \tag{A-35}$$

The parameters for the compression-dominated regime are defined as follows:

$$C_M = \begin{cases} 1.65 + 0.65\ \tanh\left(4Ma_p - 3.4\right), & if\ Ma_p < 1.5 \\ 2.18 - 0.13\ \tanh\left(0.9Ma_p - 2.7\right), & if\ Ma_p > 1.5 \end{cases} \tag{A-36}$$

$$G_M = \begin{cases} 20 - 10.9\ Ma_p + 3.29\ {Ma_p}^2 + 166 {Ma_p}^3, & if\ Ma_p < 0.8 \\ 5 + 40 {Ma_p}^{-3}, & if\ Ma_p > 0.8 \end{cases} \tag{A-37}$$

$$H_M = \begin{cases} 1 - 0.074\ Ma_p + 0.212 {Ma_p}^2 + 0.0239 {Ma_p}^3, & if\ Ma_p < 1 \\ 0.93 + \dfrac{1}{3.5 + {Ma_p}^5}, & if\ Ma_p > 1 \end{cases} \tag{A-38}$$

The parameters for the rarefraction-dominated regime are defined as follows:

$$C_{D,Kn,Re_p} = \frac{24}{Re_p}\left(1 + 0.115\, {Re_P}^{0.687}\right) f_{Kn} \tag{A-39}$$

$$f_{Kn} = \frac{1}{1 + Kn\left[2.514 + 0.8exp\left(\frac{-0.55}{Kn}\right)\right]} \tag{A-40}$$

$$C_{D,fm} = \frac{(1 + 2S^2)\exp(-S^2)}{S^3\sqrt{\pi}} + \frac{(4S^4 + 4S^2 - 1)\mathrm{erf}(S)}{2S^4} + \frac{2}{3S}\sqrt{\pi} \tag{A-41}$$

$$C_{D,fm,Re_p} = \frac{C_{D,fm}}{1 + \left[\frac{C_{D,fm}}{J_M} - 1\right]\sqrt{\frac{Re_p}{45}}} \tag{A-42}$$

$$J_M = \begin{cases} 2.26 - \frac{0.1}{Ma_p} + \frac{0.14}{{Ma_p}^3}, & if\ Ma_p \le 1 \\ 1.6 + \frac{0.25}{Ma_p} + \frac{0.11}{{Ma_p}^2} + \frac{0.44}{{Ma_p}^3}, & if\ Ma_p > 1 \end{cases} \tag{A-43}$$

The following critical Reynolds number for the Loth drag correlation is assumed:

$$Re_{p,crit} \approx 1.5e5 \tag{A-44}$$

9. References

1. Williams, D. R. "Chronology of Mars Exploration." Vol. 2024, NASA, https://nssdc.gsfc.nasa.gov/planetary/chronology_mars.html, 2023.
2. Palmer, G., Ching, E., Ihme, M., Allofs, D., and Gülhan, A. "Modeling Heat-Shield Erosion Due to Dust Particle Impacts for Martian Entries," Vol. 57, No. 5, 2020, pp. 857-875.doi: 10.2514/1.A34744
3. Zurek, R. W. "Martian Great Dust Storms: An Update," *Icarus* Vol. 50, No. 2, 1982, pp. 288-310.doi: 10.1016/0019-1035(82)90127-0
4. Dunbar, L. E., Courtney, J. F., and Mcmillen, L. D. "Heating Augmentation in Erosive Hypersonic Environments," *AIAA Journal* Vol. 13, No. 7, 1975, pp. 908-912.doi: 10.2514/3.60468
5. Golubkina, I. V., Osiptsov, A. N., and Sakharov, V. I. "Supersonic Low-Concentration Dusty-Gas Flow Past a Plane Cylinder in the Presence of an Oblique Shock Wave Interacting with the Bow Shock," *Fluid Dynamics* Vol. 46, No. 1, 2011, pp. 51-63.doi: 10.1134/S0015462811010066
6. Hove, D., and Shih, W. "Reentry Vehicle Stagnation Region Heat Transfer in Particle Environments," *15th Aerospace Sciences Meeting*. 1977.
7. Hove, D. T., and Taylor, E. "Stagnation Region Heat Transfer in Hypersonic Particle Environments," Vol. 14, No. 10, 1976, pp. 1486-1488.doi: 10.2514/3.7240
8. Ishii, R., Hatta, N., Umeda, Y., and Yuhi, M. "Supersonic Gas-Particle Two-Phase Flow around a Sphere," *Journal of Fluid Mechanics* Vol. 221, 1990, pp. 453-483.doi: 10.1017/S0022112090003639
9. Levin, A. L. "Heat Exchange near the Critical Point of a Body within a Supersonic Two-Phase Jet," *Journal of Applied Mechanics and Technical Physics* Vol. 34, No. 5, 1993, pp. 694-700.doi: 10.1007/BF00859837
10. Polezhaev, Y. V., Repin, I. V., and Mikhatulin, D. S. "Heat Transfer in a Heterogeneous Supersonic Flow," *High Temperature* Vol. 30, No. 6, 1992, pp. 1147 - 1153.
11. Fleener, W., and Watson, R. "Convective Heating in Dust-Laden Hypersonic Flows," *8th Thermophysics Conference*. 1973.
12. Kudin, O. K., Nesterov, Y. N., Tokarev, O. D., and Flaksman, Y. S. "Experimental Investigations of a High-Temperature Dust-Laden Gas Jet Impinging on an Obstacle," *TsAGI Science Journal* Vol. 44, No. 6, 2013, pp. 869-884.doi: 10.1615/TsAGISciJ.2014011135
13. Vasilevskii, E., and Osiptsov, A. "Experimental and Numerical Study of Heat Transfer on a Blunt Body in Dusty Hypersonic Flow," *33rd Thermophysics Conference*. American Institute of Aeronautics and Astronautics, 1999.
14. Molleson, G. V., and Stasenko, A. L. "Gas-Dispersed Jet Flow around a Solid in a Wide Range of Stagnation Parameters," *High Temperature* Vol. 55, No. 1, 2017, pp. 87 - 94.doi: 10.1134/S0018151X1701014X
15. Allofs, D., Neeb, D., and Gülhan, A. "Simultaneous Determination of Particle Size, Velocity, and Mass Flow in Dust-Laden Supersonic Flows," *Experiments in Fluids* Vol. 63, 2022.doi: https://doi.org/10.1007/s00348-022-03402-z
16. Allofs, D., Neeb, D., and Gülhan, A. "Particle Mass Flow Determination in Dust-Laden Supersonic Flows by Means of Simultaneous Application of Optical Measurement Techniques," *Experiments in Fluids*, 2022.doi: 10.1007/s00348-022-03567-7
17. Allofs, D. N., Dominik; Gülhan, Ali. "Experimental Investigation of Particle-Induced Heating Augmentation in Dust-Laden Supersonic Flows," *Experiments in Fluids*, 2023.

18. Alkhimov, A. P., Nesterovich, N. I., and Papyrin, A. N. "Experimental Investigation of Supersonic Two-Phase Flow over Bodies," *Journal of Applied Mechanics and Technical Physics* Vol. 23, No. 2, 1982, pp. 219-226.doi: 10.1007/BF00911002
19. Holden, M., Duryea, G., Gustafson, G., and Hudack, L. "An Experimental Study of Particle-Induced Convective Heating Augmentation," *9th Fluid and PlasmaDynamics Conference*. 1976.
20. Wilkinson, H. R., Marcisz, T. J., Gustafson, G. Q., D'attore, L., and Bilyk, M. A. "Flow Phenomea in Particle-Induced Convective Heating Augmentation," *Report DNA 3799F*, 1976.
21. Bakum, B. I., and Komarova, G. S. "The Effect of Dust in the Working Stream of Hypersonic Wind Tunnels on the Results of Heat-Transfer Measurements," *Journal of engineering physics* Vol. 21, No. 5, 1971, pp. 1361-1363.doi: 10.1007/BF01271345
22. Bakum, B. I. "Characteristics of the Working Stream of Hypersonic Aerodynamic Tubes in the Presence of Solid Particle Impurities," *Journal of engineering physics* Vol. 19, No. 4, 1970, pp. 1290-1294.doi: 10.1007/BF00832671
23. Osipov, M. I., Gladoshchuk, K. A., and Arbekov, A. N. "Heat Transfer Processes in High-Temperature Flows of Two-Phase Media," *Heat Transfer research* Vol. 32, No. 7 & 8, 2001, pp. 402 - 708.doi: 10.1615/HeatTransRes.v32.i7-8.90
24. Nikitin, P. V., Borisov, S. A., Dobrovolskiy, S. V., and Gloukhovskaya, Y. I. "Study of the Mechanism of the Particle—Substrate Interaction in the Case of the Impact of a Supersonic Heterogeneous Flow on a Flat Solid Wall," *Journal of Surface Investigation: X-ray, Synchrotron and Neutron Techniques* Vol. 11, No. 2, 2017, pp. 375-380.doi: 10.1134/S1027451017020100
25. Kovalev, P. I. "Effect of Impact Breakup of Solid and Liquid Particles on Two-Phase Supersonic Flow About Solids," *Technical Physics* Vol. 53, No. 1, 2008, pp. 37-42.doi: 10.1134/S1063784208010076
26. Gorbushin, N. A., and Petrov, Y. V. "Dynamic Fragmentation of Solid Particles Interacting with a Rigid Barrier," *Technical Physics* Vol. 59, No. 2, 2014, pp. 194-198.doi: 10.1134/S1063784214020091
27. Stasenko, A. L. "Velocity Recovery Factors of a Particle Repelled from a Solid Surface," *Journal of Engineering Physics and Thermophysics* Vol. 80, No. 5, 2007, pp. 885-891.doi: 10.1007/s10891-007-0119-4
28. Lashkov, V. A. "Experimental Determination of the Coefficients of Restitution of Particles in the Flow of a Gas Suspension in a Collision against the Surface," *Journal of engineering physics* Vol. 60, No. 2, 1991, pp. 154-159.doi: 10.1007/BF00873057
29. Dunbar, L., Courtney, J., and Mcmillen, L. "Heating Augmentation in Particle Erosion Environments," *8th Aerodynamic Testing Conference*. 1974.
30. Edney, B. E. "Effects of Shock Impingement on the Heat Transfer around Blunt Bodies," Vol. 6, No. 1, 1968, pp. 15-21.doi: 10.2514/3.4435
31. Wassel, A. T., and Denny, V. E. "Heat Transfer to Axisymmetric Bodies in Super- and Hypersonic Turbulent Streams," *Journal of Spacecraft and Rockets* Vol. 14, No. 4, 1977, pp. 212-218.doi: 10.2514/3.27963
32. Shih, W. "Ballistics Range Measurements of Aerodynamic Heating in Erosion Environments," *9th Fluid and PlasmaDynamics Conference*. 1976.
33. Vasilevskii, E., Dombrovsky, L. A., Mikhatulin, D. S., and Polezhaev, Y. V. "Heat Transfer in a Heterogeneous Supersonic Flow," *Heat Transfer, Proceedings of the 12th International Heat Transfer Conference* Vol. 12, 2002.

34. Molleson, G. V., and Stasenko, A. L. "Kinetic-Thermal Effect of a Gas-Dispersed Supersonic Jet on an Axisymmetric Body," *High Temperature* Vol. 52, No. 6, 2014, pp. 881-889.doi: 10.1134/S0018151X14050125
35. Castanet, G., Dunand, P., Caballina, O., and Lemoine, F. "High-Speed Shadow Imagery to Characterize the Size and Velocity of the Secondary Droplets Produced by Drop Impacts onto a Heated Surface," *Experiments in Fluids* Vol. 54, No. 3, 2013, p. 1489.doi: 10.1007/s00348-013-1489-3
36. Wang, H., Felis, F., Tomas, S., Anselmet, F., and Amielh, M. "An Improved Image Processing Method for Particle Characterization by Shadowgraphy," *ILASS-Europe 2017 28th Conference on Liquid Atomization and Spray Systems*. 2017, p. 6.
37. Dehnadfar, D., Friedman, J., and Papini, M. "Laser Shadowgraphy Measurements of Abrasive Particle Spatial, Size and Velocity Distributions through Micro-Masks Used in Abrasive Jet Micro-Machining," *Journal of Materials Processing Technology* Vol. 212, No. 1, 2012, pp. 137-149.doi: https://doi.org/10.1016/j.jmatprotec.2011.08.016
38. Legrand, M., Nogueira, J., Lecuona, A., and Hernando, A. "Single Camera Volumetric Shadowgraphy System for Simultaneous Droplet Sizing and Depth Location, Including Empirical Determination of the Effective Optical Aperture," *Experimental Thermal and Fluid Science* Vol. 76, 2016, pp. 135-145.doi: https://doi.org/10.1016/j.expthermflusci.2016.03.018
39. Senthilkumar, P., Mikhil, S., and Anand, T. "Estimation of Measurement Error and Depth of Field in Pdia Experiments: A Comparative Study Using Water Droplets and a Calibration Target," *Measurement Science and Technology* Vol. 31, No. 11, 2020, p. 115204.
40. Kashdan, J. T., Shrimpton, J. S., and Whybrew, A. "Two-Phase Flow Characterization by Automated Digital Image Analysis. Part 1: Fundamental Principles and Calibration of the Technique," Vol. 20, No. 6, 2003, pp. 387-397.doi: 10.1002/ppsc.200300897
41. Anand, T., Mohan, A. M., and Ravikrishna, R. "Spray Characterization of Gasoline-Ethanol Blends from a Multi-Hole Port Fuel Injector," *Fuel* Vol. 102, 2012, pp. 613-623.
42. Ju, D., Shrimpton, J. S., and Hearn, A. "A Multi-Thresholding Algorithm for Sizing out of Focus Particles," *Particle & Particle Systems Characterization* Vol. 29, No. 2, 2012, pp. 78-92.
43. Zhou, W., Tropea, C., Chen, B., Zhang, Y., Luo, X., and Cai, X. "Spray Drop Measurements Using Depth from Defocus," *Measurement Science and Technology* Vol. 31, No. 7, 2020, p. 075901.doi: 10.1088/1361-6501/ab79c6
44. Lee, S. Y., and Kim, Y. D. "Sizing of Spray Particles Using Image Processing Technique," *KSME International Journal* Vol. 18, No. 6, 2004, pp. 879-894.doi: 10.1007/BF02990860
45. Koh, K. U., Kim, J. Y., and Lee, S. Y. "Determination of in-Focus Criteria and Depth of Field in Image Processing of Spray Particles," *Atomization and Sprays* Vol. 11, No. 4, 2001.
46. Fdida, N., and Blaisot, J.-B. "Drop Size Distribution Measured by Imaging: Determination of the Measurement Volume by the Calibration of the Point Spread Function," *Measurement Science and Technology* Vol. 21, No. 2, 2009, p. 025501.doi: 10.1088/0957-0233/21/2/025501
47. Putkiranta, M., Eloranta, H., Alahautala, T., and Saarenrinne, P. "Droplet Shadow Sizing with a Diode Laser Illumination and a Depth-of-Field Calibration," *ISFV13-13 th International Symposium on Flow Visualization, July, 1-4, 2008, Nice, France*. 2008, p. 11.
48. Kim, K. S., and Kim, S.-S. "Drop Sizing and Depth-of-Field Correction in Tv Imaging," *Atomization and Sprays* Vol. 4, No. 1, 1994.

49. Ghaemi, S., Rahimi, P., and Nobes, D. S. "Evaluation of Stereopiv Measurement of Droplet Velocity in an Effervescent Spray," *International Journal of Spray and Combustion Dynamics* Vol. 2, No. 2, 2010, pp. 103-123.
50. Han, S., Sun, Z., De Jacobi Du Vallon, C., Collins, T., Boot-Handford, M., Sceats, M. G., Tian, Z. F., and Nathan, G. J. "In-Situ Imaging of Particle Size Distribution in an Industrial-Scale Calcination Reactor Using Micro-Focusing Particle Shadowgraphy," *Powder Technology* Vol. 404, 2022, p. 117459.doi: https://doi.org/10.1016/j.powtec.2022.117459
51. Hufnagel, M., Werner-Spatz, C., Koch, C., and Staudacher, S. "High-Speed Shadowgraphy Measurements of an Erosive Particle-Laden Jet under High-Pressure Compressor Conditions," *Journal of Engineering for Gas Turbines and Power* Vol. 140, No. 1, 2018.
52. Chigier, N. "Optical Imaging of Sprays," *Progress in Energy and Combustion Science* Vol. 17, No. 3, 1991, pp. 211-262.
53. Lecuona, A., Sosa, P. A., Rodríguez, P. A., and Zequeira, R. I. "Volumetric Characterization of Dispersed Two-Phase Flows by Digital Image Analysis," *Measurement Science and Technology* Vol. 11, No. 8, 2000, pp. 1152-1161.doi: 10.1088/0957-0233/11/8/309
54. Robinson, M., Mahmud, Z., Swenson, O. F., and Hoey, J. "Development of a Particle Sizing Algorithm for Sub-10µm Particles Using Shadowgraphy," *ASME International Mechanical Engineering Congress and Exposition*. Vol. 45233, American Society of Mechanical Engineers, 2012, pp. 899-906.
55. Minov, S. V., Cointault, F., Vangeyte, J., Pieters, J. G., and Nuyttens, D. "Spray Droplet Characterization from a Single Nozzle by High Speed Image Analysis Using an in-Focus Droplet Criterion," *Sensors* Vol. 16, No. 2, 2016, p. 218.
56. Lavision Gmbh, G. "Particlemaster Shadow - Product Manual." November 8, 2019 ed., 2019, p. 110.
57. Fantini, E., Tognotti, L., and Tonazzini, A. "Drop Size Distribution in Sprays by Image Processing," *Computers & chemical engineering* Vol. 14, No. 11, 1990, pp. 1201-1211.
58. Yule, A., Chigier, N., and Cox, N. "Measurement of Particle Sizes in Sprays by the Automated Analysis of Spark Photographs," *Particle Size Analysis*, 1978, pp. 61-73.
59. Nishino, K., Kato, H., and Torii, K. "Stereo Imaging for Simultaneous Measurement of Size and Velocity of Particles in Dispersed Two-Phase Flow," *Measurement Science and Technology* Vol. 11, No. 6, 2000, p. 633.
60. Kashdan, J. T., Shrimpton, J. S., and Whybrew, A. "A Digital Image Analysis Technique for Quantitative Characterisation of High-Speed Sprays," *Optics and Lasers in Engineering* Vol. 45, No. 1, 2007, pp. 106-115.
61. Lebrun, D., Touil, C., and Özkul, C. "Methods for the Deconvolution of Defocused-Image Pairs Recorded Separately on Two Ccd Cameras: Application to Particle Sizing," *Applied optics* Vol. 35, No. 32, 1996, pp. 6375-6381.
62. Warncke, K., Gepperth, S., Sauer, B., Sadiki, A., Janicka, J., Koch, R., and Bauer, H.-J. "Experimental and Numerical Investigation of the Primary Breakup of an Airblasted Liquid Sheet," *International Journal of Multiphase Flow* Vol. 91, 2017, pp. 208-224.
63. Berg, T., Deppe, J., Michaelis, D., Voges, H., and Wissel, S. "Comparison of Particle Size and Velocity Investigations in Sprays Carried out by Means of Different Measurement Techniques," *ICLASS 06*. Kyoto, 2006.
64. Kapulla, R., Tuchtenhagen, J., Müller, A., Dullenkopf, K., and Bauer, H.-J. "Droplet Sizing Performance of Different Shadow Sizing Codes," *Lasermethoden in der Strömungsmesstechnik* Vol. 16, 2008, pp. 38-1.

65. Raffel, M., Willert, C. E., Scarano, F., Kähler, C. J., Wereley, S. T., and Kompenhans, J. *Particle Image Velocimetry*, 2018.
66. Lavision Gmbh, G. "Flowmaster Davis V10.1 - Product Manual." 2019, p. 172.
67. Gawehn, T., Gülhan, A., Al-Hasan, N. S., and Schnerr, G. H. "Experimental and Numerical Analysis of the Structure of Pseudo-Shock Systems in Laval Nozzles with Parallel Side Walls," *Shock Waves* Vol. 20, No. 4, 2010, pp. 297-306.doi: 10.1007/s00193-010-0263-1
68. Baron, P. A., and Willeke, K. *Aerosol Measurement: Principles, Techniques, and Applications. 2nd Ed*: John Wiley &amp; Sons Ltd., New York, NY (US); %J, 2001.
69. Azom. "Mgo Material Properties." Vol. 2022, Azom, https://www.azom.com/properties.aspx?ArticleID=54, 2023, p. MgO material properties.
70. Arthur, J. S. "The Specific Heats of Mgo, Tio2, and Zro2 at High Temperatures," *Journal of Applied Physics* Vol. 21, No. 8, 1950, pp. 732-733.doi: 10.1063/1.1699748
71. Scharnowski, S., Bross, M., and Kähler, C. J. "Accurate Turbulence Level Estimations Using Piv/Ptv," *Experiments in Fluids* Vol. 60, No. 1, 2018, p. 1.doi: 10.1007/s00348-018-2646-5
72. Wieneke, B. "Piv Uncertainty Quantification from Correlation Statistics," *Measurement Science and Technology* Vol. 26, No. 7, 2015, p. 074002.doi: 10.1088/0957-0233/26/7/074002
73. Kähler, C. J., Scharnowski, S., and Cierpka, C. "On the Uncertainty of Digital Piv and Ptv near Walls," *Experiments in Fluids* Vol. 52, No. 6, 2012, pp. 1641-1656.doi: 10.1007/s00348-012-1307-3
74. Bhattacharya, S., and Vlachos, P. P. "Volumetric Particle Tracking Velocimetry (Ptv) Uncertainty Quantification," *Experiments in Fluids* Vol. 61, No. 9, 2020, p. 197.doi: 10.1007/s00348-020-03021-6
75. Hovenac, E. A. "Performance and Operating Envelope of Imaging and Scattering Particle Sizing Instruments." 1987.
76. Williams, O. J. H., Nguyen, T., Schreyer, A.-M., and Smits, A. J. "Particle Response Analysis for Particle Image Velocimetry in Supersonic Flows," *Physics of Fluids* Vol. 27, No. 7, 2015, p. 076101.doi: 10.1063/1.4922865
77. Assadi, H., Schmidt, T., Richter, H., Kliemann, J. O., Binder, K., Gärtner, F., Klassen, T., and Kreye, H. "On Parameter Selection in Cold Spraying," *Journal of Thermal Spray Technology* Vol. 20, No. 6, 2011, pp. 1161-1176.doi: 10.1007/s11666-011-9662-9
78. Henderson, C. B. "Drag Coefficients of Spheres in Continuum and Rarefied Flows," Vol. 14, No. 6, 1976, pp. 707-708.doi: 10.2514/3.61409
79. Parmar, M., Haselbacher, A., and Balachandar, S. "Improved Drag Correlation for Spheres and Application to Shock-Tube Experiments," Vol. 48, No. 6, 2010, pp. 1273-1276.doi: 10.2514/1.J050161
80. Loth, E., Daspit, J. T., Jeong, M., Nagata, T., and Nonomura, T. "Supersonic and Hypersonic Drag Coefficients for a Sphere," Vol. 59, No. 8, 2021, pp. 3261-3274.doi: 10.2514/1.J060153
81. Gerhold, T., Hannemann, V., and Schwamborn, D. "On the Validation of the Dlr-Tau Code," *AG STAB Symposium*. Vol. 72, Vieweg, Berlin, 1999, pp. 426-433.
82. "Niosh Pocket Guide to Chemical Harzards - Magnesium Oxide Fume." CDC - Centers for Disease Control and Prevention, 2022.
83. Esser, B., Koch, U., and Gülhan, A. "Experimental and Theoretical Study of Mars Dust Effects - Heat Transfer Measurement Report," *MDUST*. 2006.
84. Lebigot, E. O. "Uncertainties: A Python Package for Calculations with Uncertainties." 2021.

85. Shershnev, A. A., and Kudryavtsev, A. N. "Numerical Simulation of Particle Beam Focusing in a Supersonic Nozzle with Rectangular Cross-Section," *Journal of Physics: Conference Series* Vol. 1404, No. 1, 2019, p. 012042.doi: 10.1088/1742-6596/1404/1/012042
86. Fay, J. A., and Riddell, F. R. "Theory of Stagnation Point Heat Transfer in Dissociated Air," *Journal of the Aeronautical Sciences* Vol. 25, No. 2, 1958, pp. 73-85.doi: 10.2514/8.7517
87. Cook, W. J., and Felderman, E. J. "Reduction of Data from Thin-Film Heat-Transfer Gages - a Concise Numerical Technique," *AIAA Journal* Vol. 4, No. 3, 1966, pp. 561-562.doi: 10.2514/3.3486
88. Olivier, H. "Influence of the Velocity Gradient on the Stagnation Point Heating in Hypersonic Flow," *Shock Waves* Vol. 5, No. 4, 1995, pp. 205-216.doi: 10.1007/BF01419002
89. Sutherland, W. "Lii. The Viscosity of Gases and Molecular Force," *Philosophical Magazine Series 1* Vol. 36, 1893, pp. 507-531.
90. Olivier, H. "Thin Film Gauges and Coaxial Thermocouples for Measuring Transient Temperatures." SWL - Shock Wave Labroratory RWTH Aachen University, p. 10.
91. Thiele, T., Gülhan, A., and Olivier, H. "Instrumentation and Aerothermal Postflight Analysis of the Rocket Technology Flight Experiment Rotex-T," *Journal of Spacecraft and Rockets*. 5 ed. Vol. 55, 2018, pp. 1050-1073.
92. Schultz, D. L., and Jones, T. "Heat-Transfer Measurements in Short-Duration Hypersonic Facilities." Agard, 1973.
93. Lantelme, M. T. "Energetic Characterization of Martian Atmospheric Flow in the Arc-Heated Wind Tunnel L2k Using Experimental and Numerical Methods," *Department of Mechanical Engineering, Institute of Fluid Mechanics, DLR AS-HYP*. Vol. Master, KIT - Karlsruhe Institue of Technology, 2020.
94. Wang, Q., Olivier, H., Einhoff, J., Li, J., and Zhao, W. "Influence of Test Model Material on the Accuracy of Transient Heat Transfer Measurements in Impulse Facilities," *Experimental Thermal and Fluid Science* Vol. 104, 2019, pp. 59-66.doi: https://doi.org/10.1016/j.expthermflusci.2019.02.013